

# Optical Resonator Sensors and Systems

by

Sahba Talebi Fard

B.Sc., Carleton University, 2006

M.A.Sc., The University of British Columbia, 2008

A THESIS SUBMITTED IN PARTIAL FULFILLMENT OF  
THE REQUIREMENTS FOR THE DEGREE OF  
DOCTOR OF PHILOSOPHY

in

The Faculty of Graduate and Postdoctoral Studies

(Biomedical Engineering)

THE UNIVERSITY OF BRITISH COLUMBIA

(Vancouver)

April , 2015

© Sahba Talebi Fard 2015

# Abstract

Silicon-on-insulator (SOI)-based sensors are attractive for sensing applications in environmental safety, oil and gas, medical research, and clinical applications. Since these devices are typically developed using Complementary metal-oxide-semiconductor (CMOS)-compatible multi-project-wafer (MPW) shuttles, they bring the potential for having sensing systems on chips (SSOCs), and for mass fabrication and low cost production. The objective of this thesis is to improve the sensitivity, accuracy, and repeatability of sensors fabricated on the SOI platform. Such sensors have the potential to be the key components of an SSOC.

One can increase the sensitivity of a resonator sensor by increasing the interaction between the evanescent field of the guided mode and the analyte. In this thesis, two methods for increasing this interaction in micro-ring resonator-based sensors are investigated: 1) using the transverse electric (TE) guided mode in ultra-thin strip waveguides and 2) using the quasi-transverse magnetic (TM) guided mode in thin strip waveguides. Using analyses and simulations, micro-ring sensors were designed to be fabricated within the constraints of a MPW CMOS-compatible process. Using the TE sensors, the temperature-induced errors were reduced by a factor of three; and the TM sensors exhibited twice the sensitivity of the best SOI micro-ring resonator-based sensors reported to date.

Moving towards the actual implementation of an SSOC, a system of sensors was design to correct for unwanted variations in the measurements. This system drew on multivariate techniques to achieve improvements that resulted in measurements that were more repeatable and more accurate in the

## *Abstract*

---

presence of environmental variations. The capability of this system is investigated by designing a cascade of previously developed micro-ring sensors with various waveguide thicknesses. With this system of sensors, we achieved an  $R^2$  value of predictions over 0.996 in the presence of a 2 K temperature drift. This approach significantly improved the repeatability and reliability of the measurements in the presence of undesirable variations and drifts. In another move towards achieving an SSOC, integrating photodetectors in resonator sensors was investigated. To accomplish this, ion-implantation on micro-ring sensors was used. Such integrated photodetector-sensors were designed, fabricated, and tested. Their measured sensitivities were within 90% of the expected values.

# Preface

The following publications contribute to parts of the chapters of this thesis:

- **Sahba Talebi Fard**, Samantha M. Grist, Valentina Donzella, Shon A. Schmidt, Jonas Flueckiger, Xu Wang, Wei Shi, Andrew Millspaugh, Mitchell Webb, Daniel M. Ratner, Karen C. Cheung, Lukas Chrostowski, “Label-free silicon photonic biosensors for use in clinical diagnostics”, Proc. SPIE, Silicon Photonics VIII, 8629:86290914 (**Invited**), *SPIE OPTO*, International Society for Optics and Photonics, 2/02/2013.

This was an invited conference paper. I was the lead author, prepared the manuscript and presented it at the SPIE conference. I have performed data analysis of the measurement results for the devices presented in this invited conference paper.

- **Sahba Talebi Fard**, Valentina Donzella, Shon A. Schmidt, Jonas Flueckiger, Samantha M. Grist, Pouria TalebiFard, Yichen Wu, Rick J. Bojko, Ezra Kwok, Nicolas A. F. Jaeger, Daniel M. Ratner, and Lukas Chrostowski, ”Performance of ultra-thin SOI-based resonators for sensing applications.” *Optics Express* 22, no. 12 (2014): 14166-14179.

The author identified the research problem and proposed methods to improve, performed literature review and contributed the idea. The author then calculated the parameters using simulations and analytical relations, designed the devices, and prepared the layout to be submitted for fabrication. Upon arrival of the fabricated devices, the author

performed experiments to test and characterize the devices, analyzed the measurement results and prepared the manuscript.

- **Sahba Talebi Fard**, Kyle Murray, Michael Caverley, Valentina Donzella, Jonas Flueckiger, Samantha M. Grist, Edgar Huante-Ceron, Shon A. Schmidt, Ezra Kwok, Nicolas A. F. Jaeger, Andrew P. Knights, and Lukas Chrostowski, "Silicon-on-insulator sensors using integrated resonance-enhanced defect-mediated photodetectors." *Optics Express* 22, no. 23 (2014): 28517-28529.

This paper demonstrates a ring resonator biosensor with an integrated ion-implanted detector, which exploits the resonance enhancement of the ring for increased responsivity. For this project, we brought together the expertise of two groups, one at McMaster university, and one at the University of British Columbia (UBC), where the McMaster group's expertise is in ion-implanted defect-mediated based photodetectors, and UBC's expertise is in resonator-based sensors. For this paper/project, the author performed literature search and, using simulations and analytical equations, calculated the appropriate parameters to design the devices. The author contributed to the layout of the design to be submitted for fabrication. Upon arrival of the fabricated chips, the author designed and performed experiments to test and characterize the devices, analyzed the measurement results and prepared the manuscript.

- **Sahba Talebi Fard**, et al., "*Optimized Sensitivity of Silicon-on-Insulator Strip Waveguide Resonator Sensor*", In review (2014).

The author identified the research problem and proposed methods to improve, performed literature review and contributed the idea. The author then calculated the parameters using simulations and analytical relations, designed the devices, and prepared the layout to be submitted for fabrication. Upon arrival of the fabricated devices, the author performed experiments

to test and characterize the devices, analyzed the measurement results and prepared the manuscript.

For the following publication, I have contributed the sections on thin and ultra-thin TE resonator sensors and TM racetrack resonator sensors.

- S. Schmidt, J. Flueckiger, W. Wu, S. M. Grist, **S. Talebi Fard**, V. Donzella, P. Khumwan, E. R. Thompson, Q. Wang, P. Kulik, X. Wang, A. Sherwali, J. Kirk, K. C. Cheung, L. Chrostowski, and D. Ratner, “Improving the performance of silicon photonic rings, disks, and bragg gratings for use in label-free biosensing”, Proc. SPIE, Biosensing and Nanomedicine VII 9166, 91660M (2014).

For the following publications, I have contributed to the data analysis and related methods.

- Xu Wang, Jonas Flueckiger, Shon Schmidt, Samantha Grist, **Sahba Talebi Fard**, James Kirk, Matt Doerfler, Karen C. Cheung, Daniel M. Ratner, and Lukas Chrostowski, “A silicon photonic biosensor using phase-shifted bragg gratings in slot waveguide”, *Journal of Biophotonics*, 04/2013 2013.
- Samantha M. Grist, Shon A. Schmidt, Jonas Flueckiger, Valentina Donzella, Wei Shi, **Sahba Talebi Fard**, James T. Kirk, Daniel M. Ratner, Karen C. Cheung, and Lukas Chrostowski, “Silicon photonic micro-disk resonators for label-free biosensing”, *Optics Express*, 21:79948006, 03/2013 2013.

For the following papers, I have done the pioneering work and initial investigations, performing simulation, design, and layout:

- Valentina Donzella, Ahmed Sherwali, Jonas Flueckiger, **Sahba Talebi Fard**, Samantha M Grist, and Lukas Chrostowski, “Sub-wavelength grating components for integrated optics applications on SOI chips”, *Optics Express*, 22, no. 17 (2014/8/25): 21037-21050.

- Valentina Donzella, Ahmed Sherwali, Jonas Flueckiger, Samantha M Grist, **Sahba Talebi Fard**, and Lukas Chrostowski, “Design and fabrication of SOI micro-ring resonators based on sub-wavelength grating waveguides”, *Optics Express* (2014).

# Table of Contents

<b>Abstract</b> . . . . .	ii
<b>Preface</b> . . . . .	iv
<b>Table of Contents</b> . . . . .	viii
<b>List of Tables</b> . . . . .	xii
<b>List of Figures</b> . . . . .	xiii
<b>List of Abbreviations</b> . . . . .	xvi
<b>Acknowledgements</b> . . . . .	xvii
<b>Dedication</b> . . . . .	xviii
<b>1 Introduction</b> . . . . .	1
1.1 Silicon Photonics as Sensors . . . . .	2
1.2 Objective . . . . .	6
1.3 Contributions and Some Applications . . . . .	6
1.4 Methodology and Collaborations . . . . .	9
1.5 Organization of the Thesis . . . . .	11
<b>2 Methodology and Review of the Sensors</b> . . . . .	13
2.1 Sensor's Figures of Merit . . . . .	14
2.2 Methods and Materials . . . . .	19

*Table of Contents*

---

2.2.1	Sensor Design . . . . .	19
2.2.2	Layout Design . . . . .	22
2.2.3	Fabrication . . . . .	23
2.2.4	Experimental Setup . . . . .	24
2.2.5	Microfluidic Integration . . . . .	26
2.2.6	Sensor Characterization . . . . .	28
2.3	Sensor Designs and Calibration Results . . . . .	32
2.3.1	Optical Sensor Designs . . . . .	33
2.3.2	Disk Resonators . . . . .	34
2.3.3	Strip Waveguide Bragg Grating . . . . .	36
2.3.4	Slot Waveguide Ring Resonator . . . . .	38
2.3.5	Slot Waveguide Bragg Grating . . . . .	38
2.4	Biological Results . . . . .	40
2.5	Discussion and Analysis . . . . .	42
2.6	Conclusion and Future Work . . . . .	45
<b>3</b>	<b>Ultra-Thin Resonator Sensors . . . . .</b>	<b>47</b>
3.1	Introduction and Background . . . . .	48
3.2	Design Methods and Analysis . . . . .	50
3.2.1	Bulk Sensitivities of TE Resonator Sensors . . . . .	54
3.2.2	Temperature Sensitivities of TE Resonator Sensors . . . . .	56
3.3	Experimental Methods and Materials . . . . .	56
3.4	Performance of the Ultra-Thin TE Resonator Sensors . . . . .	58
3.4.1	Sensitivity Analysis Results . . . . .	58
3.4.2	Q Factor and Intrinsic Limit of Detection (ILOD) . . . . .	62
3.5	Conclusion and Discussion . . . . .	65
<b>4</b>	<b>Optimized Sensitivity . . . . .</b>	<b>68</b>
4.1	Introduction and Background . . . . .	69
4.2	Methods and Materials . . . . .	71
4.3	Theory: Waveguide's Sensitivity . . . . .	72

*Table of Contents*

---

4.4	Resonator's Sensitivity - Effect of Dispersion . . . . .	74
4.5	Resonator's Bulk Sensitivity . . . . .	76
4.6	Resonator's Temperature Sensitivity - Simulation Results . .	80
4.7	Resonator's Surface Sensitivity - Simulations and Experiments	81
4.8	Bio-Sensing Demonstration . . . . .	82
4.9	Discussion, Summary and Conclusion . . . . .	85
<b>5</b>	<b>Integrated Photodetector Sensors . . . . .</b>	<b>88</b>
5.1	Introduction . . . . .	88
5.2	Resonator Sensors and Defect-Mediated Photodetectors . . .	89
5.2.1	Defect-Mediated Photodetectors . . . . .	90
5.2.2	Evanescent Field-Based Resonator Sensors . . . . .	91
5.2.3	Defect-Mediated Photodetector Resonator Sensor . . .	92
5.3	Design Considerations and Layout . . . . .	94
5.4	Experimental Methods and Materials . . . . .	98
5.4.1	Experimental Setup . . . . .	98
5.4.2	Reagents and Microfluidic Setup . . . . .	99
5.5	Performance Analysis and Results . . . . .	100
5.6	Analysis and Discussion . . . . .	105
5.6.1	Performance Tradeoffs . . . . .	105
5.6.2	Discussion and Analysis of Device Performance . . . .	106
5.7	Summary and Conclusion . . . . .	108
<b>6</b>	<b>Differential Sensing System . . . . .</b>	<b>111</b>
6.1	Introduction . . . . .	112
6.2	System Design and Methods . . . . .	115
6.3	Characterization and Performance of the Sensors and System	120
6.4	Discussions and Conclusions . . . . .	125
<b>7</b>	<b>Conclusions and Future Work . . . . .</b>	<b>129</b>
7.1	Summary and Conclusion . . . . .	129

*Table of Contents*

---

7.2 Future Work . . . . .	131
<b>Bibliography . . . . .</b>	<b>133</b>
 <b>Appendices</b>	
A List of Publications . . . . .	147
B Derivation of Sensitivity Formula . . . . .	150

# List of Tables

2.1	Measured refractive index (RI) of various concentrations of salt solutions, in refractive index unit (RIU) . . . . .	30
2.2	Summary of the performance and characteristics of our silicon photonics sensors . . . . .	43
3.1	Thermo optics coefficient of the materials in the system . . . .	57
5.1	Summary of the performances of designs A and B devices . . .	103
6.1	Sensitivity vectors of a few sensors . . . . .	127
6.2	Determinant of the sensitivity matrix for various combinations of a system of two resonator sensors . . . . .	127

# List of Figures

1.1	Research and development cycle . . . . .	10
2.1	Q and S demonstrations . . . . .	17
2.2	Schematic representation of the cross-section of the waveguide.	20
2.3	TE convergence test (out-of-plane) . . . . .	21
2.4	TE convergence test (in-plane) . . . . .	21
2.5	TM convergence test (out-of-plane) . . . . .	22
2.6	TM convergence test (in-plane) . . . . .	23
2.7	Schematic representation of our testing platform . . . . .	24
2.8	Picture representation of coupling light into the chip . . . . .	25
2.9	Schematic representation of our testing platform . . . . .	26
2.10	The experimental setup . . . . .	27
2.11	SEM images of the fabricated devices . . . . .	33
2.12	Mode profiles (TE and TM) for 10 $\mu\text{m}$ disk resonator . . . . .	34
2.13	Spectral shift and sensitivity for a 3 $\mu\text{m}$ radius disk resonator	35
2.14	Strip Bragg waveguide and the propagating TE mode . . . . .	37
2.15	Spectral shift and sensitivity for a strip Bragg resonator . . . . .	38

*List of Figures*

---

2.16	Slot Bragg waveguide and the propagating TE mode . . . . .	39
2.17	Spectral shift and sensitivity for a slot Bragg resonator . . . . .	40
2.18	Biosensing results for a disk and a Bragg resonator. . . . .	41
2.19	Summary of the performance of various sensors. . . . .	45
3.1	Simulation results for the cross-section of the SOI waveguides	51
3.2	Simulated evanescent field penetration depth (TE mode) . . . . .	52
3.3	Sensitivities of TE resonator sensors . . . . .	54
3.4	SEM image of ultra-thin TE resonator sensors . . . . .	57
3.5	Experimental bulk sensitivity results . . . . .	59
3.6	Experimental temperature sensitivities . . . . .	61
3.7	Prediction results of glucose concentrations while temperature varies . . . . .	62
3.8	Prediction results of glucose concentrations at constant tem- perature . . . . .	63
3.9	Performance summary of the sensors (simulation and experi- ment) . . . . .	64
4.1	Simulated evanescent field penetration depth (TM mode) . . . . .	70
4.2	Sensitivities of the waveguide as functions of slab thicknesses . . . . .	73
4.3	Surface Sensitivities of the waveguide as functions of slab thick- nesses . . . . .	74
4.4	Group indices of slab waveguides as functions of slab thick- nesses. . . . .	75

*List of Figures*

---

4.5	Calculated/simulated resonator's sensitivities. . . . .	77
4.6	Contour plot of sensitivity in nm/RIU as functions of waveguide widths and thicknesses. . . . .	78
4.7	Sensitivities of TM sensors (simulation and experiment). . . . .	79
4.8	Measured bulk sensitivities of TM sensors. . . . .	80
4.9	Temperature sensitivities of TM waveguides. . . . .	80
4.10	Calculated resonator's surface sensitivities . . . . .	82
4.11	Surface Sensing Experiment . . . . .	84
5.1	Schematic representations of proposed designs for sensing. . . . .	93
5.2	Schematic of detector cross-section . . . . .	95
5.3	Schematic presentation and microscope pictures of designs A and B devices. . . . .	96
5.4	IV curves for designs A and B. . . . .	100
5.5	Measured electrical/optical responses of photodetector sensors . . . . .	101
5.6	Experimental sensitivity results for the photodetector sensor . . . . .	104
6.1	Response of each sensor to concentration variations. . . . .	122
6.2	Response of the system of sensors to concentration variations. . . . .	123
6.3	Response of the sensors and the system to concentration variations at random temperature. . . . .	124

# List of Abbreviations

BSA	Bovine Serum Albumen
CMOS	Complementary Metal-Oxide-Semiconductor
EF	Evanescent Field
ELISA	Enzyme-Linked Immunosorbent Assay
EMI	Electromagnetic Interference
GC	Grating Coupler
IME	Institute of Microelectronics
LOC	Lab On a Chip
LOD	Limit Of Detection
MPW	Multi Project Wafer
PBS	Phosphate Buffered Saline
PDMS	polydimethylsiloxane
SEM	Scanning Electron Microscope
SOI	Silicon On Insulator
SPR	Surface Plasmon Resonance
SSOC	Sensing System On Chip
TE	Transverse Electric
TM	Transverse Magnetic

# Acknowledgements

I would like to acknowledge Profs. Lukas Chrostowski, Ezra Kwok, and Nicolas Jaeger for their support, guidance and encouragements throughout my graduate studies. I give thanks to the rest of my thesis committee members for their invaluable comments and support during my PhD program. Further, I would like to acknowledge the University of British Columbia, NSERC as well as the BC Innovation Council for their financial support.

A very special gratitude and love goes to my parents, Sirous and Nahid, who are the embodiments of determination and selflessness, for their all-embracing support, prayers, and abiding love that words cannot express. It is impossible to imagine any of my achievements without them. I further acknowledge them, and all my teachers, for planting the seeds of love of science, humbleness, and striving for excellence in my heart. They taught me to apply my knowledge to solve real world problems that effect humanity. I acknowledge my spouse for his insightful and invaluable scientific comments as well as his loving care and emotional support. I am thankful for having a supportive partner with whom I can discuss interesting scientific matters, real world problems, and service to humanity. Particular appreciation goes to my brothers who were my best friends and the point of trust and reliance, and all my close friends and families, who never stopped supporting and encouraging me. I thank my parents-in-law for their understanding and prayers, and my grand parents for their continuous thoughts of love and well wishes. At the end, I like to appreciate my sister for her beautiful smile that is always in my mind and enlightens my path. I am blessed and thankful for having people around me who shower me with their love and care.

# Dedication

To my parents, Nahid and Sirous, who have sacrificed their lives with endless love, support, and kindness

To my spouse, my eternal partner and friend, who brought me the real-life experience of the joy of love and care

To my siblings, who have always been there for me

“Arts, crafts and sciences uplift the world of being, and are conducive to its exaltation. Knowledge is as wings to man’s life, and a ladder for his ascent. Its acquisition is incumbent upon everyone. The knowledge of such sciences, however, should be acquired as can profit the peoples of the earth, . . . .”  
–Baha’u’llah

“Regard man as a mine rich in gems of inestimable value. Education can, alone, cause it to reveal its treasures, and enable mankind to benefit therefrom.”  
–Baha’u’llah

# Chapter 1

## Introduction

The healthcare efficiency and costs is an ever-increasing public issue. More easily accessible diagnosis and monitoring devices can significantly improve the outcomes. The current diagnostic gold-standard for biological analysis and protein quantification is Enzyme-Linked Immunosorbent Assay (ELISA) [1]. This method is highly sensitive [2], but requires trained operators and consumption of significant volumes of costly reagents and enzyme-labeled antibodies for optical detection, in well-equipped facilities. Therefore, the method is expensive, time consuming, and bound to sophisticated labs, which limits the accessibility and usage of this method for frequent monitoring and early detection, in home healthcare settings or rural areas. Researchers have focused on development of nano- and micro-scale sensors [2–4], with ELISA-like sensitivities and capabilities for Lab on Chip (LOC) applications, to provide affordable diagnostics to public and leverage the cost benefits of early detection [5].

Researchers have investigated and compared the performances of various sensing methods to ELISA [2]. Silicon photonics-based resonator sensors not only match and exceed the performances of ELISA [6], they have advantages

such as immunity from electromagnetic interference (EMI) and mechanical forces. Genalyte's system is a larger scale example of such technology that is currently being used for basic biomedical research [7–11]. However, this system would have been more beneficial and widely used if the sensors had higher sensitivity and larger evanescent field penetration depths to detect larger molecules or molecules further away from the surface. The other advantage of silicon photonics-based sensors (critical to their commercialization) is that their fabrication processes are compatible with CMOS circuits providing the opportunity for integration of electronics on chip as well as leveraging the fabrication economies of scale.

## **1.1 Silicon Photonics as Sensors**

Just as electronic integration has dramatically changed everyday life (e.g. with tablets, smart phones, laptops and all kinds of electronic devices), photonics integration is quickly evolving and revolutionizing several fields, from optical intra- and inter- chip connections [12], modulators and filters [13, 14], and high speed telecommunications [15], to environmental monitoring [16] and healthcare [17]. The fabrication of silicon photonics chips could exploit current CMOS foundries, resulting in a great number of potential advantages, including integration with control electronics, availability of electro-optic devices, and lowered cost facilitated by large scale production and leveraging of existing electronic facilities.

One of the most promising applications of silicon photonics is in the field of sensors and biosensor such as environmental and healthcare applications. The environmental monitoring application of these sensors include water and air quality monitoring, as well as oil and gas sensing. The biosensing applications of these sensors range from basic medical research [8] to bioterror detection [18, 19] to smart home healthcare [20] diagnostics. Sensitive, reliable, and inexpensive silicon photonic sensors integrated with microfluidics and electronics could lead to the development of integrated electro-optic microfluidic chips (Sensing System on a Chip, SSOC, or Lab on a Chip, LOC). These chips will eventually be able to perform completely automated biological and sensing analysis and present numerous advantages, such as small sample volume requirement, portability, and ease of use. Silicon photonics is poised to revolutionize biosensing applications, specifically in medical diagnostics. In principle, we can have either disposable or partially disposable sensors depending on the application and the the associated safety and costs.

The core component of a SSOC or LOC is the sensing device, which allows the detection and quantification of target molecules. Several optical sensing mechanisms have been proposed and developed so far [21, 22]; in particular Surface Plasmon Resonance (SPR) has been exploited in well-developed commercial devices [23]. Those commercial devices present some drawbacks and only a very small part of the device is actually integrated on a chip. One way to improve current sensing mechanisms is using silicon nanophotonic optical resonators that offer smaller footprints [24] while keeping high sensitivity

(comparable with commercial devices [25]). The resonant condition provides enhanced light - functionalized area interaction because the light travels multiple times and resonates within the sensing volume, and therefore interacts multiple times with the analyte, causing the sensor response to be amplified [26]. Evanescent field (EF) optical sensors exploit the interaction between the evanescent field of the waveguide mode and the material surrounding the waveguide core (e.g. analyte in the cladding medium) for detection. Among EF optical sensors, waveguide-based ring [7, 9, 27], disk [28], photonic crystal [29], and Bragg grating [30] resonators have shown excellent potential for sensing applications as well as for SSOC and LOC integration.

Our group is working on characterizing and comparing various types of resonator-based EF optical sensors. Most of the silicon photonics chips that are fabricated on a Silicon-on-Insulator (SOI) wafer are waveguide-based sensors. The high refractive index of silicon confines the light in planar nanoscaled waveguides. Due to the high index of Si ( $n_{Si}$  is about 3.46 at 1550 nm, while  $n_{SiO_2}$  is about 1.43), the light is well confined in the silicon waveguide, resulting in low propagation and bending losses for the TE polarization [31]. Nevertheless, some modal energy propagates in the surrounding media and interacts with the analyte. The overlap of electric field and analyte is dictated by the shape of the propagating optical mode and determines the sensitivity of the device. Their basic working mechanism is the detection of a change in the effective refractive index for light propagation in the structure [32], due to a variation of analyte concentration (bulk sensing) or

binding of molecules on the waveguide functionalized surfaces (surface sensing). The addition of a resonant structure allows for sensing this refractive index change by a shift in the resonance wavelength, providing a measurable response.

The geometry (ring, disk, Bragg grating, as well as waveguide type and size) and polarization of light (TM vs TE) can be optimized to design the sensing element for a given analyte and application. For example, the TM and TE have different distributions of the field in the waveguide and outside of it, so they can potentially allow for sensing particles with different sizes or distances from the sensor surface [33]. The field distribution for the TM mode has more evanescent field extending into the surrounding media (and thus in the analyte) so it can potentially provide higher sensitivity and it can allow sensing of particles farther from the waveguide surface, for example attached to long functionalization chemistries.

In our group, the performance and sensing capabilities of these devices were characterized. Comparing sensing performance across these devices will help validate architectures suitable for the application at hand. The most promising sensors for each application will then be identified for further study and development. We discuss the sensors' comparative advantages for sensing applications and provide an outlook for future work in this field.

## 1.2 Objective

The objectives of this thesis are to investigate and design novel optical sensors and systems of sensors (as the core of SSOC) on the silicon platform and to explore their capabilities for on-chip sensing systems. It is vital to have sensitive, accurate, repeatable, and reliable sensors at the core of a reliable system. The long-term objective of this work is to use these sensors and systems of sensors for development of lab-on-chip and further optimize them for various applications, such as biomedical and environmental sensing systems.

## 1.3 Contributions and Some Applications

In this thesis,

- Methods to improve the sensitivity of the sensors as single devices is proposed and demonstrated.
- Optimum waveguide dimension to achieve the highest sensitivity is demonstrated analytically and experimentally.
- One new method to integrate a detector with a sensor is investigated.
- Novel design of a system of sensors, mimicking multivariate techniques, to correct for unwanted variations and to accomplish a more repeatable and accurate measurement in the presence of environmental variations, is demonstrated and achieved.

### 1.3. Contributions and Some Applications

---

There are numerous applications for this work in the sensing field. Some possible applications of this work include, but not limited to: medical and clinical diagnostic and/or monitoring, research and development, and environmental safety.

These sensors can be used in medical and clinical application for patients that require real-time monitoring, such as glucose monitoring for diabetes patients, as well as patients that require less frequent monitoring, such as TSH for patients with thyroid deceases or CTNI for people with Cardiovascular Diseases (CVD) who are prone to Myocardial Infarction (MI) or heart attack. Their small size, immunity from electromagnetic interference, sensitivity to adsorbed bimolecular layers at their surface, and compatibility with established, high volume CMOS foundry processes make them an attractive technology for lab-on-chip applications [17, 21, 34-36]. This makes them useful for smart home healthcare [20] diagnostics.

These sensors are also promising for basic medical research and diagnosis [8] since they are sensitive to adsorbed bimolecular layers at their surface. Genalyte's diagnostic platform leverages a TE mode silicon photonic ring resonator and has demonstrated significant progress towards realizing the first commercially available, highly multiplexed, silicon photonic biosensor for clinical and research use [7-11]. There still exist many medical diagnostic applications where TE mode ring resonators cannot achieve the sensitivity required for a definitive clinical diagnosis without secondary amplification [7, 37]. Therefore, developing sensors with higher sensitivities and larger pen-

### 1.3. Contributions and Some Applications

---

etration depths is highly desirable. A TM-mode based sensor, for example, provides larger penetration depths, allowing for sensing molecules attaching to long functionalized chemistries further from the surface of the sensor. An example is glycoprotein receptor molecules that play an important role in initiating cellular binding and communication. These membrane-bound proteins, which can be immobilized on a silicon photonic biosensor, often bind small ligands (10-15 nm in size) or in the case of bacteria, the adhesins at the end of their long fimbria. Since fimbria are often 100's nm long, a sensor capable of detecting bound mass several 100's nm from the sensor's surface is needed, especially for bacterial adhesion and other cellular diagnostic applications. Therefore, silicon photonic biosensors with Quasi-TM guided mode, which naturally extend their sensing field 100's of nm from the sensor's surface, are ideally suited for these kinds of biosensing applications.

Furthermore, these sensors can be used for water and air quality monitoring applications, as well as oil and gas sensing. Examples include detection of the presence of Organophosphorus (OP) in water, that is extremely harmful to human, or detection of various toxic molecules in the air. Organophosphorus (OP) pesticides have been used as insecticide on broad range of crops (vegetables, fruits, etc). Although designed to kill pests, but OP pesticides can be extremely harmful to humans due to their significant contribution to cancer mortality [38], and their potential in effecting humans' nervous system at low concentrations (they inhibit the nervous system enzyme, AChE [39]).

## 1.4 Methodology and Collaborations

To achieve the objectives, it was required to go through the research and development cycle multiple times. Each research and development cycle consists of:

1. Define research problem through observations, experience and literature reviews.
2. Propose methods and designs to address the problem.
3. Simulation and analysis of the design to predict its feasibility and performance, and to calculate and optimize the parameters.
4. Design of the mask layout based on the process design kit (PDK) provided by the foundry services.
5. Design is sent for fabrication
6. Measurement and tests
7. Analysis of the results and characterization of the devices
8. Optimizing and improving the design based on the results and repeating the cycle
9. Publication of the results.

Fabrication of the devices are achieved through Multi Project Wafer (MPW) runs offered by commercial CMOS-photonics fabrication facilities,

## 1.4. Methodology and Collaborations

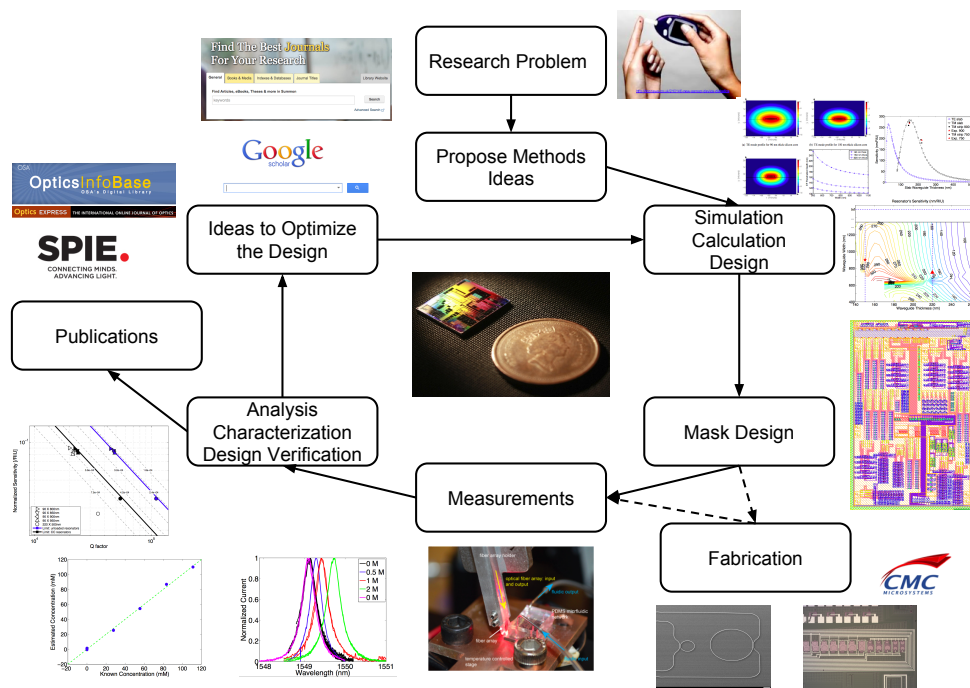


Figure 1.1: Schematic representation of our research and development cycle.

such as The Institute of Microelectronics (IME) foundry in Singapore, and IMEC [40]. For initial investigations, we usually used E-Beam Lithography (EBL) System at the University of Washington - Washington Nanofabrication Facility (UW WNF) that has a quick turnaround time.

Design and performance of biomolecular binding experiments are done in collaborations with Dr. Ratner's group at the University of Washington (UW) in Seattle. Specifically, the sandwich assays explained in section 2.2.6 are designed at UW, and the experiments incorporating these assays are performed on their site.

The design and fabrication of the microfluidic channels in poly dimethylsiloxane (PDMS) was performed by our collaborator's group at UBC (Dr. Karen Cheung).

The work on the integrated photodetector sensor (chapter 5) was in collaboration with McMaster university. The layouts of the designs were discussed with Prof. Andrew Knights, and the ion-implantations of the devices were performed at McMaster university.

## 1.5 Organization of the Thesis

To achieve the objectives, this PhD thesis is organized into following chapters.

Chapter 2 includes an overview of some of the sensors developed in our group. This chapter also includes the figures of merit for evaluating the performance of the sensors, as well as detailed materials and methods used throughout this thesis. Sensors with higher sensitivities to the refractive index changes of the analyte, or molecular adsorption, are more desirable for most sensing applications. Therefore, in the rest of this thesis, we propose and investigate methods to improve and optimize the sensitivity of the sensor (chapters 3 and 4). One novel method of integrating a detector with a sensor device is investigated (chapter 5). This work was done in collaboration with McMaster University. In addition, a system design of multiple sensors capable of correcting for some *'unwanted'* common changes and drifts is proposed and investigated (chapter 6). At the end, chapter 7 concludes the thesis with

### 1.5. *Organization of the Thesis*

---

a brief summary as well as discussions and suggestions for future research directions.

# Chapter 2

## Methodology and Review of the Sensors <sup>1</sup>

Our group has worked on developing various SOI-based resonator sensors such as TE and TM disk [28], slot ring, Bragg grating [30], and sub-wavelength gratings (SWG). These devices have been investigated for wavelengths around  $\lambda=1550$  nm (conventional wavelength window in fiber-optic communication) and  $\lambda=1220$  nm, where the water absorption is greatly decreased, offering improved limits of detection. Each one of these have advantages as well as drawbacks, for example, devices such as slot waveguide Bragg grating sensors have shown high sensitivities and high quality factors and may present advantages for specific biosensing applications, however they are usually long resulting in larger footprints; also cascading these devices is challenging.

To compare the performance of these sensors, we use a set of criteria that will be explained in section 2.1.

To characterize the device and measure the performance, we used an

---

<sup>1</sup>Parts of of this chapter have been published in [34]:  
S. Talebi Fard, et al., “Label-free silicon photonic biosensors for use in clinical diagnostics”, Proc. SPIE, Silicon Photonics VIII, 8629:86290914 (Invited), SPIE OPTO, International Society for Optics and Photonics, 2/02/2013.

automated test setup, which is explained in section 2.2.

In section 2.3, we compare the performance of different optical resonator devices, i.e. rings, disks and slot-waveguide Bragg gratings, that have been designed and fabricated, using electron beam (e-beam) lithography rapid prototyping as well as standard CMOS foundry fabrication processes on SOI chips.

## 2.1 Sensor's Figures of Merit

To compare the performance of the devices, the set of criteria is included in this section [17, 34, 35, 41, 42].

In evanescent field (EF) sensors, changes in refractive index of the cladding (resulting from molecular binding events or concentration variation) change the effective index of the propagating mode. The ratio of the change in effective index of the propagating mode to the changes in refractive index of the cladding medium, is defined as the mode sensitivity,  $S_{mode}$ , or waveguide's bulk sensitivity:

$$\begin{aligned} S_{mode_{bulk}} &= \frac{\delta n_{\text{eff}}(n_{cl}, n_{co}, n_{box}, \omega)}{\delta n_{cl}} \\ &= \frac{n_{\text{eff}}(n_{cl} + \delta n_{cl}, n_{co}, n_{box}, \omega) - n_{\text{eff}}(n_{cl}, n_{co}, n_{box}, \omega)}{\delta n_{cl}} \end{aligned} \quad (2.1)$$

where  $n_{\text{eff}}$  is the effective index of the waveguide,  $n_{cl}$  is the refractive index of the cladding medium (including the biomolecules of interest),  $n_{co}$  is the refractive index of the waveguide core material,  $n_{box}$  is the refractive index

## 2.1. Sensor's Figures of Merit

---

of the buried oxide (BOX) material, and  $\omega = 2\pi f$  is the optical frequency. This change in the effective index, in turn, results in a change in the resonant wavelength(s) of the resonator, which can be measured.

Waveguide's (or modal) surface sensitivity is defined as the change in effective index of the waveguide as biomolecules adsorb to the surface of the waveguide's core:

$$S_{mode_{surf}} = \frac{\delta n_{eff}}{\delta t} \quad (2.2)$$

where  $t$  is the thickness of the bimolecular layer adsorbed to the surface.

The sensor's refractive index sensitivity is defined as the shift in resonant wavelength as a function of the change in refractive index of the cladding [17, 34, 43]:

$$S = \frac{\Delta \lambda_{res}}{\Delta n_{cl}} = \frac{\lambda_{res}}{n_g} \frac{\delta n_{eff}}{\delta n_{cl}} \quad (2.3)$$

where  $\lambda_{res}$  is a resonant wavelength, and  $n_g$  is the group index. The wavelength shift is the result of contributions from various factors:

1. The change in the refractive index of the cladding medium ( $\Delta n_{cl}$ ).
2. The effect of material and waveguide dispersions ( $n_g$ ): due to the wavelength dependence of the effective index, a change in wavelength results in a further change in the effective index.  $n_g$  takes this effect into account.
3. As the index changes, the mode profiles slightly change, and therefore the mode's effective index and sensitivity ( $\frac{\delta n_{eff}}{\delta n_{cl}}$ ) changes.

## 2.1. Sensor's Figures of Merit

---

When comparing different wavelength resonators, normalized sensitivity ( $S'$ ) is used:

$$S' = \frac{S}{\lambda_{res}} = \frac{1}{\lambda_{res}} \frac{\Delta\lambda_{res}}{\Delta n_{cl}} \quad (2.4)$$

Surface sensitivity of a resonator is defined as:

$$S_{surf} = \frac{\Delta\lambda_{res}}{\Delta t} = \frac{\lambda_{res}}{n_g} \frac{\delta n_{eff}}{\delta t} \quad (2.5)$$

Another important property of optical waveguide resonator-based sensors is their quality factor,  $Q$ , defined as the number of optical oscillations until the resonating energy decays to  $1/e$  of its maximum value. The higher the number of these oscillations, the more light interacts with analyte. High quality factor means improved minimum detectable wavelength shift (leading to improved limit of detection, equation 2.9). The intrinsic quality factor ( $Q_i$ ) of a resonator is defined and approximated as [17, 34]:

$$Q_i = \omega_r \frac{E}{dE/dt} = \omega_r \tau_p = \frac{\omega_r}{\alpha_{[m-1]} \times \frac{c}{n_g}} = \frac{2\pi \times n_g}{\lambda_{res} \times \alpha_{[m-1]}} = \frac{2\pi \times n_g \times 4.34}{\lambda_{res} \times \alpha_{[dB/m]}} \quad (2.6)$$

where  $\alpha$  is the loss in the resonator and  $\omega_r = 2\pi f_r$  is the resonant frequency.

For a critically coupled resonator:

$$Q = \frac{Q_i}{2} \quad (2.7)$$

## 2.1. Sensor's Figures of Merit

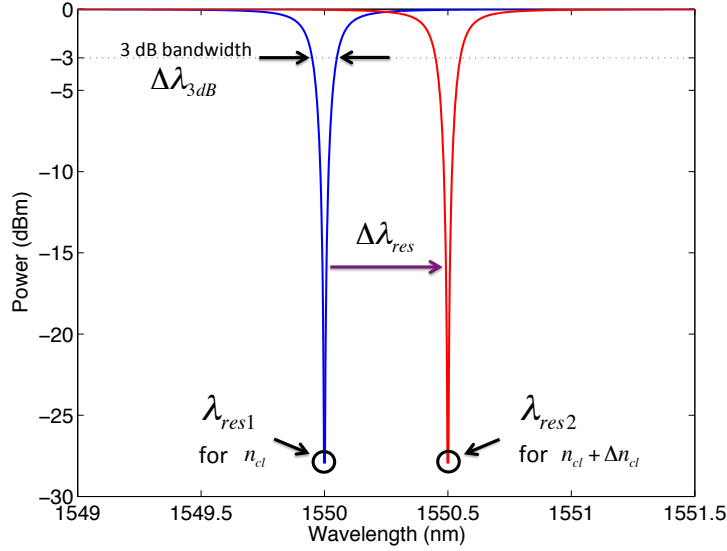


Figure 2.1: Schematic demonstration of  $Q$  value and sensitivity ( $S$ ) of a resonator sensor. The red spectrum is the shifted version of the blue spectrum corresponding to a change in the refractive index of the cladding ( $\delta n_{cl}$ ).

Experimentally, we can measure  $Q$ :

$$Q \approx \frac{\lambda_{res}}{\Delta\lambda_{3dB}} \quad (2.8)$$

where  $\Delta\lambda_{3dB}$  is the 3dB bandwidth of the resonance. A higher  $Q$  indicates a sharper resonance. Figure 2.1 schematically demonstrates how  $Q$  and  $S$  are calculated from the given spectra.

Since shifts in the resonant wavelength of sharper peaks are easier to detect, both the resonator's  $Q$  and sensitivity impact its sensing ability. The absolute limit of detection (minimum detectable refractive index change in cladding) of a resonator-based optical biosensor is affected by both the in-

## 2.1. Sensor's Figures of Merit

---

intrinsic characteristics of the resonator and the characteristics of the measurement system (thermal stability, optical input laser noise, etc), both of which should be optimized. To compare different resonators, independent of their operating wavelength and system optimizations, we have used the previously defined intrinsic limit of detection (ILOD) [17, 34, 42]. This takes into account bulk sensing characteristics of the resonators.

The minimum refractive index unit change that can be detected by the resonator, not taking into account the other system components (eg. laser, readout hardware), is called Intrinsic Limit of Detection (ILOD) as defined by the equation 2.9.

$$\Delta n_{min} = \text{ILOD} = \frac{\lambda_{res}}{QS} = \frac{1}{QS'} \quad (2.9)$$

However, researchers have demonstrated that the system's LOD can be typically 100 times better than iLOD [42]. We have utilized commonly used methods such as  $R^2$  and standard deviation to compare systems' performances. From the system's point of view, there are challenges, as described in chapter 6, and there are various sources of error that can impact the system's performance and contribute to the noise. These sources of error include, but not limited to, laser noise (amplitude relative intensity noise, phase noise, wavelength accuracy and repeatability, laser wavelength drift), detector thermal noise, shot noise, thermal fluctuations and thermal gradients on the chip, etc. Chapter 6 identifies thermal variations as being the

dominant contributor to error and can be reduced significantly using our system's design.

## 2.2 Methods and Materials

This section will include details of the design and fabrication of the sensors, the experimental setup, and the reagents used for sensor characterization and bio-experiments.

If there are slight variations to these for any specific chapter, it will be included in a the *methods* section of that chapter.

### 2.2.1 Sensor Design

To design the parameters of the various sensor types, simulations were conducted using Lumerical's MODE (fully-vectorial 2D eigenmode calculations), as well as analytical modelling in MATLAB.

Lumerical MODE solutions was used to calculate the effective index of the waveguide. Figure 2.2 shows the cross-section of the waveguide schematically.

#### Simulation Area

To determine the sensitivity, we calculated the change in  $n_{eff}$  of the waveguide as the refractive index of the cladding changes. To observe these changes and also to have reasonably accurate estimation of  $n_{eff}$ , we aim for errors in the orders of or less than  $10^{-5}$ . This value also ensures that the mode

## 2.2. Methods and Materials

---

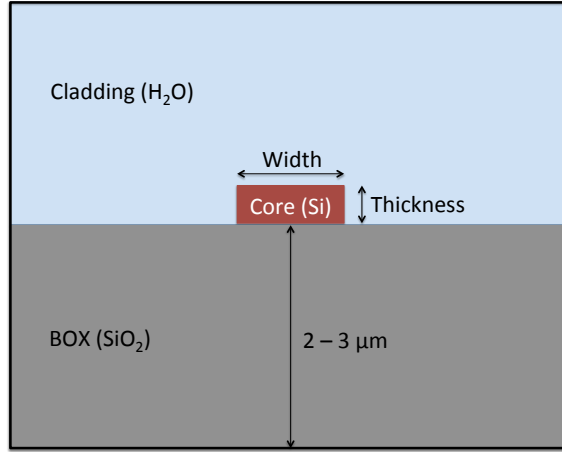


Figure 2.2: Schematic representation of the cross-section of the waveguide.

perturbation due to boundary values is minimal.

To determine the approximate dimensions for simulation area, the error in  $n_{eff}$  is estimated as a function of the dimensions of the simulation area, based on the method explained in [44]. We first determine the simulation span for the out-of-plane direction by calculating the  $n_{eff}$  of the slab waveguide as the simulation span increases (figure 2.3). We then use the  $n_{eff}$  of the slab to calculate the  $n_{eff}$  in the in-plane direction, and to determine the error in  $n_{eff}$  as the simulation span in the in-plane direction increases (figure 2.4).

We have performed these convergence tests for various waveguide thicknesses under study. As the waveguides get thinner, the mode is less confined (this is the cause of higher sensitivity). Therefore, larger simulation spans are required to get the desired error.

Our investigation of TM mode is for waveguide core thicknesses of 220, and 150 nm. To estimate the required simulation area for TM calculations,

## 2.2. Methods and Materials

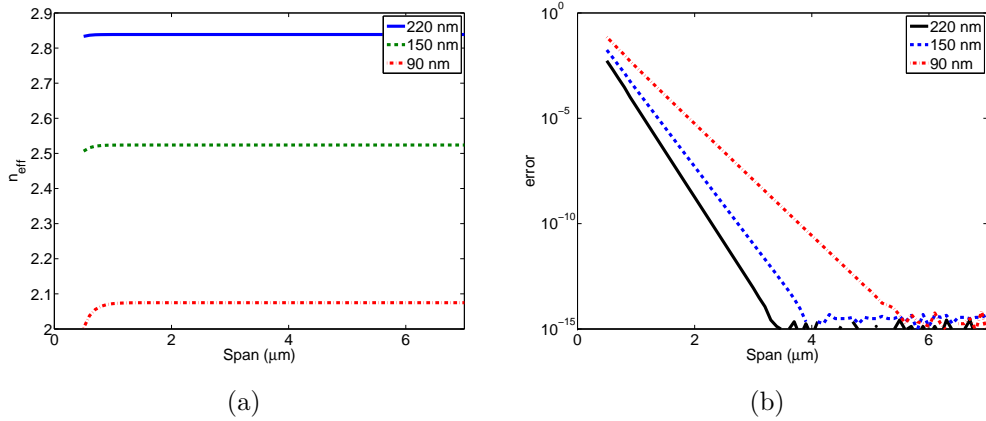


Figure 2.3: Estimated error in simulating effective index for the first TE mode as simulation span increases, out-of-plane, for various waveguide thicknesses.

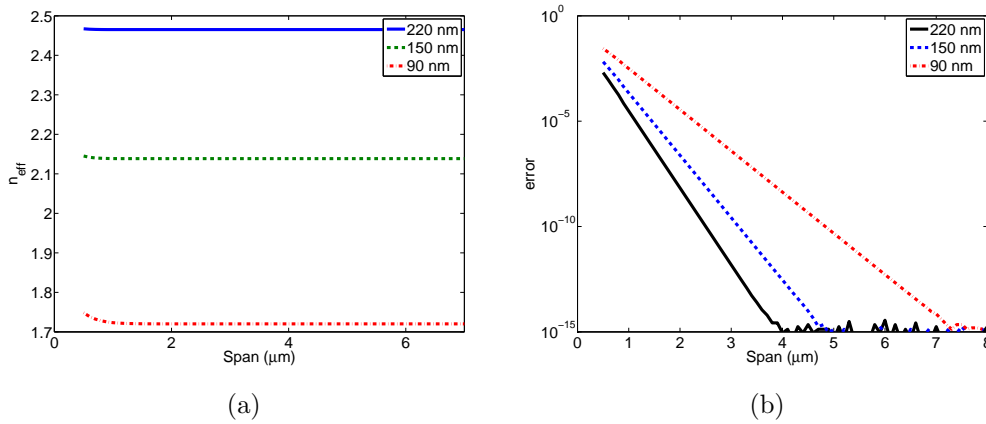


Figure 2.4: Estimated error in simulating effective index for the first TE mode as simulation span increases, in-plane, for various waveguide thicknesses.

## 2.2. Methods and Materials

the area on the top and bottom (out-of-plane simulation span) is calculated, then the  $n_{eff}$  of the slab is used to calculate the required area on two sides (in-plane simulation span). Figure 2.5 and 2.6 shows plots of the calculated error as the simulation area in these two directions increase.

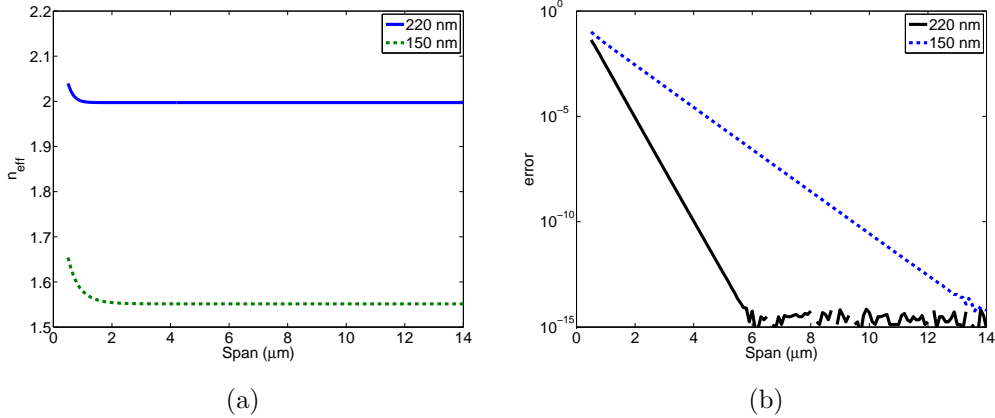


Figure 2.5: Estimated error in simulating effective index for the first TM mode as simulation span increases, out-of-plane, for various waveguide thicknesses.

### 2.2.2 Layout Design

Light is coupled into and out of the chip using grating couplers (GCs) [45]. The sensors designed for biological applications were all aligned towards the center of a large chip (e.g.  $16 \times 25$  mm) containing multiple designs, to allow for poly dimethylsiloxane (PDMS) bonding on chip. This design facilitates the exposure of the sensors to various reagents, when the microfluidic channels in PDMS are aligned to the sensors. On the chip, PDMS channels are reversibly bonded, in order to allow the flow of liquids and biological fluids

## 2.2. Methods and Materials

---

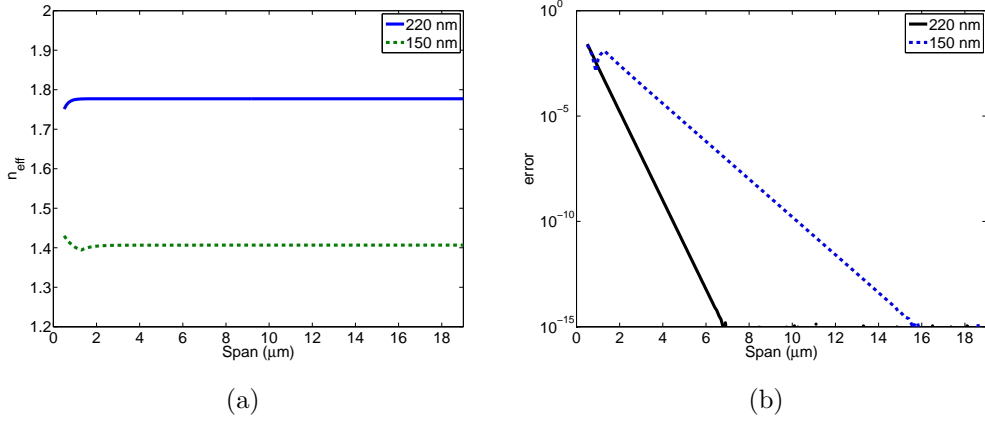


Figure 2.6: Estimated error in simulating effective index for the first TM mode as simulation span increases, in-plane, for various waveguide thicknesses.

on the top of the devices. Sometimes, sensors are fabricated with reference sensors, which are not subjected to change in analyte concentration or solution (they can be under PDMS, or in a different channel), thus they can allow correction for temperature drift or other effects.

### 2.2.3 Fabrication

Optical devices were fabricated on SOI chips using various foundry services. For initial investigations, we usually used an E-Beam Lithography (EBL) System at the University of Washington - Washington Nanofabrication Facility (UW WNF) that has a quick turnaround time. In addition, various foundries with multi-project wafer (MPW) services such as IMEC [40] and IME in Singapore were used.

### 2.2.4 Experimental Setup

Our automated measurement setup is currently capable of automatically measuring hundreds of devices within only a few hours. Figure 2.7 shows the schematics of our setup.

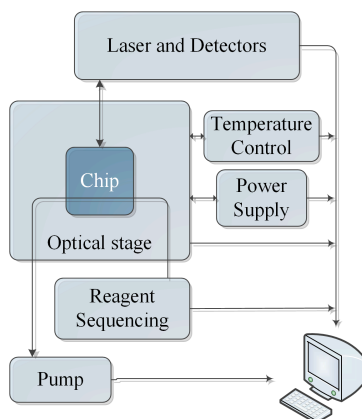


Figure 2.7: Schematic representation of our testing platform [courtesy of UW team]

The setup consists of a tunable laser (Agilent 81682A, Agilent Technologies, Inc., USA) as the optical source that operates with an output range of 1460 nm to 1580 nm. An array of polarization maintaining (PM) optical fibers (PLC Connections, LLC., USA) is used to couple light from the tunable laser to the silicon waveguides on the chip through a GC (figure 2.8). The guided mode in the waveguide will then travel through the biosensor and after interacting with the reagents will go to an output GC, which couples the light from the waveguide into another PM optical fiber.

A vacuum is used to immobilize the photonic chip onto the motorized stage (Thorlabs, USA). The efficiency of light coupling from the fiber array

## 2.2. Methods and Materials

---

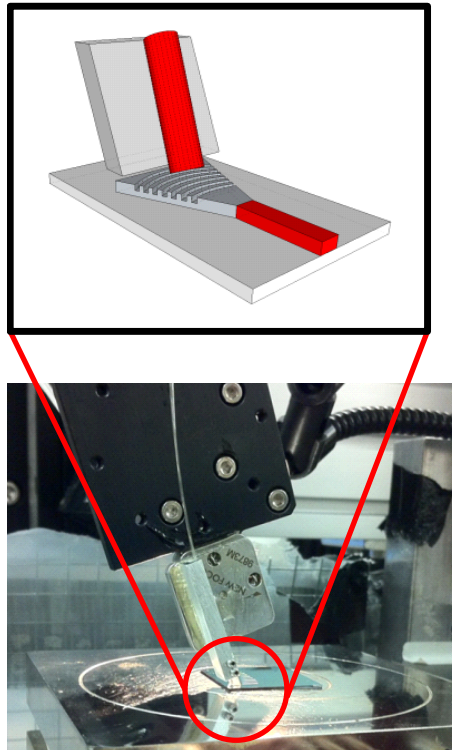


Figure 2.8: Schematic representation and a picture of how light gets coupled into the chip. [courtesy of UW team]

to the Si waveguides and back out from the chip is very sensitive to the alignment (rotational and linear alignment) of the fiber array itself to the fiber grating couplers. By monitoring the output power and moving the stage in plane, the alignment is automatically optimized with a MATLAB script by maximizing collected output power.

The stage temperature is controlled with a Peltier element and a feedback controller (LDC501, Stanford Research System, USA) with a typical stability of 1-10mK.

The intensity of the output light is then measured with an optical power

## 2.2. Methods and Materials

---

sensor (Agilent 81635A, Agilent Technologies, Inc., USA). All of the above mentioned processes are controlled with MATLAB programs that control the tunable laser and optical detectors as well as a motorized stage holding the chip. A MATLAB script is also used to sweep the laser wavelength and to acquire the transmission spectrum. The motorized stage is controlled through a script to align the fiber array to the GCs on the chip; and move from one GC to another to interrogate various biosensors.

Figure 2.10 and 2.9 are two picture representation of the test setup. One using PDMS as microfluidic channel, and the other using the silicone gasket with Polytetrafluoroethylene (PTFE) flow cell.

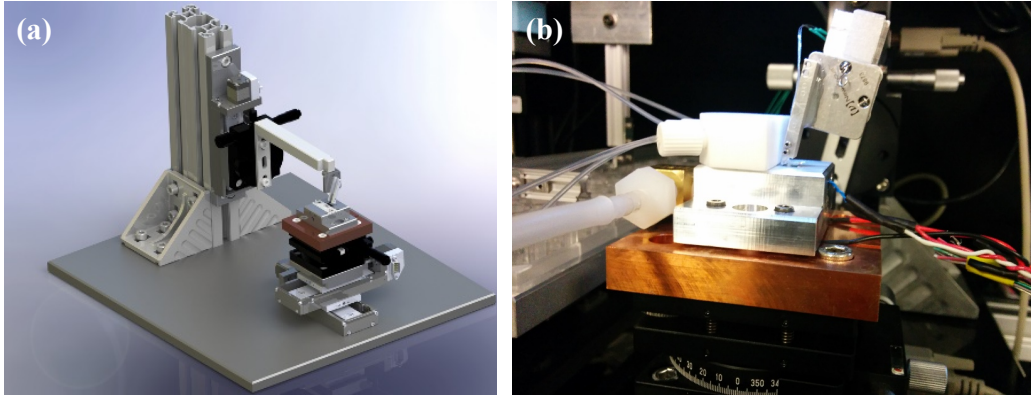


Figure 2.9: Schematic representation of our testing platform [courtesy of UW team]

### 2.2.5 Microfluidic Integration

Custom design and fabrication of the microfluidic channels in poly dimethylsiloxane (PDMS, Sylgard 184, Dow Corning, USA), using soft-lithography procedures, provided the means to expose specific set of devices on SOI chip

## 2.2. Methods and Materials

---

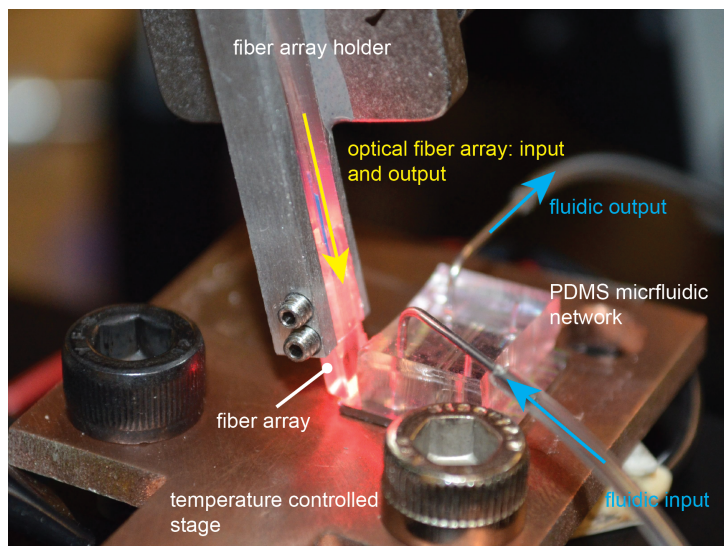


Figure 2.10: The experimental setup: fiber array is used to both bring the light from a tunable laser source (operating in 1460 nm to 1580 nm wavelength range) to, and collect the output light from the chip to be transferred to the optical power sensor. The chip is immobilized on the motorized stage using vacuum. [34]

to the fluidic reagents. The mold masters were fabricated with standard photolithography in SU-8 2075 (MicroChem, USA). Uncured PDMS was then poured onto the molds to a thickness of about 1 cm. Before curing for 2 hours at 80°C, the PDMS was degassed in a desiccator for 10min to remove unwanted air bubbles.

These fabricated polydimethylsiloxane (PDMS) microfluidic channels were used to deliver the refractive index titrations to the sensors (figure 2.10). Inlet and outlet holes are punched into the PDMS layer to access the microchannels and to connect to the syringe pump. The inlet and outlet holes were punched with a 0.5 mm coring tool (Schmidt Press, CORP, USA) prior to bonding and connected to tygon micro-bore tubing using 22 gauge blunt

needles (Nordson EFD, CORP., USA) to serve as the fluidic inlet and outlet of the device. The PDMS fluidic block was then aligned to the devices under study on the SOI substrate using a stereo microscope. The reversible bond formed between the SOI substrate and the PDMS block is strong enough to form a seal to withstand the pressure used to drive the flow during our experiment; however, to minimize the risk of leakage, the fluids were supplied to the channels under a negative pressure (the syringe pump was set to withdraw rather than inject). A syringe pump (KDS-230, KD Scientific, Inc., USA) operating in withdraw mode (negative pressure) was used to control the flow rate in the device, usually at a constant flow rate of about 10  $\mu\text{L}/\text{min}$ . Maintaining a slow flow is required in these experiments both to avoid creating air bubbles as well as to allow the system to maintain thermal equilibrium.

In some recent experiments at the university of Washington, a different method is used to deliver various solutions to the sensor. To deliver reagents to the sensor, a 500 nm thick laser-cut silicone gasket (Grace BioLabs, Bend, Oregon) defined 300  $\mu\text{m}$  wide channels over the optical sensors and mated with a custom, PTFE (Teflon®) flow cell to connect the Tygon tubing (figure 2.9).

### 2.2.6 Sensor Characterization

To characterize the sensor devices and demonstrate their bulk sensitivity capabilities, aqueous solutions of salt and aqueous solutions of glucose were

used, interchangeably. A standard sandwich assay was used to demonstrate the surface sensitivity capabilities of the sensors.

Currently, to characterize and demonstrate the performances of our devices, we have to perform multiple steps and multiple scans at each step. This can take a few hours for characterization of each device and even longer (sometimes days) when surface modifications with bio-reagents are required. However, when these devices are developed and ready to be used for sensing applications, ideally only one scan is needed to determine/predict the value of interest, which takes less than a minute.

### **Refractive Index Calibration Using Salt Solutions**

To characterize the performance and bulk sensitivity of the devices, a set of aqueous solutions of NaCl were used with various concentrations (7 samples in the range of 0 to 2M). To ensure the accuracy of the characterization, refractive index (RI) of these solutions was measured and characterized using a Reichert AR200 digital refractometer (Depew, NY), in refractive index unit (RIU).

The measured solutions are included in table 2.1.

The sensor was subjected to the various solutions and its response measured to determine the resonant shift while the optical stage was thermally tuned to 25 degrees Celsius to limit the impact of thermal drift on the measurements.

## 2.2. Methods and Materials

---

Table 2.1: Measured refractive index (RI) of various concentrations of salt solutions, in refractive index unit (RIU)

Reagent	Measured RI (RIU)
Ultrapure, deionized water	1.3334
62.5 mM NaCl	1.3335
125 mM NaCl	1.3344
250 mM NaCl	1.3354
500 mM NaCl	1.3375
1 M NaCl	1.3430

### Refractive Index Calibration Using Glucose Solutions

Aqueous solutions of glucose can also be used to determine the bulk sensitivity characteristics of the sensors. Therefore, aqueous solutions of D-Glucose (D16-500, Fisher Chemicals, Fisher Scientific, Inc.) in distilled water with various concentrations were prepared using the multiple dilution method (0 to 2000 mg/dL). The refractive index of glucose solutions can be estimated according to the following Equation [46]:

$$n_{glucose}(\lambda) = n_{H_2O}(\lambda) + 1.515 \times 10^{-6} C_{glucose} \quad (2.10)$$

where  $n_{glucose}$  is the refractive index of the aqueous solution of glucose, and  $C_{glucose}$  is the concentration of glucose in mg/dL. These aqueous solutions were used to characterize the performance and sensitivity of our resonators.

### **Bio-Assay Experimental Reagents**

To test the performance and response of the devices to bio-molecules, we used a modified sandwich assay [47, 48] involving well-characterized molecules with high binding affinities including: anti-Streptavidin (antiSA, Vector Labs; Burlingame, CA), streptavidin (SA, Vector Labs; Burlingame, CA), and Biotinylated Bovine Serum Albumen (biotin-BSA, bBSA), which was conjugated per the manufacturer’s instructions using a commercial biotinylation kit (SoluLink; San Diego, CA). During the experiments, the optical stage was thermally controlled at 30°C to minimize thermal drift. Reagents were introduced to the sensor arrays using a reversibly bonded PDMS flow cell and Chemyx Nexus 3000 Syringe Pump (Houston, TX) at 10  $\mu$ L/min. Selected peaks were tracked every 45 seconds using an Agilent 8164A 1550 nm mainframe with a tunable laser (Agilent 81682A) with an integrated detector (Agilent 81635A). Each sensor was exposed to phosphate-buffered saline (PBS) for at least 20 minutes prior to other reagents to establish an initial signal baseline.

## 2.3 Sensor Designs and Calibration Results <sup>2</sup>

Using these metrics, we analyze the performance of ring, disk, and Bragg grating resonators fabricated in SOI, and integrated with microfluidics. We also demonstrate a biosensing experiment.

In addition to investigating these proposed devices at around 1550 nm wavelength, which is commonly used for telecommunication applications, some of these devices are under investigation for wavelengths around 1220 nm. At 1220 nm, light absorption from water is strongly decreased with respect to the 1550 nm range, thus increasing the quality factor and improving the limit of detection [17].

When dealing with resonator sensors, the sensitivity is determined by the shift of the resonant peak wavelength as the refractive index of the solution changes. A set of aqueous solutions of NaCl, as explained in section 2.2.6 is used to characterize the sensor devices under investigation.

Resonator sensors with a high quality factor are desirable. A high quality factor of the sensor means improved accuracy of the detection due to the improved minimum detectable wavelength shift. This will consequently improve the Limit of Detection (LOD) based on equation 2.9.

---

<sup>2</sup>Parts of of this section have been published in [34]:  
S. Talebi Fard, et al., “Label-free silicon photonic biosensors for use in clinical diagnostics”, Proc. SPIE, Silicon Photonics VIII, 8629:86290914 (Invited), SPIE OPTO, International Society for Optics and Photonics, 2/02/2013.

### 2.3.1 Optical Sensor Designs

Optical resonators have shown promises as biosensors due to their longer interaction with the analyte surrounding the resonators. The following resonators have been investigated in our group: disk resonators; slot waveguide ring resonators; strip waveguide Bragg gratings; and slot waveguide Bragg gratings. Figure 2.11 provides an SEM image of each of these resonators. Also, since they are integrated in waveguides, they often have compact footprint and thus are easily integrated with microfluidic channels.

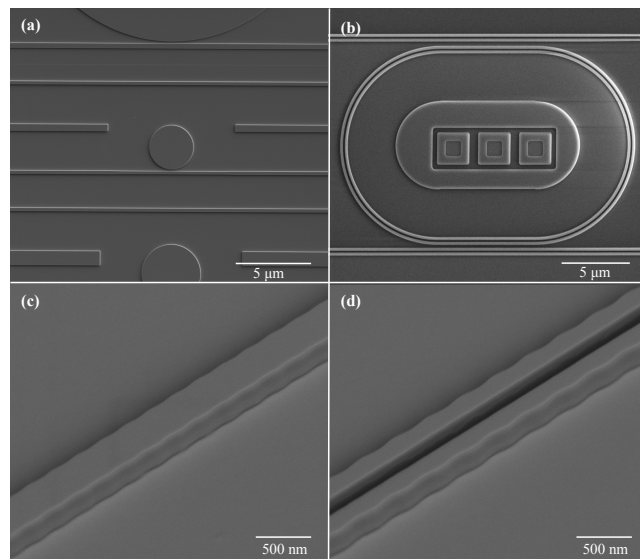


Figure 2.11: SEM images of the fabricated devices on SOI wafers, using E-Beam lithography process at the University of Washington. a) disk resonator; b) slot waveguide ring resonator; c) strip waveguide Bragg grating; d) slot waveguide Bragg grating.

### 2.3.2 Disk Resonators

Disk resonators offer potential advantages of improved limits of detection due to lower scattering losses and thus higher quality factors [17]. The nature of disk resonators means that there is only one sidewall surface from which scattering can occur. These reduced losses increase the resonator quality factor and in doing so have the potential to improve the limit of detection as defined in Equation 2.9. Additionally, disk resonators offer very small device footprints; this is advantageous for multiplexing (many disks can fit in a small area, and the disks offer a wide free spectral range, FSR), and the sensing surface area is comparatively small.

Figure 2.12 shows the schematics of the 10  $\mu\text{m}$  disk resonators and the simulated mode profiles for the first three TE and TM modes.

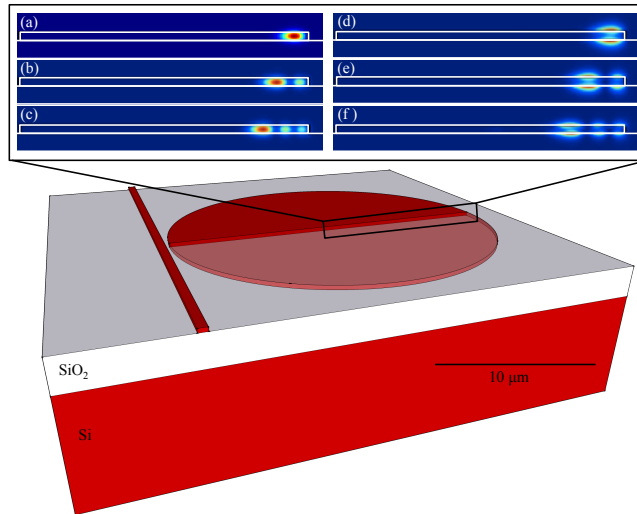


Figure 2.12: Mode profiles (TE and TM) for 10  $\mu\text{m}$  disk resonator. a-c are the first to third TE modes; and d-f are the first to third TM modes.

### 2.3. Sensor Designs and Calibration Results

We have investigated 10  $\mu\text{m}$  disk resonators supporting both TE and TM modes. As Figure 2.12 illustrates, the TM modes in our disk geometries have electric fields that penetrate further into the analyte as well as more field traveling in the analyte itself; this leads to more interaction of light with analyte and therefore higher refractive index sensitivity. The results of the sensitivity analysis of the 3  $\mu\text{m}$  disk are shown in Figure 2.13, demonstrating the peak shift and refractive index sensitivity calibration for the two modes present in the disk.

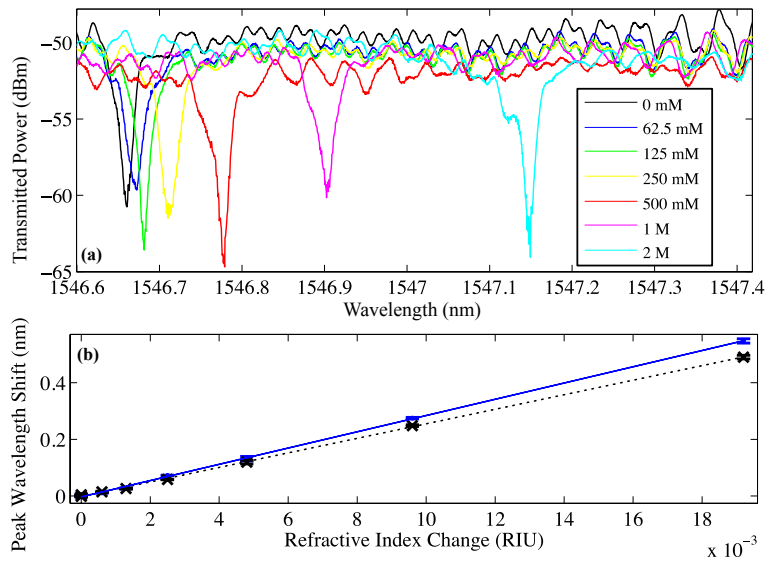


Figure 2.13: a) Shows how the spectra shifts as the refractive index of the medium changes (using various concentrations of NaCl). b) Sensitivity for the fundamental (black) second (blue) TE modes in 3  $\mu\text{m}$  radius disk resonator. The error bars indicate a 99% confidence interval (within 3 standard deviation). We observe sensitivities of 26 nm/RIU for the fundamental mode and 29 nm/RIU for the second mode.

### 2.3.3 Strip Waveguide Bragg Grating

Integrated waveguide Bragg gratings are also promising candidates for biosensors. Compared with other resonant structures (e.g. ring or disk), waveguide Bragg gratings usually operate at only one particular wavelength (Bragg wavelength) and thus are not limited to FSR for the maximum range of the peak wavelength shift.

Figure 2.14 represents a schematic of a strip Bragg grating sensor with phase shift; with inset being the mode profile of the main propagating TE mode. The Bragg gratings are realized with corrugations on the lateral side-walls of the strip. As light travels through the waveguide, the optical mode experiences periodic modulation of the effective refractive index, and the Bragg condition depends on the grating period and the effective refractive index of the medium.

The phase shift region in the strip Bragg grating sensors constructs a cavity with two Bragg reflector mirrors and induces a resonant peak in the stop band of the Bragg gratings. The Q factor of the resonance can be very high (100,000 in air [49] ).

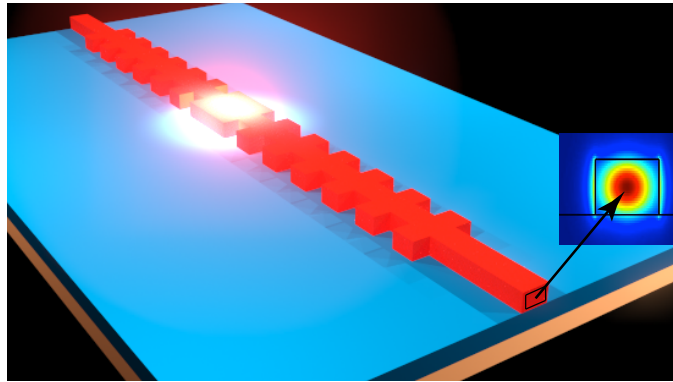


Figure 2.14: Schematic of a strip Bragg waveguide and the propagating TE mode in the waveguide cross-section.

Figure 2.15 shows the experimental results of the sensitivity analysis of strip waveguide Bragg grating sensor. A sensitivity of 59 nm/RIU is measured, which is close to the simulated value of about 55 nm/RIU. The quality factor (Q) of this device is measured to be 27600, which leads to an intrinsic limit of detection of  $9.3 \times 10^{-4}$  RIU.

### 2.3. Sensor Designs and Calibration Results

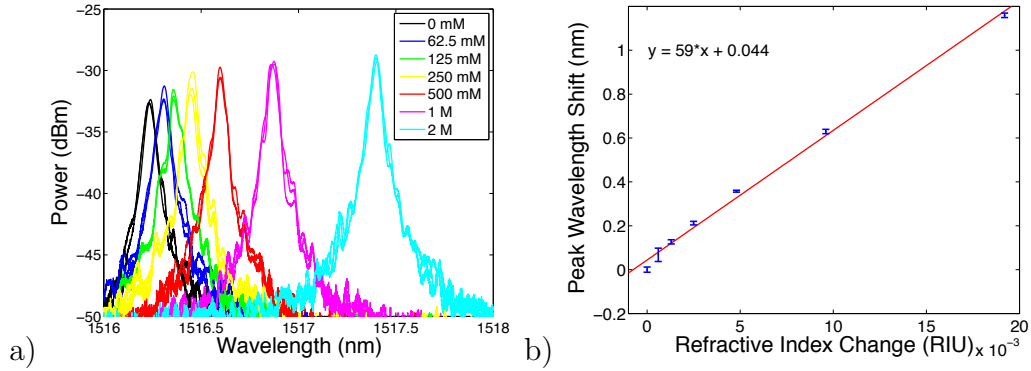


Figure 2.15: a) Shows how the spectra shifts as the refractive index of the medium changes (using various concentrations of NaCl). b) Shows the sensitivity of the strip Bragg sensors. Error bars show experimental results for peak wavelength shift versus refractive index change of the medium. The error bars indicate a 99% confidence interval (within 3 standard deviation). Red line is a linear fit to these points indicating the sensitivity of about 59 nm/RIU.

#### 2.3.4 Slot Waveguide Ring Resonator

A slot waveguide racetrack resonator with a 30  $\mu\text{m}$  radius, 300 nm waveguide widths and 130 nm slot was fabricated and yielded quality factors of about 1450 and sensitivities of 263 nm/RIU. The low Q is partly due to high bending, mode mismatch, and scattering losses. This limited Q suggests that it is necessary to eliminate the bent regions in the slot device in order to obtain high ILODs.

#### 2.3.5 Slot Waveguide Bragg Grating

To enhance the light-analyte interaction, we also applied the phase-shifted Bragg grating structure in a slot waveguide [50], as shown in Figure 2.16.

### 2.3. Sensor Designs and Calibration Results

---

The electric field of the slot waveguide is concentrated inside the small low-index slot region. This unique property makes the slot waveguide much more sensitive to the surrounding fluidics than conventional strip waveguides that use only weak evanescent field tails. The Bragg gratings are constructed by corrugating the outer sidewalls of the slot waveguide, where the evanescent field decays.

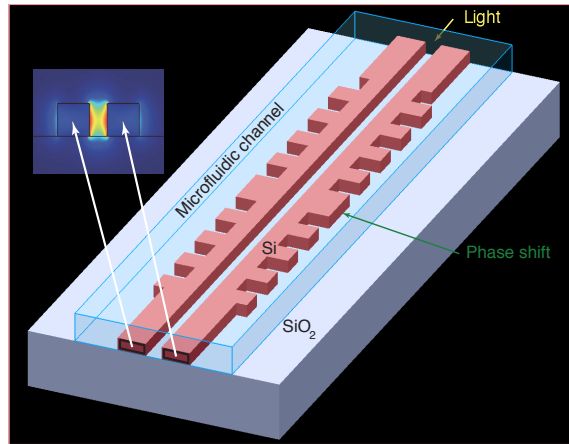


Figure 2.16: Schematic of a slot Bragg waveguide and the propagating TE mode in the waveguide cross-section.

Figure 2.17 shows the experimental results of the sensitivity analysis of a slot waveguide Bragg grating sensor. A sensitivity of 340 nm/RIU is measured, which is in excellent agreement with simulation results [30]. The quality factor (Q) of this device is measured to be about 15000, which leads to a limit of detection of  $3.0 \times 10^{-4}$  RIU. Compared to the slot waveguide ring resonators, the slot Bragg grating resonators exhibit significantly enhanced Q factors since they do not suffer from the bending and mode mismatch losses as in ring structures.

## 2.4. Biological Results

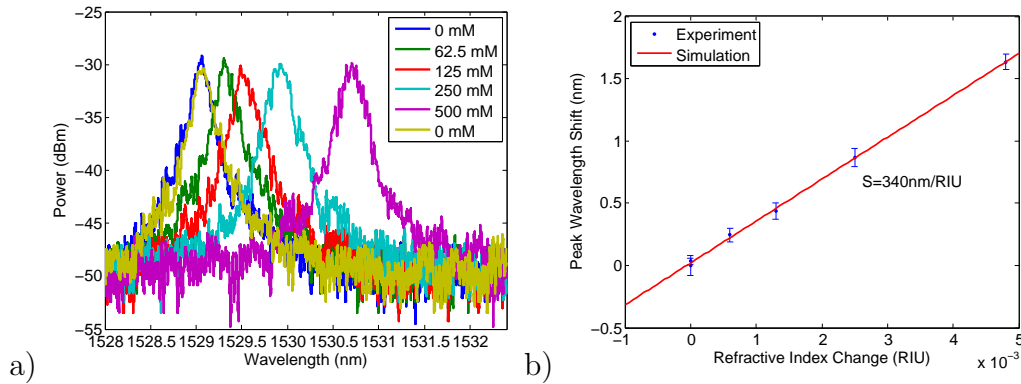


Figure 2.17: a) Shows how the spectra shifts as the refractive index of the medium changes (using various concentrations of NaCl). b) Shows the sensitivity of the Slot Bragg Sensors. Error bars show experimental results for peak wavelength shift versus refractive index change of the medium. The error bars indicate a 99% confidence interval (within 3 standard deviation). Red line is a linear fit to these points indicating the sensitivity of about 340 nm/RIU.

## 2.4 Biological Results

As a first step towards demonstrating the sensor's biosensing capabilities, we performed a modified "sandwich" assay using streptavidin (SA) as a model protein and its binding partners, biotin and a monoclonal anti-SA antibody. For the purposes of this study, these molecules were selected based on their availability and ease of use. Additionally, it is worth noting that the specific molecular recognition event between SA and biotin is one of the strongest non-covalent bonds known [51] and anti-SA has been used to demonstrate specific binding to immobilized SA on silicon photonic sensors previously [52].

Figure 2.18 shows results from the biosensing experiments for a 3  $\mu\text{m}$  radius TE-mode resonant disk and a single-waveguide Bragg interferometer

## 2.4. Biological Results

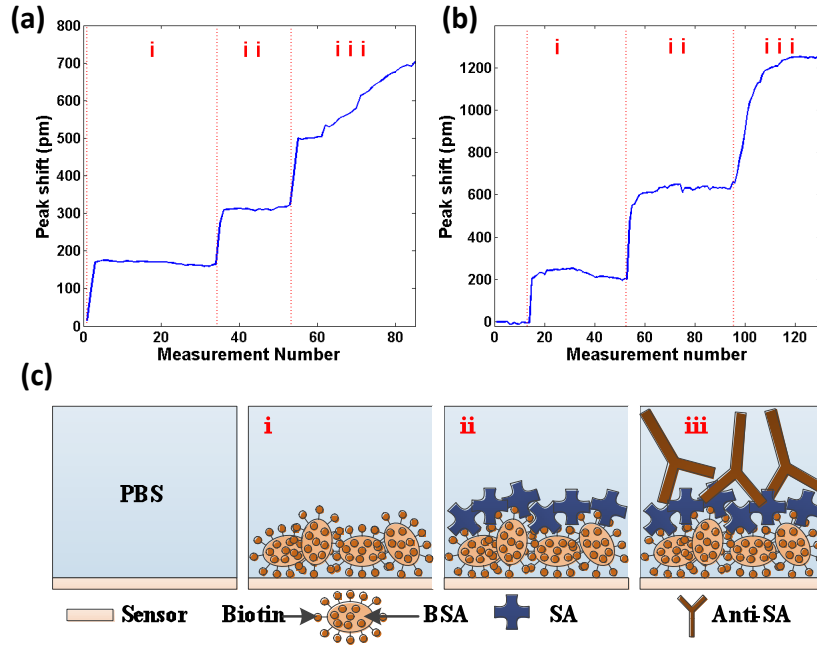


Figure 2.18: Wavelength shift during biosensing demonstration for the  $3 \mu\text{m}$  radius TE-mode disk sensor (a) and single waveguide Bragg interferometer sensor (b). (c) Illustrates reagent sequencing corresponding to regions [i, ii, and iii] in (a) and (b). Region i = Biotinylated Bovine Serum Albumen (b-BSA) ( $2 \text{ mg/mL}$ ), ii = streptavidin (SA) ( $1.8 \mu\text{M}$ ), iii = anti-streptavidin (anti-SA) ( $125 \mu\text{g/mL}$ ). A PBS-wash preceded and followed the introduction of each reagent in steps i-iii.

sensor. Wavelength shifts resulting from the molecular binding events for the disk resonator and Bragg sensor are shown in Figure 2.18 (a and b) respectively. Figure 2.18 (c) illustrates the idealized sequence of molecular interactions resulting in the sandwich assay. These sequential binding interactions correspond to the wavelength shifts shown in regions i, ii, and iii shown in Figure 2.18 (a, b).

After establishing a signal baseline in PBS buffer, biotinylated-BSA (b-BSA) was adsorbed to the oxide of the sensor surface (shown in region i in

Figure 2.18 (a, b)). Next, SA was introduced to the functionalized sensor, binding irreversibly to the immobilized b-BSA, resulting in the wavelength shift observed in region ii (Figure 2.18 (a, b)). Finally, Anti-SA bound the capture SA, serving as a final signal amplification step, resulting in the additional resonant peak shift shown in region iii (Figure 2.18 (a, b, and c)).

These binding results are in good agreement with the formation of a multilayer biomolecular system consisting of b-BSA, SA and anti-SA. Ideally, the refractive index change (and subsequent wavelength shift) resulting from each additional layer would correlate precisely to the molecule's mass of each protein. However, steric hindrance due to dense molecular packing limits 1:1 stoichiometries of binding. This, coupled with the exponential decay of the evanescent sensing field, causes the sensor's response to each adlayer to deviate from the ideal. With those limitations in mind, the sandwich assay clearly demonstrates expected responses to the biological interactions and demonstrates the platform's suitability for interrogating molecules in other multi-layer biological assays.

## 2.5 Discussion and Analysis

Table 2.2 presents a summary of geometrical specifics, resonance wavelengths and light polarizations, as well as sensing performance in terms of Q, S, and ILOD (equations 2.5, 2.6, 2.8, and 2.9) of our fabricated SOI sensors. In addition, Figure 2.19 presents a comparison of the limits of detection and

## 2.5. Discussion and Analysis

---

sensitivities of devices summarized in Table 2.2 to our previously-presented devices [17] and to limits of detection of various sensor configurations reported in literature. The blue line on Figure 2.19 represents the theoretical limit to the obtainable sensor performance (in water).

Table 2.2: Summary of the performance and characteristics of our silicon photonics sensors

Sensor	Specifications	$\lambda$ (nm)	TE/TM	$Q_{water}$	S ( $\frac{nm}{RIU}$ )	ILOD (RIU)
Disk	3 $\mu\text{m}$ radius	1527	TE	32300	26	$1.8 \times 10^{-3}$
Disk	10 $\mu\text{m}$ radius	1512	TE	131000	21	$5.5 \times 10^{-4}$
Disk	10 $\mu\text{m}$ radius	1543	TM	16000	142	$6.8 \times 10^{-4}$
Slot Ring	30 $\mu\text{m}$ radius	1500	TE	1450	263	$1.3 \times 10^{-2}$
Strip Bragg	0.5 $\mu\text{m}$ width $\sim 112 \mu\text{m}$ length	1517	TE	27600	59	$9.3 \times 10^{-4}$
Slot Bragg	0.5 $\mu\text{m}$ width $\sim 112 \mu\text{m}$ length	1530	TE	15000	340	$3.0 \times 10^{-4}$

It is worth noting that the lowest limits of detection (about one order of magnitude less than other sensor configurations) are achieved with the TE and TM modes [28] in the 10  $\mu\text{m}$  radius disks as well as the slot Bragg grating resonator sensors. On the other hand, their refractive index sensitivities vary by an order of magnitude (with TM disk and the slot Bragg with better performance), but their different quality factors equalize the limits of detection to the same order of magnitude. Concerning Bragg sensors, they both have a very low limit of detection and high Q, but the sensitivity is about 6 times improved for the configuration with the slot waveguide. This is likely

## 2.5. Discussion and Analysis

---

due to an enhanced interaction between the electromagnetic field and light, causing a wider shift of its resonance wavelength. We can observe in Figure 2.19 that Q factor of slot Bragg is very close to the theoretical limit, so one can conclude that it is mainly limited by the water absorption.

In addition to ILODs, often resonator characteristics can influence the choice of best resonator type for a given application. Depending on the shape and size of the microchannels, number of multiplexed sensors, as well as shape of target molecule, one can determine the best sensor for the particular application. For example, the 3  $\mu\text{m}$  radius disks have the smallest footprint, while Bragg sensors have long but very narrow shape; this perhaps makes 3  $\mu\text{m}$  disks better suited for multiplexing applications. Indeed, the ultimate best choice of sensor type will be dictated by the requirements of the application; whether sharp peaks or large peak shifts are preferable, whether it is advantageous to track multiple peaks at the same time. Obviously, the sizes and expected concentrations of the analyte or of the specific target molecule will all play a role in determining the best sensor type. For example, slot waveguides may be better suited for sensing small molecules with low concentrations, because they offer high sensitivity, but they require that molecules can flow also in the slot (that has a cross section of 150 nm  $\times$  220 nm), where much of the field is concentrated.

## 2.6. Conclusion and Future Work

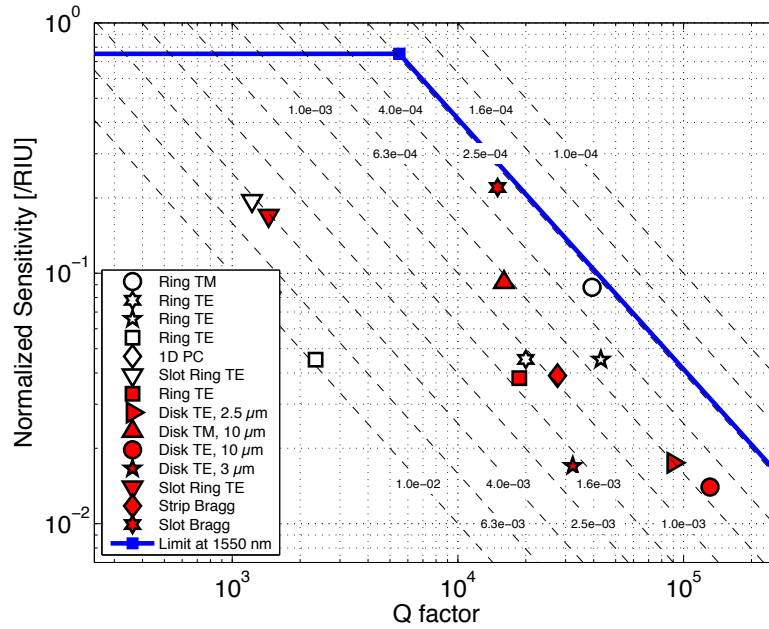


Figure 2.19: Experimental results for performance and figure of merit (ILOD) of various sensors. All the red filled points are devices developed by our group at UBC/UW; and black hallowed ones represent devices developed in other groups [9, 27, 29, 53–55] for comparison purposes. The y-axis is the sensitivity normalized to the peak resonant wavelength (equation 2.4). The blue line is the theoretical limit for 1550 nm in water.

## 2.6 Conclusion and Future Work

In this section, we have discussed the emerging and promising role of integrated optical biosensors, and we described various individual resonator sensors that have been modelled and fabricated by our group. Those sensors have been characterized and validated using a standard ‘sandwich’ assay. Having variety of sensors characterized have prepared us for performing more meaningful bio-assay experiments using more custom designed sensors to detect essential aspects under study.

## 2.6. Conclusion and Future Work

---

Having sensors with small footprints, it would be very easy to have high-throughput multiplexed and simultaneous analysis, with hundreds of sensors each-one ‘tuned’ for a different specific target. All those sensors can be designed and aligned such that they can be easily integrated with microfluidic channels, as well as they can have built-in normalization with integrated reference sensors. Considering that all those sensors would be fabricated with standard SOI chip processes that are CMOS compatible, facilitating integration with on-chip electronics, they would be very promising in terms of whole systems integration. Furthermore, our integration of these devices with microfluidics and bioassays represents a step forward towards realizing Lab on Chip systems.

A final remark on the wavelength we have used, that is 1550 nm, commonly used for telecommunications, thus it has been very well characterized and offers several low-cost components. Since our aim is biological sensing, it is worth exploring different wavelength regions, which may offer some advantages or the possibility of gaining multi-wavelength information. For example we are start to investigate 1220 nm as a working wavelength, since it presents a significantly reduced water absorption, which in turn may improve the figure of merit, ILOD. As seen in the work by Chrostowski et al. (Figure 8b)[17], the detection limit is lower at around 1220 nm compared to 1550 nm, making the wavelength window of 1.2 to 1.3  $\mu\text{m}$  a more desirable range for sensing applications in the presence of water.

# Chapter 3

## Ultra-Thin Resonator Sensors <sup>3</sup>

This chapter presents simulation and experimental results of ultra-thin optical ring resonators, having larger Evanescent Field (EF) penetration depths, and therefore larger sensitivities, as compared to conventional Silicon-on-Insulator (SOI)-based resonator sensors. Having higher sensitivities to the changes in the refractive indices of the cladding media is desirable for sensing applications, as the interactions of interest take place in this region. Using ultra-thin waveguides (<100 nm thick) shows promise to enhance sensitivity for both bulk and surface sensing, due to increased penetration of the EF into the cladding. In this work, the designs and characterization of ultra-thin resonator sensors, within the constraints of a multi-project wafer service that offers three waveguide thicknesses (90nm, 150nm, and 220nm), are presented. These services typically allow efficient integration of biosensors with on-chip detectors, moving towards the implementation of lab-on-chip (LoC) systems. Also, higher temperature stability of ultra-thin resonator sensors were characterized and, in the presence of intentional environmental (temper-

---

<sup>3</sup>Parts of of this chapter have been published in [35]:  
S. Talebi Fard, et al., "Performance of ultra-thin SOI-based resonators for sensing applications." *Optics Express* 22, no. 12 (2014): 14166-14179.

ature) fluctuations, were compared to standard transverse electric SOI-based resonator sensors.

### 3.1 Introduction and Background

As described in section 2.3, our group has previously compared the ILODs of waveguide-based resonator sensors fabricated in silicon-on-insulator (SOI) operating near wavelength of  $\lambda = 1550$  nm. Ring [17], disk [28], and Bragg grating [30] resonators have been demonstrated with ILODs approaching the theoretical limit (due to the optical absorption of water) of  $2.5 \times 10^{-4}$  RIU [17].

One technique for improving the performance of a waveguide-based resonator sensor is to increase its sensitivity,  $S$ . This can be done by increasing the interaction between the propagating optical mode and the cladding medium, since the sensing mechanism relies upon the interaction of the evanescent tail of the guided mode in the waveguide with molecules in the cladding medium. When a larger portion of the optical field travels outside of the silicon waveguide core, both the mode sensitivity ( $S_{mode}$ ) and  $S$  increase, resulting in a larger shift in the resonant wavelength. This also results in higher loss due to the optical absorption of water, resulting in a lowered  $Q$ , and, thus, there is a trade-off that results in limited improvements in the ILOD.

The use of thinner waveguide cores was proposed to increase the interac-

tion of the EF of the optical mode with the cladding. Theoretical analysis [56, 57] demonstrates that thinner SOI waveguide cores are more responsive (have higher sensitivities) both to bulk cladding concentrations and thin adsorbed biomolecule layers. Analysis to determine the optimum waveguide thicknesses for specific biological applications has also been performed [56, 57]. In addition, thin and ultra-thin waveguides have been fabricated in CMOS-compatible processes and exhibited low losses; for example a loss of about 2 dB/cm was reported for a 50 nm thick strip waveguide [58]. Ultra-thin waveguide resonator sensors (based on using ultra-thin silicon cores) also offer the potential for improved thermal stability for biosensing applications. The refractive indices of the silicon core and silicon dioxide (buried oxide, BOX) materials increase with increasing temperature [59, 60], while the index of the water cladding decreases with increasing temperature [61, 62], thus moving more of the propagating field to the cladding decreases the overall effect of temperature on the modal effective index.

This chapter includes the first experimental demonstration of ultra-thin waveguide resonator sensors fabricated in a CMOS-compatible SOI process. We have successfully simulated, fabricated, and tested ultra-thin waveguide resonators using waveguide core thicknesses (90 nm) available in commercial Multi Project Wafer (MPW) runs offered by Optoelectronic Systems in Silicon (OpSIS) and/or CMC Microsystems fabricated by the Institute of Microelectronics (IME) in Singapore. We focused on these thicknesses as they offered the best potential for integration with future CMOS-compatible

processes. Using both simulated and experimental results, we have demonstrated that ultra-thin ring resonators have higher sensitivities to the changes in cladding medium and lower sensitivities to temperature. We also compared these ultra-thin resonators with standard 220 nm thick ring resonators and observed significantly more stable responses.

These sensors were tested with glucose solutions, from which a prediction model was created to predict glucose concentrations. These sensors could also be used to study molecular bindings for chemical and biological research purposes [9].

## 3.2 Design Methods and Analysis

We have used Lumerical MODE Solutions and analytical models in MATLAB to design optical resonators with various thicknesses. MODE is used to calculate the effective index for each waveguide thickness and, ultimately, the change in effective index as the cladding is altered. In these MODE simulations, a  $4 \times 4 \mu\text{m}$  simulation area was used. This results in errors less than  $10^{-7}$  in calculations of effective index ( $n_{\text{eff}}$ ) based on the convergence test (figures 2.3 and 2.4). The resulted errors in sensitivity calculations are insignificant ( $< 0.1\%$ ). Figures 3.1(a-c) illustrate the mode profile of the propagating TE fundamental mode for waveguide thicknesses of 220, 150, and 90 nm.

The thinner the waveguides, the less confined are the propagating modes

### 3.2. Design Methods and Analysis

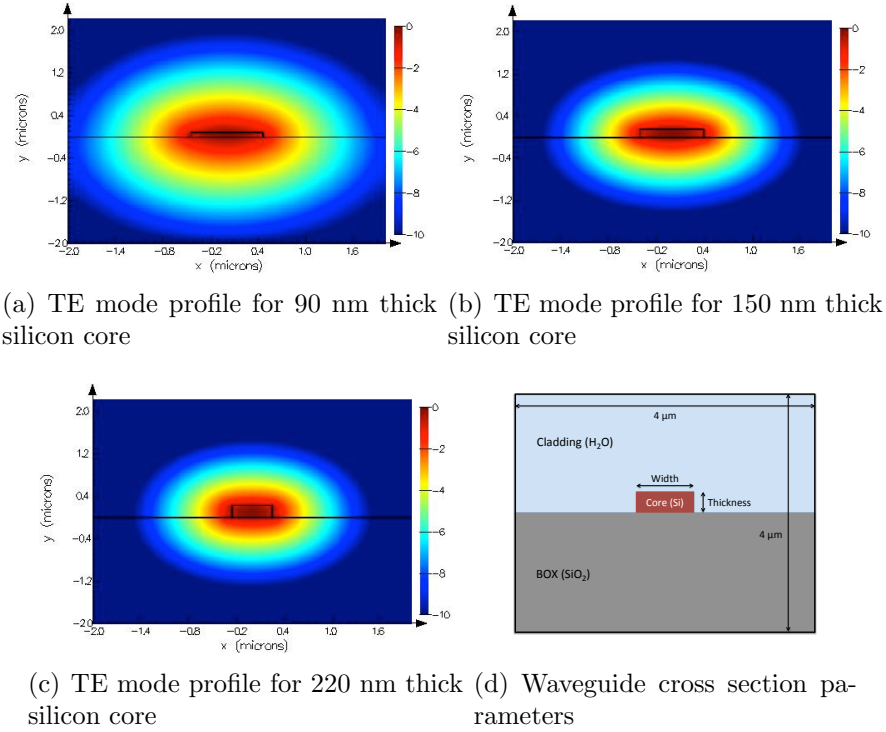


Figure 3.1: Simulation results for the cross-section of the silicon waveguides (SOI) with water as the cladding medium. (a-c) the mode profile of the fundamental TE mode for silicon thicknesses of 220, 150, and 90 nm, in log scale, calculated using MODE Solutions. (d) Schematic of the waveguide's cross section and parameters.

to their silicon cores and the higher are their penetration depths into the surrounding media. The evanescent field in the top cladding at the centre of the silicon slab can be approximated by:

$$E(d) \approx E_0 e^{-d \left( \frac{2\pi}{\lambda_0} \right) \sqrt{N_{\text{eff}}^2 - n_{\text{cl}}^2}} \quad (3.1)$$

where  $E_0$  is the electric field at the surface of the silicon core,  $d$  is the perpendicular distance from the surface,  $N_{\text{eff}}$  is the effective index of the waveguide,

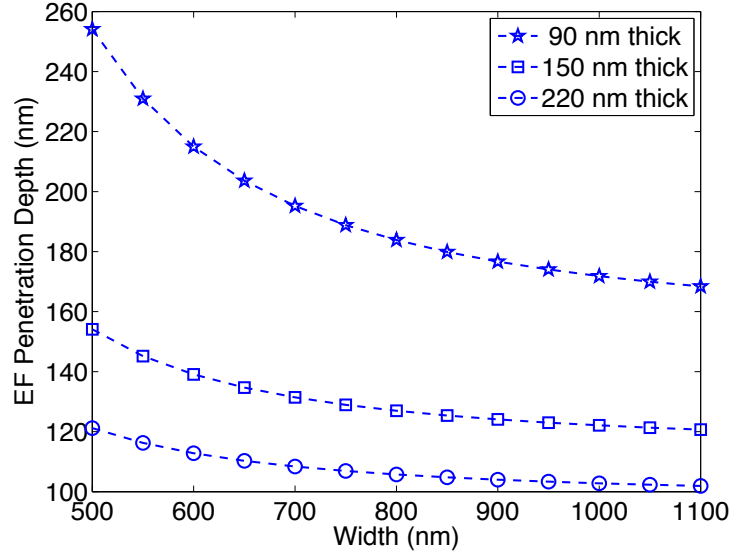


Figure 3.2: Simulated  $1/e$  penetration depths of the evanescent field of the first guided TE mode into the solution for various waveguide core thicknesses and widths.

$n_{cl}$  is the refractive index of the cladding, and  $\lambda_0$  is the operating wavelength.

The penetration depth ( $d_e$ ) is defined as the distance from the silicon-cladding interface (at the centre of the silicon) at which the evanescent field decays to  $E_0/e$ . This penetration depth ( $d_e$ ) of the mode is calculated using MODE and Equation 3.1 for the waveguide thicknesses under investigation, and is plotted in Figure 3.2.

Racetrack resonators are usually designed and optimized at critical coupling, resulting in maximum Extinction Ratio (ER). Analytical modelling in MATLAB is used to calculate the parameters and predict the response of the ring resonator, to achieve an optimal design. This model considers estimated and simulated losses as well as simulated mode profiles for various

sections of racetrack in the calculations. The simulation area of  $4 \times 4 \mu\text{m}$ , assuming a standard SOI wafer (with 2 or  $3 \mu\text{m}$  of  $\text{SiO}_2$  BOX between the waveguide and silicon substrate), includes the waveguide core, its  $\text{SiO}_2$  BOX and cladding. Propagation losses (scattering loss + substrate leakage) were estimated to calculate the critical coupling lengths for racetrack resonators. Researchers have investigated these losses, analytically and experimentally. They reported a substrate leakage of 1 dB/cm for 100 nm slab waveguide over a  $1 \mu\text{m}$   $\text{SiO}_2$  BOX [63], and a substrate loss of 3-4 dB/cm for a  $500 \times 120$  nm waveguide over  $1.4 \mu\text{m}$   $\text{SiO}_2$  BOX [64, 65] (with reported total loss of 7 dB/cm for racetrack structure). In addition, a propagation loss of 2 dB/cm for a  $500 \times 50$  nm waveguide on a standard SOI wafer is reported [58]. It has been demonstrated that the losses due to substrate leakage decreased exponentially as the thickness of the oxide layer increased [31, 63]. Propagation losses, both scattering loss and substrate leakage, decreased as the waveguide width increased (higher mode confinement) [31, 66]. Therefore, for our case with a standard SOI wafer (with 2 or  $3 \mu\text{m}$  of  $\text{SiO}_2$  BOX) and wider waveguides, we assumed a total propagation losses of 2-5 dB/cm.

Based on the higher simulated sensitivities for ultra-thin 90 nm resonator sensors, we decided to fabricate a few variations of these ultra-thin sensors as well as conventional 220 nm thick resonators for comparison purposes. In this research, resonators with radii of 10, 20, and  $30 \mu\text{m}$  and waveguide widths of 800 nm to 950 nm were designed for critical coupling, in order to achieve the best ER and optimized response. The goal was to use 90 nm waveguide

cores, the thinnest offered by the standard MPW foundries. When using ultra-thin waveguides, a wider silicon core is necessary to guide the mode and has the advantage of reduced scattering losses due to sidewall roughness [58]. These reduced losses result in slightly higher  $Q$  values, but slightly lower sensitivities (as a small portion of the evanescent field is travelling outside of the core). This trade-off between  $Q$  and  $S$  leads to an optimum point for the ILOD. In addition, the single mode conditions for waveguides with 90 nm silicon cores are not disturbed until the waveguide widths reach 900 nm, after which the waveguides are multi-mode.

### 3.2.1 Sensitivities of TE Resonator Sensors to Cladding Refractive Indices

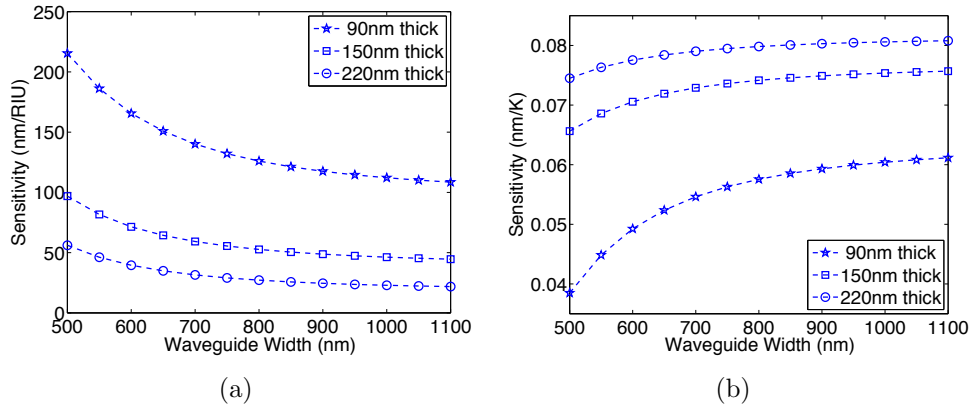


Figure 3.3: Sensitivities of TE waveguide resonators with various thicknesses to (a) the analyte in the cladding medium and (b) to the temperature

An EF sensor operates by detecting changes in the effective index of

the waveguide. The effective index of the waveguide can be affected by a change in the refractive index of the core and the refractive index of the BOX and/or the refractive index of cladding. We are most interested in the change in effective index of the waveguide as a function of the change in refractive index of the analyte in the cladding medium (equations 2.1 and 2.5).

If thinner cores are used in resonators, the mode is less confined to the core and a larger portion of the evanescent field travels outside the core, resulting in more interaction with the cladding. Therefore, the dependence of the effective index of the waveguide on the refractive index of the cladding medium is increased in thinner waveguides, resulting in higher sensitivity. MODE is used to calculate the effective index of strip waveguides with various widths, thicknesses, and claddings. For each case, the change in effective index as a function of the refractive index of the cladding is calculated. We then use the sensitivity relation for resonators (equation 2.5) to find the estimated sensitivity for each case at  $\lambda_0 = 1550$  nm. Figure 3.3(a) shows the sensitivity that can be achieved in a strip waveguide resonator for three waveguide thicknesses: 90, 150, and 220 nm.

An ideal optical sensor will have high sensitivity ( $S$ ) to cladding refractive index changes and low sensitivity to other factors such as temperature variation or system noise.

### 3.2.2 Sensitivities of TE Resonator Sensors to Temperature Variations

The sensitivity of a TE resonator sensor to temperature is defined as the wavelength shift in resonator's response caused by a temperature change of the waveguide (core, buried oxide, and cladding). The change in refractive index as a function of a change in temperature ( $\frac{dn}{dT}$ ) for silicon can be approximated for T around 295 K, and  $\lambda_0$  around 1.5  $\mu\text{m}$ , to be  $\frac{dn}{dT} \approx 1.8 \times 10^{-4}/\text{K}$  [59, 60]. Since the waveguide thickness is changing in our study, the contribution of the temperature variation of the silicon dioxide ( $\text{SiO}_2$ ) BOX would be significant and different for each case. Therefore, the sensitivity is estimated assuming that the temperature of the substrate and BOX is changing by the same amount as the temperature of the core. The sensitivity of the refractive index of silicon dioxide to temperature is about  $\frac{dn}{dT} \approx 2.8 \times 10^{-5}/\text{K}$  [44]. Most solutions used for biological applications are aqueous. The dependence of the refractive index of water to temperature is  $\frac{dn}{dT} \approx -9.9 \times 10^{-5}/\text{K}$  [61, 62]. Table 3.1 shows the summary of these thermo optics (TO) coefficient values. Figure 3.3(b) shows the sensitivity of strip waveguide resonators to temperature variations of waveguide (when the cladding is water).

## 3.3 Experimental Methods and Materials

The above mentioned designed ultra-thin racetrack resonator sensors were fabricated on a SOI chip using the E-Beam Lithography (EBL) System at

### 3.3. Experimental Methods and Materials

Table 3.1: Thermo optics coefficient of the materials in the system

Material	TO coefficient $\frac{dn}{dT} \left(\frac{1}{^{\circ}C}\right)$
Si waveguide	$1.8 \times 10^{-4}$ [44, 59, 60, 67]
Water (cladding)	$-9.9 \times 10^{-5}$ [61, 62]
SiO <sub>2</sub> (BOX)	$2.8 \times 10^{-5}$ [44]

the University of Washington - Washington Nanofabrication Facility (UW WNF). Figure 3.4 shows SEM images of two of these sensors. On-chip Grating Couplers (GCs) are used to couple light into and out of the SOI chip [68]. These sensors were tested using techniques and reagents described in section 2.2.

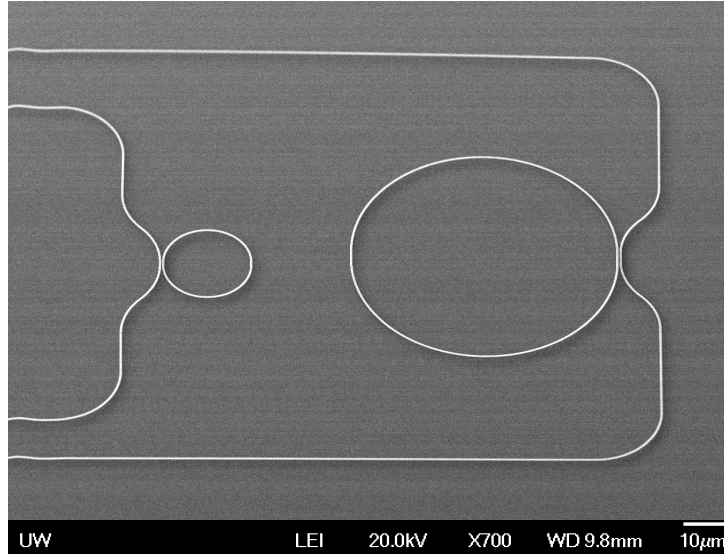


Figure 3.4: SEM image of ultra-thin TE resonator sensors for two radii of 10  $\mu\text{m}$  and 30  $\mu\text{m}$ , fabricated on SOI wafers, using E-Beam lithography process at the University of Washington

## 3.4 Performance of the Ultra-Thin TE Resonator Sensors

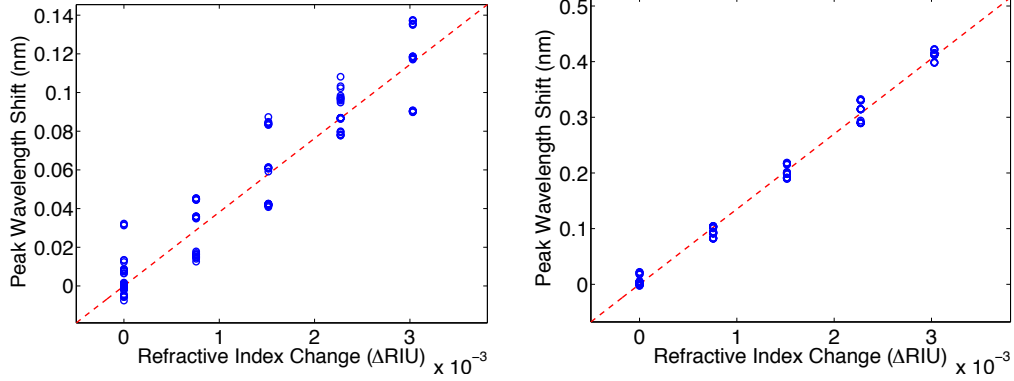
In this section, we report on the performance of our fabricated devices.

### 3.4.1 Sensitivity Analysis Results

The optical responses of two ring resonators, one with the standard 220 nm thick silicon core and one with 90 nm ultra-thin silicon cores, in the presence of the various glucose concentrations (section 2.2.6) were measured. These two devices were measured consecutively in the presence of the same solutions under the same experimental conditions. These experiments were repeated on three days, at three different temperatures between 298 and 299 K inclusive, therefore subjected to an intentional temperature variations of 1 K. From the data, the wavelength shifts as functions of the change in refractive index of the glucose concentrations were calculated and plotted for both sensors.

Figure 3.5 summarizes the wavelength shift responses of our two sensors, in the presence of the various concentrations of analyte, and plots these shifts as functions of refractive index change. The slopes of the best linear fits to these points represent the sensitivities in nm/RIU, which is the peak wavelength shift as a function of refractive index change. Figure 3.5(a) is the response of the traditional 220 nm thick resonator sensor, and Figure 3.5(b) is the response of a 90 nm ultra-thin resonator sensor. The slope of

### 3.4. Performance of the Ultra-Thin TE Resonator Sensors



(a) Measured sensitivity of a 220 nm thick TE sensor  
(b) Measured sensitivity of a 90 nm ultra-thin TE sensor

Figure 3.5: Peak wavelength shift as a function of the change in refractive index of the glucose solutions. There are about 25 measurements for each concentration (i.e. each refractive index point), measured over three days subjected to intentional temperature variations of 1 K. The dashed line is the best linear fit to these measurements, representing the sensitivity in nm/RIU. The estimated sensitivities based on these linear fits for (a) is 38.2 nm/RIU and for (b) is 133 nm/RIU.

the dashed lines in Figures 3.5(a,b) is the sensitivity of these sensors that are 38.2 and 133 nm/RIU for the standard 220 nm thick and 90 nm ultra-thin resonator sensors, respectively. The wavelength shift in the 220 nm thick resonator shows strong perturbations (large errors) due to environmental variations such as temperature (average variations of 1 K were induced) or noise, whereas the wavelength shift in the 90 nm ultra-thin resonator sensor shows a strong linear relation with the changes in the refractive index of the analyte; i.e. lower sensitivity to temperature and noise. It is evident that the ultra-thin resonator sensor shows higher sensitivity as well as better stability (significantly smaller errors). Having higher sensitivity and better stability

### 3.4. Performance of the Ultra-Thin TE Resonator Sensors

---

allows improved predictions. Note that the temperature was varied in these experiments to demonstrate and compare the performance of the sensors in the presence of intentional temperature variation; the errors are due to these variations. In typical experiments, where the temperature is not varied, the errors are significantly smaller (Figure 3.7).

To further demonstrate the lower sensitivity of ultra-thin resonators to temperature variations, and to characterize the temperature sensitivity of these sensors, the responses of the sensors at three different temperatures were measured and the corresponding resonant wavelength shifts were plotted as functions of temperature change. The shift in resonant wavelength as a function of temperature ( $\frac{d\lambda}{dT}$ ) denotes the sensitivity of a sensor to temperature. Figure 3.6 shows the experimental results for the temperature sensitivity of a 220 nm thick and a 90 nm ultra-thin resonator sensor, to be 69 and 49 pm/K respectively.

One potential application of these sensors is the use of their bulk sensitivity in predicting concentrations of analyte in their cladding medium. Figure 3.7 shows the results of using linear models, based on their sensitivities and measured wavelength shifts, to predict the concentrations of the analyte in the cladding medium using our two sensors. The red (light) error bars show the prediction results using the conventional 220 nm thick resonator with the goodness of prediction ( $R^2$  value) of 0.85, and the thick black error bars are the result of predictions using the ultra-thin resonator sensor, with an  $R^2$  value of 0.993. The error bars are the result of intentional temperature

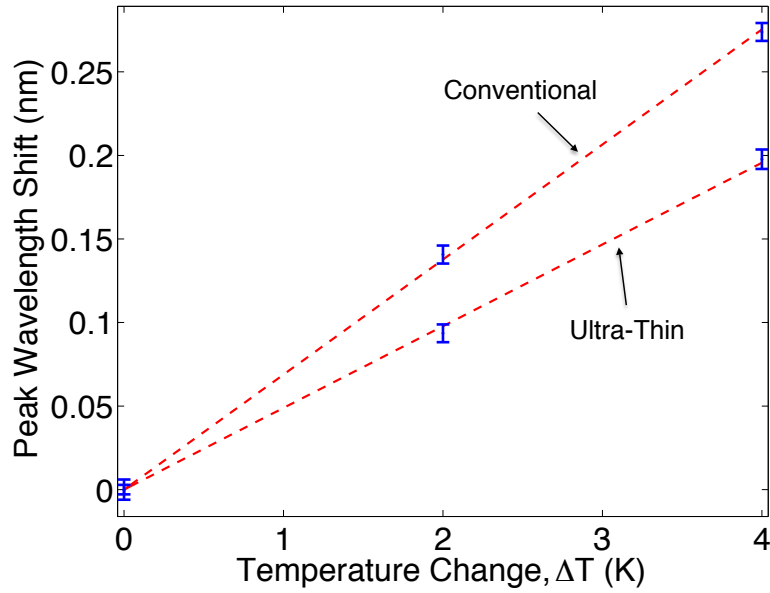


Figure 3.6: Peak wavelength shift as a function of temperature change, demonstrates the sensitivity of our sensors to temperature change. Sensitivities of the 220 nm thick (conventional) and 90 nm ultra-thin resonators are measured to be 69 and 49pm/K, respectively.

variations of 1 K. Temperature controlling these sensors would significantly reduce the error bars, and the  $R^2$  value for ultra-thin sensors increasing to 0.998 (figure 3.8). Figure 3.7 demonstrates significant improvement in ultra-thin resonator's ability to measure glucose concentrations in the presence of temperature variations, as compared to conventional 220 nm thick sensor.

### 3.4. Performance of the Ultra-Thin TE Resonator Sensors

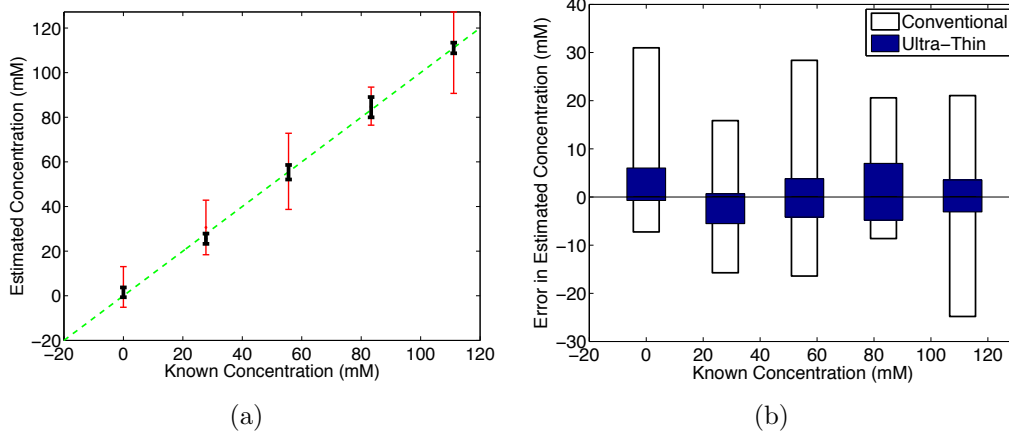


Figure 3.7: The results of predictions of glucose concentrations using the two characterized sensors based on their responses on two different days under intentional temperature fluctuations of about 1 K. a) The red (light) error bars show the predicted results using the 220 nm thick resonator ( $R^2 = 0.85$ ), and the thick black error bars show the predicted results using the 90 nm ultra-thin resonator sensor ( $R^2 = 0.993$ ). b) The bars represent the error in predicted concentrations using our two sensors. The bars are based on the maximum +/- errors.

#### 3.4.2 Q Factor and Intrinsic Limit of Detection (ILOD)

The  $Q$  factor of an optical waveguide resonator, being a measure of number of optical oscillations until the resonating energy decays to  $1/e$  of its max value, is defined in Equation 2.6. This approximation is used to measure the  $Q$  values of our devices studied in this chapter. The  $Q$  of a resonator is inversely proportional to the losses that are affecting the propagating mode (equation 2.6). Various loss components contribute to the  $Q$  factor in ring resonators: scattering loss, bend loss, mode-mismatch loss, radiation loss in bends, and material absorption, including water absorption. The  $Q$  factor is lower in

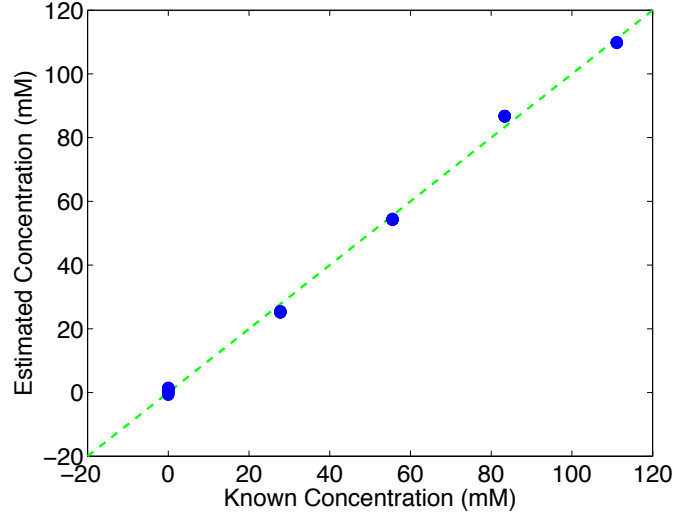


Figure 3.8: The results of predictions of glucose concentrations using ultra-thin resonator sensors at constant temperature ( $R^2 = 0.998$ ). The light dashed line is for: Estimated Concentrations = Known Concentrations.

the thinner waveguide resonators, because of their higher losses due to their increased interaction with the biomolecules in the cladding medium. These increased interactions are desirable for sensing applications. The highest  $Q$  factor that was achieved by the ultra-thin resonators in water was around 24,000, and the maximum Extinction Ratio (ER) measured was 28 dB.

Figure 3.9 summarizes the modelling and experimental results of the EF sensors, presenting the intrinsic limit of detection of the EF sensors as functions of their  $Q$  factors and normalized sensitivities. The thin black dashed lines represent contours of constant ILOD. The thick light blue line is the theoretical limit of detection for (unloaded) resonant sensors due to water absorption at 1550 nm [17]; its locus represents different proportions of light travelling in the water versus in the waveguide core, namely a high  $Q$  / low

### 3.4. Performance of the Ultra-Thin TE Resonator Sensors

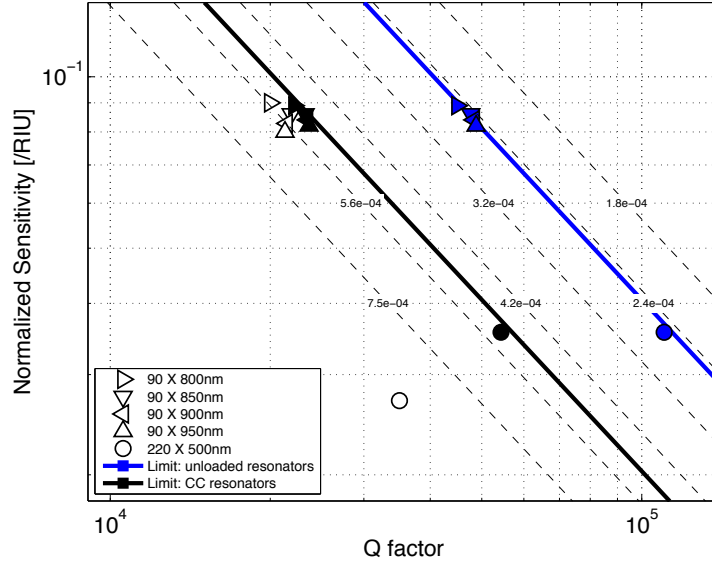


Figure 3.9: The intrinsic limit of detection (ILOD) of the silicon photonic evanescent field sensors, as functions of the normalized sensitivity ( $S^*$ ) and quality factor ( $Q$ ). The thin black dashed lines represent contours of constant ILOD. The thick light blue line is the theoretical limit of detection for (unloaded) resonant sensors due to water absorption at 1550 nm [17]. The corresponding light blue markers are the modelling results for the specific unloaded resonators considered in this study, where only optical absorption due to water around the waveguide is considered. The thick black line is the theoretical limit for a critically coupled (CC) resonator. The corresponding black markers are the modelling results for critically coupled resonators, where the  $Q$  factor is determined from the simulated optical spectra; these also include additional losses (e.g. bend loss and mode-mismatch loss) except for the waveguide scattering loss. The experimental normalized sensitivities and  $Q$  values for each fabricated device are plotted (white markers), with the waveguide dimensions noted in the legend.

sensitivity for highly confined modes (e.g., thick silicon waveguides [17] and disk resonators [28]), and a low  $Q$  / high sensitivity for weakly guided modes (e.g., thin silicon waveguides, TM polarized waveguides [54], and slot waveguides [55, 69]). The differences between the model (black markers) and the experimental results (white markers) are attributed to scattering losses and

the excess losses of the directional couplers (the couplers were assumed to be ideal in the model, i.e.,  $\kappa^2 + t^2 = 1$ ). Note that the difference between the experimental and modelling results is much larger for the narrow waveguides (500 nm) as compared to the wide waveguides (800-950 nm). It is known that wide waveguides have much lower optical scattering loss [66, 70, 71]. Scattering losses are usually induced by sidewall roughness. The interaction of the propagating mode with the sidewall roughness causes a strong scattering effect [66, 70, 72]. Thus, we expect that the scattering losses of the thin and wide waveguides (800-950 nm) should be relatively small and, hence, we expect good agreement between the model and experiments. It is seen that the experimental results for the 90 nm ultra-thin sensors agree very well with the model, both in terms of sensitivity and quality factor. These sensors offer performance that matches the theoretical limit for a critically coupled resonator.

## 3.5 Conclusion and Discussion

We have investigated, both by simulations and experiments, ultra-thin TE resonator sensors within the constraint of available thicknesses in standard MPW foundries and services. We obtained sensitivities over 100 nm/RIU with the ultra-thin TE resonator sensors. We have demonstrated, by experiment and simulation, the increased stability of these ultra-thin resonators, as compared to the traditional 220 nm thick resonators, in the presence

### 3.5. Conclusion and Discussion

---

of temperature variations. We report  $Q$  factors on the order of 15,000 to 25,000, with the ILODs on the order of  $5 \times 10^{-4}$  RIU. In addition, good agreement between experimental results and simulations was demonstrated. The bulk sensitivity and capability of these sensors in predicting glucose concentrations, in the presence of intentional 1 K temperature fluctuations, was demonstrated and showed a manifold improvement in these predictions as compared to traditional 220 nm thick resonator sensors. One method to quantify this improved performance, in the presence of temperature drift, is to compare their relative sensitivities (temperature sensitivity/bulk sensitivity). The calculated temperature-induced errors in the estimation of the change in refractive index of the cladding (due to 1K temperature change) are approximately 0.0015 and 0.0004 RIU/K, for the case of our conventional 220 nm thick resonator sensor and ultra-thin resonator sensor respectively. This means more than three times improvement in the performance (73% improvement).

The ultra-thin resonator sensors developed here, using the smallest available thickness offered by MPW foundries, can be integrated with the on-chip detectors also offered by these standard foundries. Furthermore, given that they are fabricated using SOI technology, they are well positioned to be integrated with CMOS electronics to produce a lab-on-chip. Additionally, as compared to conventional 220 nm resonator sensors, our ultra-thin resonator sensors, with larger evanescent fields, have unique advantages for bio sensing, e.g., by sampling more of the measurand, these sensors provide the capability

### 3.5. *Conclusion and Discussion*

---

to sense larger particles.

# Chapter 4

## Optimized Sensitivity <sup>4</sup>

Evanescent field sensors have shown promise for biological sensing applications. In particular, Silicon-on-Insulator (SOI)-nano-photonic based resonator sensors have many advantages, including exquisite sensitivity and compatibility with today's high volume CMOS foundries. We have investigated the optimum design parameters within the fabrication constraints of Multi-Project Wafer (MPW) foundries that result in highest sensitivity for a resonator sensor. We have demonstrated the optimum waveguide thickness to achieve the maximum bulk sensitivity with a SOI-based resonator sensor to be 165 nm using quasi-TM guided mode. The closest thickness offered by MPW foundry services is 150 nm. Therefore, resonators with 150 nm thick silicon core were fabricated and showed a sensitivity of 269 nm/RIU, whereas a similar resonator sensor with 220nm thickness showed sensitivity of around 200 nm/RIU.

---

<sup>4</sup>A version of this chapter will be published in:  
S. Talebi Fard, et al., "Optimized Sensitivity of Silicon-on-Insulator Strip Waveguide Resonator Sensor", In review (2015).

## 4.1 Introduction and Background

Researchers have investigated the optimum waveguide thicknesses for maximum sensitivities both analytically and experimentally for a waveguide slab [56] but not a waveguide resonator used for sensing which has different characteristics. It is known that the propagating TM-modes generally exhibit higher sensitivities due to an increased overlap of their evanescent field with the cladding [36, 54, 56]. Figure 4.1 shows the evanescent field penetrations depth of a propagating TM mode for the two waveguide thicknesses offered by MPW foundries (150 and 220 nm), based on equations 3.1. Comparing figures 4.1 and 3.1 show that the evanescent field penetration depth for quasi-TM waveguides with regular thickness of 220 nm is close and comparable to the penetration depth for TE guided mode in ultra-thin waveguides with 90 nm thickness.

The sensitivity can be defined in two ways: (1) bulk sensitivity and (2) surface sensitivity. For a waveguide, the homogenous or bulk sensitivity is defined as the sensitivity to the changes in the refractive index of the cladding, or aqueous solution surrounding the waveguide, assuming a homogenous solution ( $\frac{\delta n_{\text{eff}}}{\delta n_c}$ , for the case of waveguide's sensitivity, where  $n_{\text{eff}}$  is the effective index of the waveguide, and  $n_c$  is the refractive index of the cladding). The other type of sensitivity, commonly referred to as surface sensitivity, is defined as the sensitivity to the adsorbed bimolecular layer to the surface of the silicon core ( $\frac{\delta n_{\text{eff}}}{\delta t}$ , for the case of waveguide's sensitivity, where  $t$  denotes the

thickness of the adsorbed biomolecule). Both sensitivities were investigated for a simplified slab waveguide with silicon core on silicon dioxide substrate and aqueous cladding [56]. The results suggested a maximum bulk sensitivity ( $\frac{\delta n_{\text{eff}}}{\delta n_c}$ ) and surface sensitivity ( $\frac{\delta n_{\text{eff}}}{\delta t}$ ) at waveguide thicknesses of 190 nm and 210 nm respectively. The molecular add-layer used to determine the surface sensitivity was assumed to be a protein adlayer with refractive index of 1.48 [56, 73]. We have verified these optimum thicknesses as well using analytical methods (using analytical expressions by Yariv [74]) and fully-vectorial 2D eigenmode calculations. Note that the optimum value for surface sensitivity would be different depending on the distance of the newly adsorbed layer from surface of the waveguide core.

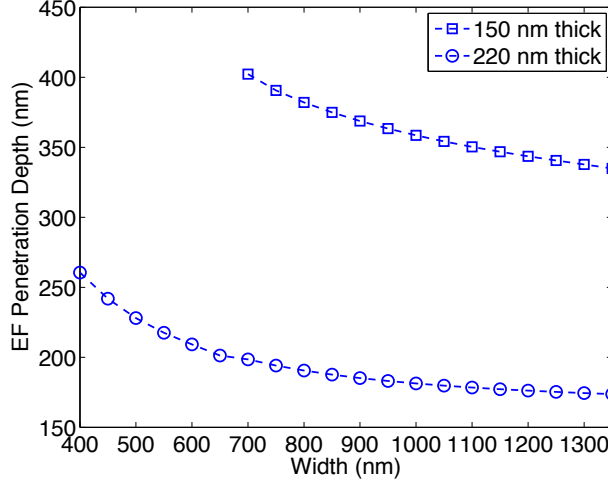


Figure 4.1: Simulated  $1/e$  penetration depths of the evanescent field of the first guided TM mode into the solution for various waveguide core thicknesses and widths.

In the case of resonators and interferometers, the sensitivity also depends

on the group index of the waveguide ( $n_g$ ). In this chapter, we have calculated and experimentally validated optimum thicknesses to achieve the highest sensitivities for a biosensing resonator, including the dispersion effect accounted by  $n_g$ . We fabricated TM resonators with the standard etch layer thicknesses offered by MPW foundries and verified experimental observations with theoretical simulations. Until now, the highest experimental sensitivity reported for quasi-TM ring resonators was 135 nm/RIU [54] but using the optimum waveguide thickness to maximize sensitivity, we demonstrate quasi-TM resonators with a bulk sensitivity of 270 nm/RIU.

## 4.2 Methods and Materials

Employing fully-vectorial 2D eigenmode (using Lumerical MODE Solutions.) calculations and analytical equations in MATLAB, we have determined our design parameters for a racetrack at, or close to, critical coupling [35, 44]. TM resonators with 150 nm thick silicon core, close to thickness with maximum sensitivity, and 220 nm thick resonators as a conventional reference for comparison purposes were fabricated at The Institute of Microelectronics (IME) foundry in Singapore [75].

Fabricated devices were characterized using a custom test platform developed by our lab to sequence solutions over the sensor [28, 34, 76]. For bulk sensitivity measurements, a set of NaCl refractive index (RI) titrations ranging from 62.5 mM to 1 M were subjected to the sensors to measure

their response. The chip was thermally tuned to 25 °C to limit the impact of thermal noise and drift on the measurements. For surface sensitivity measurements, standard sandwich assay involving well characterized molecules were used to demonstrate the sensors ability to detect biological interactions as described in [76]. Figure 4.11(a) is schematic representation of our Bio assay material.

### 4.3 Theory: Waveguide's Sensitivity

The homogenous sensitivity of a waveguide is defined as the change in effective index as a function of a change in refractive index of cladding (equation 4.1). We have calculated homogenous sensitivity (or bulk sensitivity) of a slab waveguide, with silicon as the core, silicon dioxide as the substrate, and aqueous cladding; using two methods: analytically (using analytical expressions by Yariv [74]); and with 1D MODE simulations. A matching results between these two methods were achieved (figure 4.2), verifying that our simulations results (markers in fig. 4.2) are accurately aligned with the analytical models (solid lines in fig. 4.2). These analysis results of waveguide's homogenous sensitivity for a slab waveguide suggest that a 190 nm (36 nm) thickness is optimal for TM (TE) bulk sensing, these values were also identified by other researchers [56].

$$\text{Waveguide bulk Sensitivity} = \frac{\delta n_{\text{eff}}}{\delta n_c} \quad (4.1)$$

### 4.3. Theory: Waveguide's Sensitivity

---

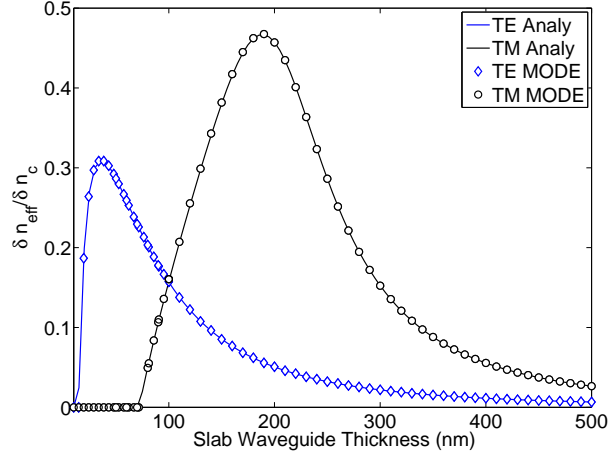


Figure 4.2: Sensitivities of the waveguide as functions of slab thicknesses. Solid lines show the results of analytical calculations and the markers show the results of 1D MODE calculations.

where  $n_{eff}$  is the effective index of the waveguide and  $n_c$  denotes the refractive index of the cladding.

The surface sensitivity of a waveguide is defined as a change in effective index of the waveguide, as the thickness of the molecular layer adsorbed to the surface of the silicon core changes (eq. 4.2). To investigate the surface sensitivity, we start with a slab waveguide using 1D MODE. We assumed the molecular add-layer to be a protein with refractive index of 1.48 [56, 73].

$$\text{Waveguide Surface Sensitivity} = \frac{\delta n_{eff}}{\delta t} \quad (4.2)$$

where  $t$  denotes the thickness of the adsorbed biomolecule. This is assuming that a homogenous layer is added evenly across the surface. Figure 4.3 shows the simulation results for slab waveguide surface sensitivity, as a function

#### 4.4. Resonator's Sensitivity - Effect of Dispersion

---

of slab thickness. These results suggest that a 210 nm (65 nm) thickness is optimal for TM (TE) surface sensing, these values were also identified by other researchers [56].

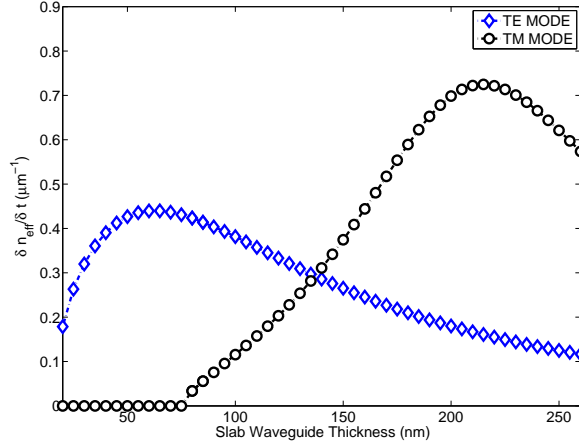


Figure 4.3: Surface Sensitivities of the waveguide as functions of slab thicknesses. A 10 nm thick molecular layer with refractive index of 1.48 is used.

## 4.4 Resonator's Sensitivity - Effect of Dispersion

For resonators, sensitivity is defined as the shift in resonant wavelength due to a refractive index change in the cladding, which results from a change in concentration of the analyte in cladding or from biomolecular adsorption to the surface of the silicon waveguide. To include the effect of this dispersion, the group index ( $n_g$ ) is used since it relates to the effective index of the

#### 4.4. Resonator's Sensitivity - Effect of Dispersion

---

waveguide ( $n_{\text{eff}}$ ) to changes in the resonant wavelength (equation 4.3) [44]:

$$n_g(\lambda) = n_{\text{eff}}(\lambda) - \lambda \frac{\delta n_{\text{eff}}}{\delta \lambda} \quad (4.3)$$

Simulations of various waveguide core thicknesses were used to calculate  $n_g$  and ultimately determine the resonator sensitivity ( $\frac{\delta n_{\text{eff}}}{\delta n_c}$ ). Using the simulations results and equation 4.3, values for  $n_g$  as functions of slab thicknesses is shown in fig. 4.4. It can be observed that group index ( $n_g$ ) of a TM propagating mode varies significantly as slab thicknesses vary between 100 nm to 300 nm (fig. 4.4).

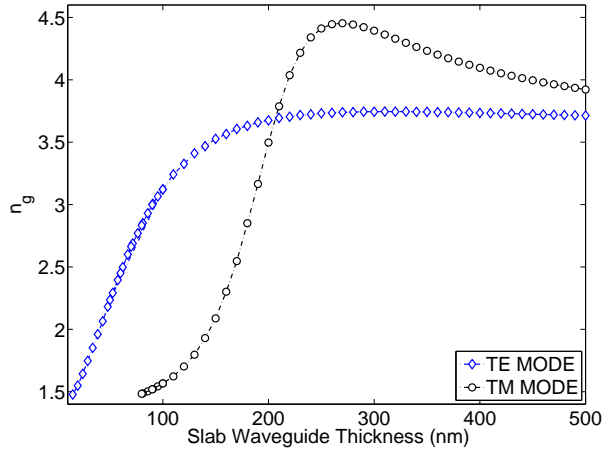


Figure 4.4: Group indices of slab waveguides as functions of slab thicknesses.

The next two sections discuss the fully-vectorial 2D eigenmode calculations (simulations) and compare them with the observed, experimental results for both kinds of sensitivities (bulk and surface) when considering the effect of dispersion (including  $n_g$ ).

## 4.5 Resonator's Bulk Sensitivity - Theory, Simulation and Experimental Results

The bulk sensitivity of a resonator is defined as the shift in resonant peak that is caused by a change in refractive index of cladding,  $\frac{\Delta\lambda_{res}}{\Delta n_c}$  (equation 4.4) [35].

$$\text{Resonator's Sensitivity} = S = \frac{\Delta\lambda_{res}}{\Delta n_c} = \frac{\lambda_{res}}{n_g} \frac{\delta n_{eff}}{\delta n_c} \quad (4.4)$$

where  $\lambda_{res}$  is the resonant wavelength of the resonator and  $n_g$  is the group index.

To calculate the sensitivity of the resonators for the case of a slab waveguide, equation 4.4 along with the above simulated  $n_g$  results and simulated waveguide sensitivities ( $\frac{\delta n_{eff}}{\delta n_c}$ ) are used (figure 4.5, dashed lines with hallowed markers). For these calculations, we have considered a perturbation of 0.01 RIU for the refractive index of the cladding, assuming that  $\frac{\delta n_{eff}}{\delta n_c}$  is nearly constant over small ranges. These results indicate that the maximum sensitivity for a quasi-TM mode happens when the silicon slab thickness is around 155 nm. Conditions for maximum sensitivity for a waveguide resonator and waveguide alone differ because of the effect of  $n_g$  in the sensitivity of the resonators. The optimal thickness, which happens to be close to one of the etch-depths offered through a standard MPW processes, provides an advantage for improved sensitivity of a biosensor at the economies of scale offered

#### 4.5. Resonator's Bulk Sensitivity

---

through mass fabrication.

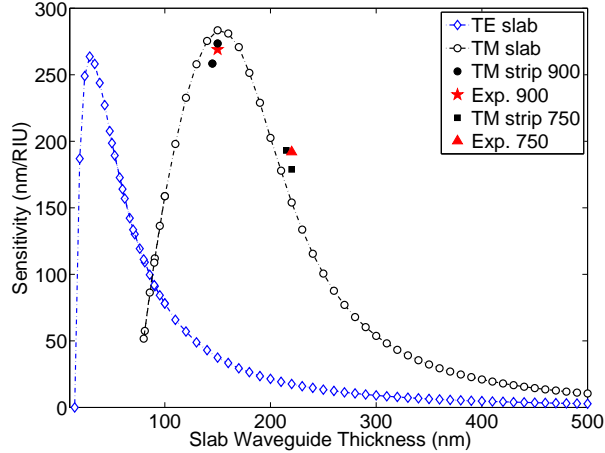


Figure 4.5: Calculated resonator's sensitivities, based on simulations, as functions of silicon core thicknesses. The hallowed markers are the simulated sensitivities for the case of a slab waveguide, the black filled markers are the simulated sensitivities for the case of rectangular waveguides with waveguide widths of 750 nm and 900 nm, and the red markers are averages of our experimental results for TM ring resonators with 150 and 220 nm thick silicon cores.

The bulk sensitivity of the fabricated resonator sensors were experimentally validated using refractive index standards described above. The slope of the best fit line through the different resonant wavelengths at each concentration results in its bulk sensitivity. Each sensor was measured several times on different days and the experimental observations were compared with simulation results in figures 4.5 and 4.7.

To better understand and compare the simulation results with the experimental observations, we included simulated sensitivities for rectangular waveguides and interpolated the experimental observations at those designed points (figure 4.5). The sensitivity for the waveguide is plotted for a wave-

#### 4.5. Resonator's Bulk Sensitivity

uide core thickness of 220 nm and width of 750 nm, as well as for waveguide thickness of 150 nm and width of 900 nm.

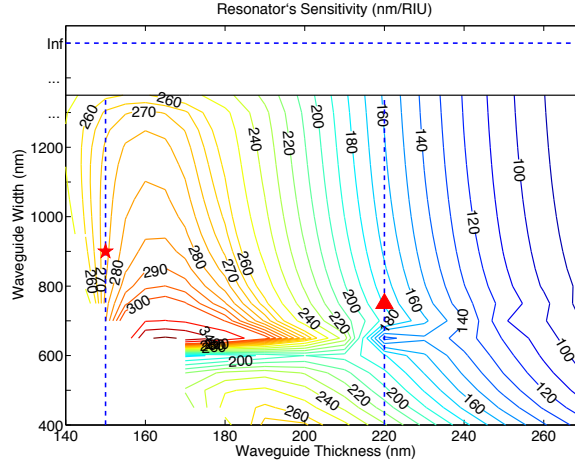


Figure 4.6: Contour plot of sensitivity in nm/RIU as functions of waveguide widths and thicknesses. The cross-section corresponding to the dashed line representing the slab is plotted in figure 4.5, and the other two cross-sections representing the thicknesses of 150 and 220 nm are plotted in figure 4.7. The red markers show the fabricated TM resonator devices (Star: Width = 900 nm and Thickness = 150 nm, Triangle: Width = 750 nm and Thickness = 220 nm )

To further improve our model, we simulated the sensitivity of a TM mode propagating in a rectangular waveguide as a function of waveguide width and thickness. These results are illustrated in figure 4.6 as contour plots. The simulation area was fixed to  $4 \times 4 \mu\text{m}$  and only structures with less than 2% error in their sensitivity (based on the error calculated in the convergence test) were considered. These results indicate that the maximum bulk sensitivity of 363 nm/RIU is achieved at a waveguide thickness of 165 nm. The closest thickness offered by MPW foundries to this optimum thickness is 150 nm.

#### 4.5. Resonator's Bulk Sensitivity

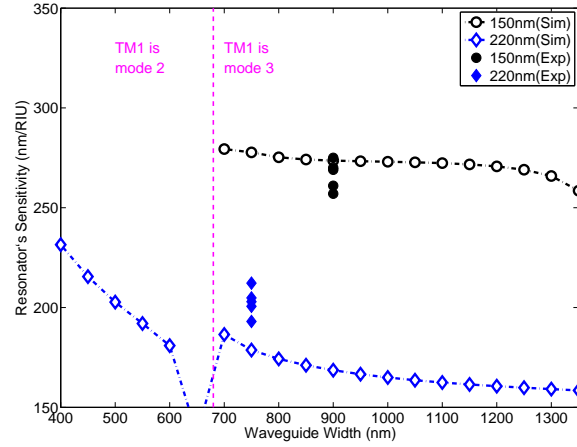


Figure 4.7: Sensitivities of TM waveguide resonators to the aqueous cladding for the optimum silicon core thickness of 150 nm and conventional thickness of 220 nm as functions of widths. The filled markers show corresponding experimental results.

The two vertical dashed lines in figure 4.6 represent the cross-sections for the thicknesses offered by MPW foundries (150 and 220 nm). The sensitivities for these two thicknesses, are plotted as functions of waveguide widths in figure 4.7, where hallowed markers indicate the simulations and filled markers indicate the experimental results. The slight variations, between the experimental and simulation results, partly come from the imprecision of salt-solutions (measurement error) and any thermal noise in tuning the stage, and can partly be explained with the non-uniformity that exist on SOI chips [77].

#### 4.6. Resonator's Temperature Sensitivity - Simulation Results

---

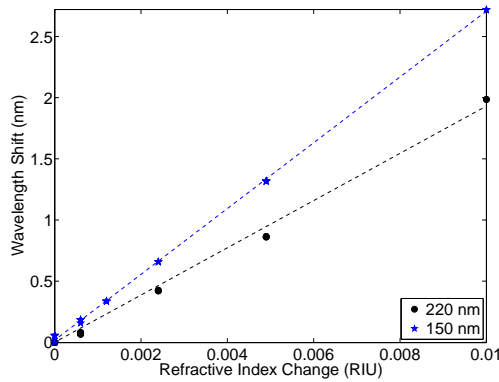


Figure 4.8: Measured resonant peak wavelength shift as indices of refraction of the cladding media changes. The slope of the line indicates the sensitivities (nm/RIU) for the optimum silicon core thickness of 150 nm and conventional thickness of 220 nm, to be 269 and 193 respectively.

#### 4.6 Resonator's Temperature Sensitivity - Simulation Results

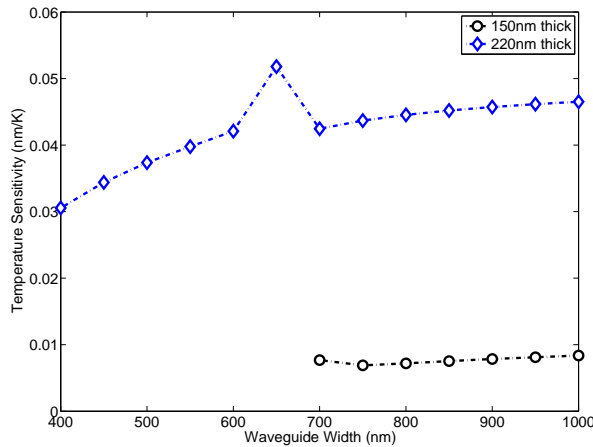


Figure 4.9: Temperature sensitivities of TM guided mode in a strip waveguide resonator sensor as functions of waveguide core widths, for the two waveguide core thicknesses of 150 nm and 220 nm.

Sensitivities of strip waveguide resonator sensors for TM guided modes were calculated as described in section 3.2.2. Figure 4.9 shows the results in these simulations/calculations for two silicon thickness of 150 nm and 220 nm.

## 4.7 Resonator's Surface Sensitivity - Simulations and Experiments

Surface sensitivity of a resonator is defined as the sensitivity to the adsorbed biomolecular layer to the surface of the silicon core. Therefore, waveguide's surface sensitivity is defined as  $\frac{\delta n_{\text{eff}}}{\delta t}$ , where  $t$  denotes the thickness of the adsorbed biomolecule. Subsequently, surface sensitivity of resonator is described as  $\frac{\delta \lambda}{\delta t}$ . The resonant wavelength shift as a function of the thickness of the add-layer is approximately linear for small add-layer thicknesses ( $< 30$  nm). We approximate the simulated surface sensitivity of our fabricated devices based on a 10 nm protein-like add-layer with refractive index of 1.48 [78]. Using our simulation/analytical model for slab waveguide, the maximum surface sensitivity of a TM resonator sensor is calculated to be at the thicknesses around 185 nm (figure 4.10). The surface sensitivity for TM resonator sensors with waveguide dimensions of 750x220 nm and 900x150 nm (our fabricated devices) are simulated to be 300, and 245 pm/nm, respectively.

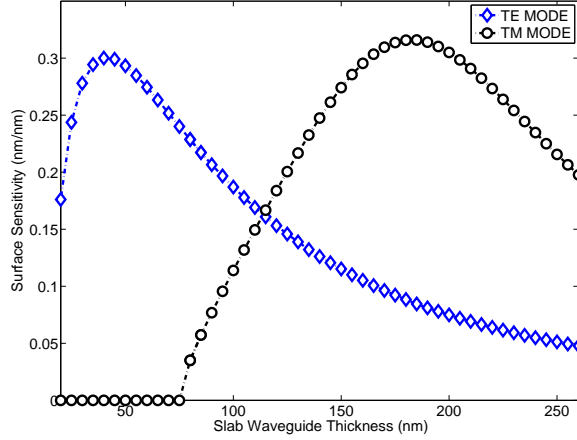


Figure 4.10: Calculated resonator’s surface sensitivities, based on simulations, as functions of silicon core thicknesses. The hallowed markers are the simulated sensitivities for the case of a slab waveguide.

## 4.8 Bio-Sensing Demonstration

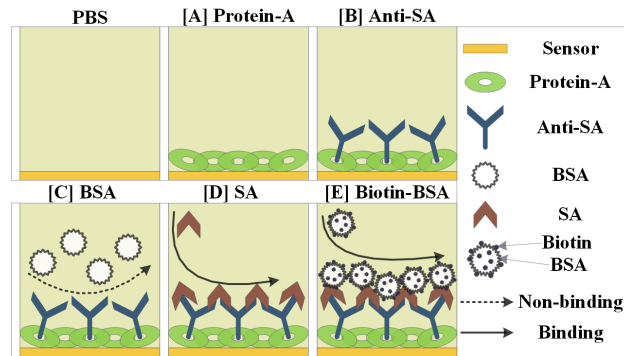
A sandwich assay representing a model biological system was performed to demonstrate the biosensing capability of our quasi-TM mode ring resonator’s and verify the surface sensitivity characterized using the electrostatic polymers. Figure 4.11(b) shows the result of the biological sandwich used demonstrate the sensors capability to detect molecular binding at its surface. The details of each reagent and step is described in detail in our previous manuscript [76] with the relevant highlights restated here. The introduction of each reagent was followed by a 20 minute rinse using PBS buffer to remove any unbound species in the channel (shown by the short, black dashed line in Figure 4.11(b)). After achieving a signal baseline in a PBS buffer at 37 degrees Celsius, Protein-A (1 mg/mL) was passively adsorbed to the sensors

native oxide surface prior to Region B to facilitate the immobilization and orientation of the capture antibodies [79, 80]. Region B shows the robust immobilization of the IgG capture antibody, anti-streptavidin ( $10 \mu\text{g}/\text{mL}$ ), to the Protein-A add-layer.

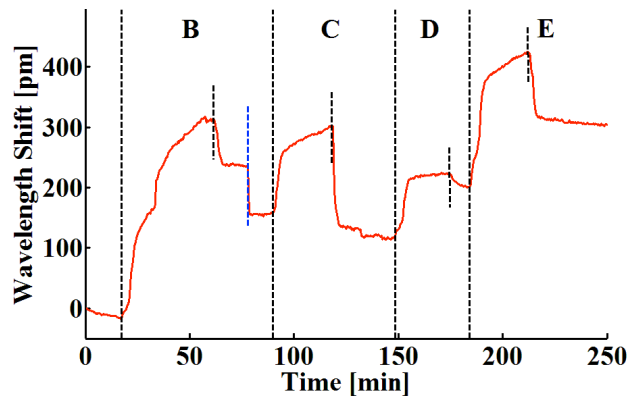
The unintended introduction of an air bubble mid-way through the antiSA rinse cycle (Region B), indicated by the blue-dashed vertical line, does not impact the viability of the subsequent biological species or their functionality. To show that subsequent molecular binding interactions are specific and to prevent unwanted, non-specific adsorption to the sensor, BSA ( $20 \mu\text{g}/\text{mL}$ ) was introduced next (Region C) to block any exposed surfaces remaining on the sensor (Region C). The slight negative shift in resonant wavelength after the BSA block and challenge (Region C) suggests that a small portion of the antibody add-layer lifts off but the original sensor coverage (Region B) was robust. Next, the functionalized and blocked sensor was subjected to  $10 \mu\text{g}/\text{mL}$  of SA, the model analyte captured by the antibody (Region D). The resulting shift in the sensors resonant wavelength after the buffer rinse suggests specific and irreversible binding interaction as expected. To further demonstrate the sensors capability to detect molecular binding, biotin conjugated with BSA was introduced as a final amplification step. Biotin and SA have one of the highest non-covalent binding interactions known [81] resulting in another, permanent resonant shift (Region E).

Protein A (with a diameter of approximately 3 nm [82, 83] and refractive index of 1.48 [78]) can approximately form a thin layer of 1-3 nm thick

#### 4.8. Bio-Sensing Demonstration



(a)



(b)

Figure 4.11: Surface Sensing Experiment [courtesy of UW team]. a) Schematic representation of the bio-assay material. b) Biosensing demonstration using a model biological system.

[28, 84]. Based on our simulated sensitivity values, a layer of 1 nm thick protein layer would have covered around 50% of our sensor's surface to result in the observed shift. Subsequently, if a 3 nm layer was formed, about 16% surface coverage results in the observed shift. These results are within the range of surface coverage that was determined by other researchers [84].

## 4.9 Discussion, Summary and Conclusion

We have investigated the optimum thickness of the waveguide core that results in the highest sensitivity for a strip waveguide resonator sensor, within the constraints of MPW foundries. The results indicate that guided quasi-TM modes have higher sensitivities to the changes in refractive indices of the cladding media, since larger evanescent field component is traveling above the waveguide, where the target molecules exist. This affects the term  $\frac{\delta n_{\text{eff}}}{\delta n_c}$  in the sensitivity relation and researchers have investigated the maximum sensitivity based on this term. However, for the case of the resonators,  $n_g$  also affects the sensitivity of the device (equation 4.4). Our investigations determined that the optimum thickness for TM resonator sensors is around 165 nm, which is close to one of the thicknesses offered by MPW foundries (150 nm). The compatibility of these resonators with the standard CMOS processes and MPW foundries, in terms of their minimum feature size requirements as well as offered thicknesses, make them a cost-effective candidate for a sensor.

The measured Q value, from the spectra of these resonators in water, are 10100 and 4500 for 220 nm thick and 150 nm thick resonator sensors respectively. These give intrinsic limit of detection (iLoD) of approximately  $7.5 \times 10^{-4}$  RIU and  $1.2 \times 10^{-3}$  RIU for 220 nm thick and 150 nm thick resonator sensors respectively. The extinction ratio for both these devices was measured to be around 30 dB. The lower Q value associated with 150

nm thickness, compared to the conventional 220 nm thick silicon core, is partly due to lower group index associated with this thickness, and partly due to higher intrinsic losses (bend loss, mode-mismatch loss, substrate leakage loss). Assuming that these resonators are close to critical coupling, their Q values translate to distributed losses of 34 dB/cm and 48 dB/cm for the resonators with 220 nm and 150 nm thick silicon core respectively. Based on simulations, material absorption losses, including water absorption, are responsible for approximately 23 dB/cm and 19 dB/cm of these losses for the resonators with 220 nm and 150 nm thick silicon core, respectively. The estimated losses based on the dry measurements of these devices are 14 dB/cm and 28 dB/cm for the resonators with 220 nm and 150 nm thick silicon core, respectively. These values approximately exclude the losses due to water absorption. As mentioned in chapter 3, the scattering losses are usually induced by the interaction of the propagating mode with the sidewall roughness [66, 70, 72]. Therefore, TM modes experience less scattering loss caused by sidewall roughness because the higher proportion of the guided mode is above and below the waveguide and, hence, the guided mode interacts less with the roughness in the sidewalls (resulted from fabrication). A propagation loss of  $\sim 3$  dB/cm for TE guided mode in a strip waveguide, dominated by sidewall scattering, is demonstrated experimentally and analytically [44, 66, 70, 72]. It has also been shown that thinner waveguides, fabricated in CMOS-compatible processes, exhibited lower scattering losses, in the order of 2 dB/cm [58]. Therefore, we estimate the scattering losses

for TM modes to be less than 3 dB/cm. The remaining losses ( $\sim 9$  dB/cm and 26 dB/cm for the resonators with 220 nm and 150 nm thick silicon core respectively) are contributed by bend losses (radiation loss, and mode mismatch loss), substrate leakage, and coupling loss. Propagation losses, including the scattering loss and substrate leakage, as well as bend losses can be improved by using wider waveguides. The loss due to substrate leakage can be improved using SOI wafers with thicker silicon oxide substrates (e.g. SOI wafers with 3  $\mu\text{m}$  thick silicon oxide substrate).

Simulations supported by experimental results in this chapter demonstrate a novel approach to achieve higher sensitivity within the constraints of MPW foundries, which has numerous advantages such as possibility of mass fabrication and integration with CMOS circuitry for potential system-on-chip implementations.

# Chapter 5

## Integrated Photodetector

### Sensors <sup>5</sup>

A resonance-enhanced, defect-mediated, ring resonator photodetector has been implemented as a single unit biosensor on a silicon-on-insulator platform, providing a cost effective means of integrating ring resonator sensors with photodetectors for lab-on-chip applications. This method overcomes the challenge of integrating hybrid photodetectors on the chip. The demonstrated responsivity of the photodetector-sensor was 90 mA/W. Devices were characterized using refractive index modified solutions and showed sensitivities of 30 nm/RIU.

#### 5.1 Introduction

Various types of silicon photonic resonators have been previously demonstrated with sensitivities sufficient for bio-molecule detection [17, 28, 30, 34,

---

<sup>5</sup>A version of this chapter have been published in [85]:  
S. Talebi Fard, et al., "Silicon-on-insulator sensors using integrated resonance-enhanced defect-mediated photodetectors." *Optics Express* 22, no. 23 (2014): 28517-28529.

35], however, these demonstrations did not use an integrated photodetector. Hybrid photodetectors have been demonstrated using III-V materials [86–88] or germanium [89–93] on the SOI platform. However, these detectors required the use of relatively complicated and expensive processes, which is not in keeping with the goal of providing an inexpensive lab-on-chip. To avoid the need for implementing such hybrid photodetectors, we suggest the use of defect-mediated based photodetectors on SOI [94–98]. In this chapter, we propose integrating such photodetectors [94–98] with well-developed and characterized resonator-based sensors [17, 28, 30, 34, 35]. To achieve this, we brought together the expertise of two groups, one at McMaster university, and one at the University of British Columbia (UBC), where the McMaster group’s expertise is in ion-implanted defect-mediated based photodetectors [94–98], and UBC’s expertise is in resonator-based sensors [17, 28, 30, 34, 35, 99].

Here, we investigate and demonstrate a ring resonator sensor with an integrated detector, which exploits the resonance enhancement of the ring for increased responsivity.

## 5.2 Resonator Sensors and Defect-Mediated Photodetectors

In this section, we review the performance and characterization of defect-mediated photodetectors, which have been characterized by Knights et al.

[94–98], as well as the resonator sensors developed in our group [17, 28, 30, 34, 35]. Further, we discuss the novel integration of these photodetectors with a resonator-based sensor.

### 5.2.1 Defect-Mediated Photodetectors

Silicon is a relatively poor material for photodetection in the near-infrared because the photon energy is less than the silicon bandgap resulting in negligible optical absorption. To overcome this, defect-mediated silicon waveguide detectors have been proposed and characterized [94–98, 100]. These photodetectors are formed by creating a *p-i-n* diode across a waveguide structure. An inert ion implantation into the intrinsic region causes damage to the silicon lattice which introduces deep levels in the bandgap through which light with energy less than that of the bandgap can be absorbed. The lattice damage-induced absorption, which increases the propagation loss to 20-100 dB/cm [96], causes the absorbed light to produce electron hole pairs that can be extracted by applying a reverse bias to the *p-i-n* diode. A subsequent low temperature anneal can be used to partially repair the damage to achieve an optimum defect concentration. The increased absorption due to the presence of the defects is modest, so, if a linear detector were to be used, it would have to be long in order to absorb a large fraction of the incident light and, thereby, achieve a high responsivity. Alternatively, the effective responsivity can be increased by using a resonant structure which makes use of the intensity buildup within the resonator to achieve increased absorption

within a small footprint [101]. In these resonant detectors, the increased optical loss associated with the defects reduces the quality factor and therefore introduces a tradeoff between the responsivity and the precision of sensing. Defect-mediated silicon photodetectors fabricated in this manner have shown responsivities of 0.5 to 10 A/W [100].

### 5.2.2 Evanescent Field-Based Resonator Sensors

Evanescent Field (EF) sensors operate by detecting a change in the effective refractive index of a waveguide [9, 32, 102, 103] caused by changes in the concentration of an analyte in the cladding (bulk sensing) or as molecules bind to a functionalized surface of the waveguide core (surface sensing). Optical resonators, having small footprints and longer interactions with the analytes in their cladding media (resulting in higher sensitivities), are promising candidates for sensing applications. SOI-based resonator sensors with small footprints, each integrated with a detector, would make high-throughput and/or simultaneous analysis of multiple analytes possible, where many sensors, each designed to measure a different target could be integrated on a single chip. These chips could be designed, with various sensors aligned, to use microfluidic channels to deliver various targets to the sensors, all in a single system. Various resonator sensors have been developed and characterized, some of which include disk resonators[28]; strip waveguide and slot waveguide ring resonators [17]; strip waveguide Bragg gratings [34]; and slot waveguide Bragg gratings [30]. These resonator sensors were shown to have

sensitivities and limits of detection approaching the theoretical maximum value (based on the case of a resonator in water). We have also characterized and validated these sensors using a standard ‘sandwich’ assay [34]. Having fabricated these sensors using a CMOS compatible SOI wafers, through a Multi-Project Wafer (MPW) foundry, provides the potential for integration of these sensors with on-chip electronics, and makes the integration of a complete system on a chip possible.

### 5.2.3 Defect-Mediated Photodetector Resonator

#### Sensor

We propose integrating defect-mediated photodetectors with previously demonstrated resonator-based biosensors, such as ring [35], disk [28], and phase-shifted Bragg grating resonators [30], to create a biosensor with integrated photodetectors (photodetector-sensor). Figure 5.1 shows schematic drawings of how defect mediated photodetectors could be integrated with each type of biosensor. A top view of each sensor shows the doped and detection regions. In each case the defect-mediated detector is introduced across the waveguide that forms the resonator cavity.

The 3D rendering below each schematic view provides perspective on how the defect region and detector can be oriented in a fluidic channel for biosensing applications. The biomolecules would be introduced across the entire device area but only those in proximity to the resonator waveguide

## 5.2. Resonator Sensors and Defect-Mediated Photodetectors

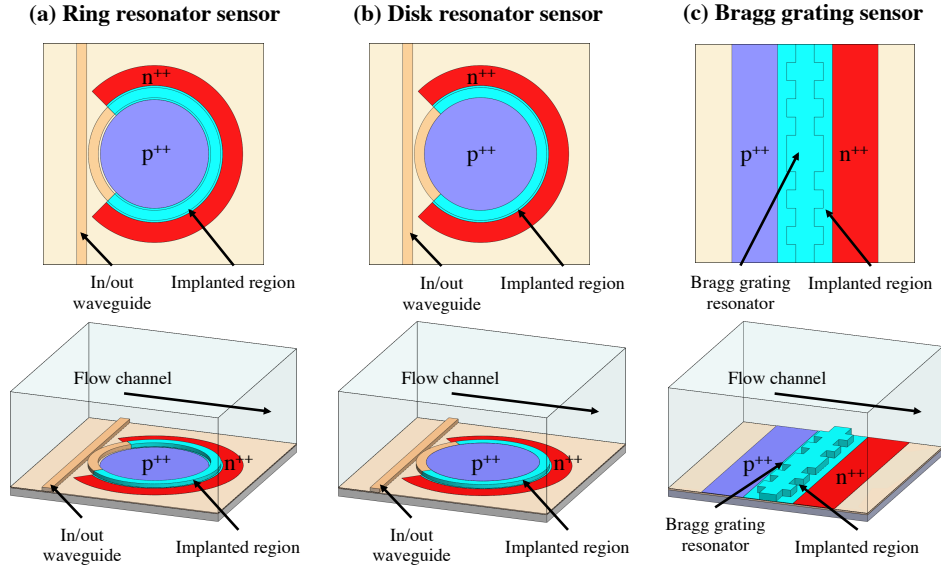


Figure 5.1: Schematic representations of proposed designs for biosensing: a) a defect-mediated ring resonator photodetector-sensor; b) a defect-mediated disk resonator photodetector-sensor; and c) a defect-mediated Bragg grating photodetector-sensor. The region of the detector with defects is highlighted in bold cyan. The remaining waveguide is shown in beige.

are interrogated. The ring resonator, Fig. 5.1(a), and disk resonator, Fig. 5.1(b), share similar configurations except that the disks are not etched in the center and only have one exterior side-wall. The ring, however, has two sidewalls formed at the inner and outer radius of the ring. The  $n^{++}$  implants are shown in red while the  $p^{++}$  implants are shown in blue. This forms a PIN structure, with the detection occurring in the “I” region which has defects.

The operation of each type of defect-mediated photodetector resonator sensor is very similar. The defect-mediated photodetector in the resonance cavity senses the optical power. Since the buildup of power inside the res-

onator is most significant at the resonance wavelength, by measuring the photocurrent as the wavelength is varied, one can find the wavelength for which the intensity buildup is maximum and determine the resonance wavelength. Furthermore, since each resonator forms an evanescent field-based sensor as described in Section 5.2.2 the resonance wavelength shifts as the refractive index of the cladding changes. Thus, in this configuration the resonator allows the device to sense refractive index changes while the integrated detector allows the simultaneous readout of the sensor response in one device.

### 5.3 Design Considerations and Layout

As a proof of concept, two variations of ring resonator photodetector sensors like that depicted in Fig. 5.1(a) were designed and fabricated. A cross-section of the detector is shown in Fig. 5.2. In order to integrate the photodetector with the ring resonator, rib waveguides, as opposed to strip waveguides, are used to allow for electrical contact with the junction to extract photocarriers that are generated in the waveguide. Metal contacts are made to the highly doped  $n^{++}$  and  $p^{++}$  slab regions far away from the optical mode that is confined to the waveguide such that the metal does not induce significant loss. The cladding oxide is removed above the resonator so that the analyte test solution can interact with the optical mode.

We fabricated two device variations (designs A and B) that have differ-

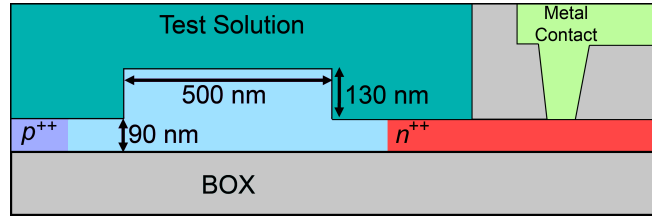


Figure 5.2: Schematic of detector cross-section

ent tradeoffs between sensitivity, responsivity, and quality factor. The two resonator designs are shown schematically along with microscopic images of fabricated devices in Fig. 5.3.

In design A, the oxide cladding is removed over 75% of the ring area to expose the ring to the analyte. Electrical contact from the metal routing to the ring interior is made through a contact via in the remaining oxide cladding as shown in Fig. 5.3(a). This design allows contact to be made to the center of the ring without introducing significant optical loss because the metal trace only crosses over the waveguides when it is above the cladding oxide, at the expense of a reduced sensitivity due to the smaller region over which the analyte interacts with the optical mode. In design B, the oxide cladding is removed over the entire ring, so the analyte can interact with the entire ring. In this case electrical contact to the silicon is made through a via outside the ring and contact is made to the ring interior by a conductive trace formed of highly doped silicon shown as the region of  $p^{++}$  doping crossing through the ring waveguide in Fig. 5.3(c). In this design a greater sensitivity can be achieved by allowing the optical mode to interact with the analyte

### 5.3. Design Considerations and Layout

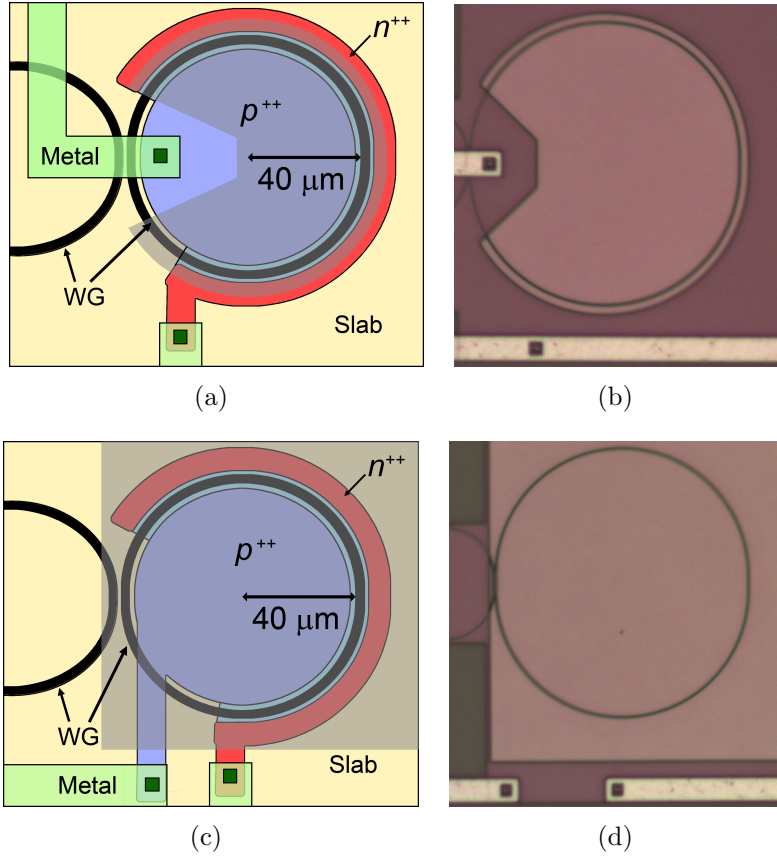


Figure 5.3: a) Schematic representation of design A (where the metal contact passes above the coupling region of the ring) ; b) Microscopic picture of design A; c) Schematic representation of design B (where the highly-doped silicon wire passes through the waveguide); d) Microscopic picture of design B. In Figs (a) and (c), the gray overlay indicates where the cladding oxide was removed.

over the entire length of the ring. This benefit comes at the cost of an increase of absorption loss and lower quality factor because the highly doped trace must cross the waveguide.

In both designs A and B the resonator is in a racetrack configuration with radius  $40\ \mu\text{m}$  and coupling lengths are  $4.2\ \mu\text{m}$  and  $5.1\ \mu\text{m}$ , respectively, each

with a 200 nm coupling gap. The racetracks were designed for critical coupling using Lumerical MODE Solutions and analytical models in MATLAB. The bend and mode-mismatch losses were simulated using MODE, and propagation loss was assumed to be around 3 dB/cm [44]. The induced loss due to implanted defects and proximity of highly doped regions were estimated to be around 10 dB/cm to 30 dB/cm [104, 105]. A few coupling lengths were calculated based on these assumed values of losses (where the assumed loss due to defects were varied from 10 to 30 dB/cm). For design A, a coupling length of 4.2  $\mu\text{m}$ , corresponding to the assumed average loss of 20 dB/cm due to defects, resulted in a spectrum close to critical coupling. In this design, 75% of the resonator is implanted. For design B, a coupling length of 5.1  $\mu\text{m}$ , corresponding to the assumed loss of 30 dB/cm, resulted in a spectrum close to critical coupling. In this design, the entire ring is implanted, and in addition a trace of  $p^{++}$  doping crosses the waveguide and therefore higher losses are expected compared to design A. The bus and resonator waveguides are 500 nm wide rib waveguides, formed by a 130 nm thick waveguide on a 90 nm thick slab. As shown in Figs. 5.2 and 5.3, the  $p^{++}$  and  $n^{++}$  doping regions are 500 nm from the edges of the waveguides. We choose the distance from the waveguide to the  $p^{++}$  and  $n^{++}$  contact regions based on two considerations: the doped regions must be sufficiently close to the waveguide to extract the generated carriers efficiently before they undergo carrier recombination, and the distance must be large enough so that the optical loss from the interaction with the highly doped regions is not too high.

## 5.4 Experimental Methods and Materials

The devices were fabricated at The Institute of Microelectronics in Singapore, up to the point at which the ion implantation was performed to introduce defects in the waveguide. For this step, implantation was performed at McMaster University. Boron ions were implanted at an energy of 30 keV and dose of  $5 \times 10^{12} \text{ cm}^{-2}$ . No post-implantation high temperature anneal was performed such that the boron remained inactive and thus only structural defects were introduced to the waveguide (i.e. no chemical doping took place). On-chip grating couplers (GCs) facilitate the efficient coupling of light into and out of the SOI chip [68], and electrical contact to the detectors is made by routing metal traces to the device from large on-chip contact pads that can be externally probed. This sensor was characterized using the techniques and reagents described in this section.

### 5.4.1 Experimental Setup

Our measurement setup used: a tunable laser (Agilent 81682A, Agilent Technologies, Inc., USA) with a wavelength range of 1460 nm to 1580 nm as the optical source; an optical power sensor (Agilent 81635A, Agilent Technologies, Inc., USA) to measure the output light intensity; and a source measurement unit (Keithley 2602, Keithley Instruments, USA) to perform the electrical characterization. Light was coupled into and out of the chip using GCs and an array of polarization maintaining (PM) optical fibers (PLC Con-

nections, LLC., USA). The PM fiber array was aligned to the GCs on the chip using a motorized stage that was controlled using an automatic alignment routine, to obtain maximum optical coupling to the devices. Electrical contact to the detectors was made by routing metal traces to the device from large on-chip contact pads that were externally probed, using a needle.

#### **5.4.2 Reagents and Microfluidic Setup**

To determine the bulk sensitivity, and to characterize the performance of our photodetector-sensors, standard aqueous solutions of sodium chloride (with concentrations of 0, 500 mM, 1 M, and 2 M) were characterized using a Reichert AR200 Digital Refractometer (Depew, NY). Polydimethylsiloxane (PDMS) microfluidic channels, with widths and heights of 200  $\mu\text{m}$  and 80  $\mu\text{m}$ , respectively, were aligned to the sensors and reversibly bonded on the chip to facilitate the delivery of standard solutions to the cladding media of our photodetector-sensors. Prior to bonding the PDMS to the chip, inlet and outlet holes for microfluidic channels were punched in the PDMS using a 0.5 mm coring tool (Schmidt Press, CORP, USA). After bonding the PDMS to the chip, the channels were linked to tygon micro-bore tubing using 21 gauge blunt needles (Nordson EFD, CORP., USA) through the punched inlet and outlet holes. These tubes were used as the fluidic inlet and outlets and were connected to a syringe. To maintain a constant flow rate of the reagents over our photodetector-sensor, a syringe pump (KDS-230, KD Scientific, Inc., USA) was set to operate in withdraw mode (negative pressure) at a constant

rate of 19  $\mu\text{L}/\text{min}$ .

## 5.5 Performance Analysis and Results

Prior to device characterization, the detectors were forward biased to produce a forward current of 1 mA for 5 minutes [106]. The current-voltage measurement for both designs is plotted in Fig. 5.4. The implanted photodetector-sensors were first tested under various reverse bias voltage (-2 to -35 V) conditions to determine a suitable operation point. In order to achieve a reasonable signal-to-noise (SNR), without unduly stressing the device, we chose a bias voltage of -10 V for operation.

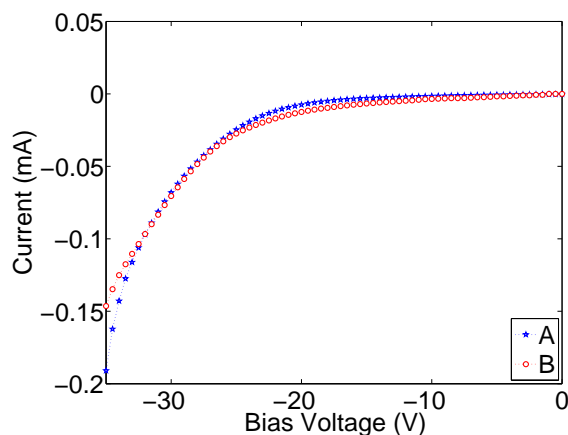


Figure 5.4: IV curves for designs A and B.

To further characterize the devices, we measured both the optical and the electrical responses of our photodetector-sensors; to do this we swept the laser's wavelength while simultaneously measuring the optical power trans-

### 5.5. Performance Analysis and Results

---

mitted through the ring and the current generated by the integrated detector (with a bias of -10 V). The optical power at the output of the laser was 0 dBm. There are various losses that contribute to the overall loss in the system. The primary dominant loss is associated with coupling from the fibers to the waveguides through the grating couplers. There are long ( $> 5$  mm) routing waveguides from the input GC to the device and from device to the output GC which also contribute to the loss. However, due to the symmetry of the design, the loss from the output of the optical power to the device is equal to the loss from device to the detector connected to the output fiber. Therefore, the total loss is divided by two to approximate the power level of the optical signal that reaches the device. Figure 5.5 shows the measured electrical and optical response of design A and design B devices. It can be seen that when the ring is on resonance there is an increase in the photocurrent due to the resonant buildup of energy in the ring.

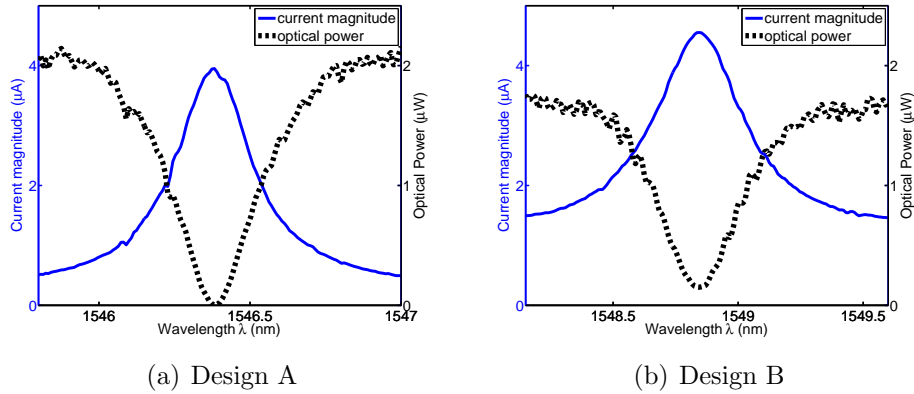


Figure 5.5: Measured electrical and optical responses of our implanted detector resonator sensors: a) Design A, and b) Design B.

### 5.5. Performance Analysis and Results

---

To estimate the responsivity of a device, the losses in the path from the laser output to the input of the device and from the device output to the detector were assumed to be equal, due to the symmetry of the design, giving an estimate of the power seen at the ring which was 0.045 mW and 0.04 mW and a calculated responsivity of approximately 0.09 A/W and 0.11 A/W for design A and design B, respectively. To calculate the dark current of a single device, the neighbouring devices had to be taken into account, since, to save space on the chip, several resonator sensors were designed to be wired together and to share common electrodes. This had the drawback that the dark current from the detectors wired in parallel was summed and the contribution from a single detector could not be directly measured. To estimate the dark current of only the detector under test, the dark current per unit length of each detector was assumed to be equal and the measured current was scaled by the ratio of the length of the detector under test to the combined lengths of all of the detectors that were in parallel. For the devices reported on here, the measured dark current calculated in this manner was 17 nA for the design A device and 30 nA for the design B device. The corresponding Noise Equivalent Power (NEP) for these two designs are 0.19  $\mu$ W and 0.27  $\mu$ W. Considering that the peak currents for designs A and B devices were 4  $\mu$ A and 4.5  $\mu$ A, respectively, the highest SNRs that were achieved were 235 and 160, respectively. Table 5.1 summarizes the characterization results. The relatively low quality factors ( $Q$ 's) for these photodetector-sensors, as compared to ring resonators without integrated detectors, is due to the loss

### 5.5. Performance Analysis and Results

---

Table 5.1: Summary of the performances of designs A and B devices

	Dark Current (nA)	NEP (1 $\mu$ W)	SNR	Responsivity (A/W)	Q
Design A	17	0.19	235	0.09	5800
Design B	30	0.27	160	0.11	4500

introduced by the ion-implantation in the silicon waveguides. As expected, design B has a lower  $Q$  than design A due to the loss associated with the highly doped silicon trace crossing the waveguide. Subsequently, for the purposes of this project, we proceed with the sensitivity analysis and experiments on the design A device only.

In order to characterize the sensitivity of the photodetector-sensor, the optical and electrical responses were measured simultaneously while the resonator was exposed to various salt solution concentrations. From the optical responses of the ring resonator in water, the  $Q$  for the design A device was measured to be approximately 4400; and the extinction ratio was measured to be approximately 30 dB. The measurements were repeated several times for each concentration. The location of the resonant peak is the important information for sensitivity measurements, which can also be found by curve fitting the response spectra. Figure 5.6(a) shows how the normalized electrical response shifts as a function of wavelength as we change the concentration of the solution. As we can see, the changing concentration of the

### 5.5. Performance Analysis and Results

---

reagent results in a resonance wavelength shift of the ring resonator. Figure 5.6(b) shows the resonance wavelength shift plotted against the salt solution's change in refractive index for various concentrations; the slope of the linear best fit gives a sensitivity (S) of approximately 30 nm/RIU. Based on measured values of Q and S, the intrinsic limit-of-detection (iLoD) for this sensor is  $1.1 \times 10^{-2}$  RIU. Considering that 75% of the ring is exposed to the solution, and that the simulated sensitivity for this waveguide is 40 nm/RIU, this yields a predicted sensitivity of 30 nm/RIU, in agreement with our experiments.

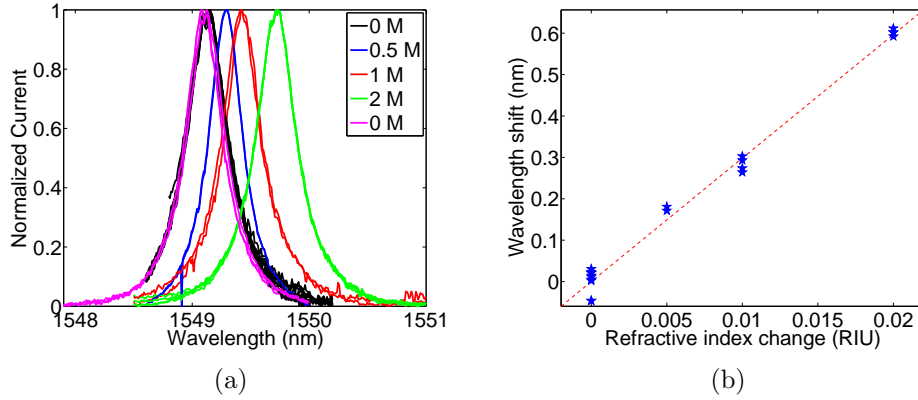


Figure 5.6: a) Normalized electrical response of photodetector-sensor design A when exposed to various salt solution concentrations. b) Resonant wavelength shift as a function of the change in refractive index of the solution, for design A. The slope of the best fit line, defined as the sensitivity, is approximately 30 nm/RIU.

## 5.6 Analysis and Discussion

In this chapter, we have investigated and demonstrated the integration of a resonator sensor and detector into one device. If, instead, the resonance-enhanced defect-mediated photodetector and the resonator sensor were designed as two separated, cascaded devices, then, the resonant wavelengths of the two would need to be matched and therefore, a wavelength locking mechanism would be required. However, having them as a single photodetector-sensor overcomes this wavelength mismatch issue and thus reduces the complexity of making measurements.

### 5.6.1 Performance Tradeoffs

The various advantages of using this novel approach for easier and cost-effective realization of a system on chip come with tradeoff that some of the sensing performance is sacrificed. Researchers developing defect-mediated photodetectors have investigated the optimum defect concentration ( $N_t = 2 \times 10^{17}$  to  $2 \times 10^{18}$  cm<sup>-3</sup>), and consequently the optimum ion implantation dosage, for maximum efficiency and detector responsivity in various structures [98, 104, 105]. Although these defect-mediated detectors have been shown to have performances well comparable with and sometimes better than Ge detectors [106], the integration of the detector into the sensor reduces the  $Q$  factor of the resonator (by contributing extra loss on the order of 20 to 30 dB/cm depending on the defect concentration [104–106])

which, in turn, degrades the performance of the sensor. We can quantify this reduction in performance by comparing the performance of our integrated photodetector-sensor to a hypothetical device fabricated using the same fabrication process without having an integrated detector. If we were to design this sensor without an integrated detector, we could have designed the resonator to have 100% of its surface exposed to the solution, which would increase the sensor's sensitivity to 40 nm/RIU. In addition, the introduction of defects in the waveguide degraded the  $Q$  by about 1000 on average (observed experimentally and confirmed through calculations). Therefore without the defects, the  $Q$  would be about about 5400 which would increase the iLoD from  $1.1 \times 10^{-2}$  (for the integrated detector) to  $0.7 \times 10^{-2}$  RIU. In exchange for this slightly lowered performance, the integrated device offers a host of advantages including reduced system footprint and less expensive fabrication process; furthermore, the iLoD of the integrated device could potentially be improved by optimizing the device geometries.

### 5.6.2 Discussion and Analysis of Device Performance for Sensing Applications

Integrated photodetector-sensors, like the one presented here, can be useful for many sensing applications, including the detection of aqueous solutions of changing concentration, gas mixtures, or molecules adsorbed to the surface of the sensor. We have previously studied the SOI-based resonator sensors and

have demonstrated both their bulk refractive index sensitivity and surface biosensing capabilities through experiments and simulations [17, 28, 34, 35, 76].

For applications which require detecting the concentration of specific molecules in the solution, a change in concentration results in a change in refractive index of the solution. In this application, the sensor's sensitivity to the concentration of specific molecules can be calculated from the sensor's bulk refractive index. For example, the relationship between glucose concentration and RI unit change is described as  $\Delta n_{glucose}(\lambda) = 2.7 \times 10^{-5} \Delta C_{glucose}[mM]$  [35, 46]. This translates to a sensitivity of approximately 810 pm/M for a device with sensitivity of 30 nm/RIU. Using the same method, the sensitivity for other aqueous solutions and gas mixtures can also be determined.

We have previously demonstrated the capability of our SOI-based resonator sensors in responding to the adsorbed molecular layers using standard sandwich assays [28, 34, 76]. The experimental results from these previous demonstrations agree with the simulations. In addition, we have confirmed that sensors offering impressive bulk refractive index sensitivities and iLoDs have also performed well in the surface sensing experiments. In the integrated device, we have observed a sensitivity of 30 nm/RIU which is 75% of the simulated value of 40 nm/RIU. Considering that only 75% of the resonator is exposed to the solutions, this shows that our device's performance agrees with simulations. Based on the agreement between previous experiments

and simulations, we expect that we can reliably predict the performance of devices in other applications such as biosensing. For example, if there is a bimolecular add-layer, with refractive index of 1.48 (to mimic proteins), the sensitivity of the non-integrated device (with full surface exposed) to the add-layer thickness is 0.12 nm/nm based on simulations. This sensitivity relation is approximately linear for small add-layer thicknesses of 0 to 30 nm. However, since 75% of the resonator is exposed in the integrated case, we expect a sensitivity of about 90 pm/nm to the thickness of add-layer with refractive index of 1.48.

The integrated device offers many advantages for potential system on chip applications as well as CMOS integration with a small footprint and less expensive mass fabrication process; these advantages might outweigh the sacrificed performance for many applications (particularly low-cost applications or those requiring disposable chips). In addition, the sensing performance of the device could be improved by optimizing the geometries and/or using TM polarization that can potentially provide higher sensitivity [56, 103].

## 5.7 Summary and Conclusion

To avoid using expensive hybrid fabrication of photodetectors for resonator biosensors and system integration on SOI, e.g., using III-V materials or germanium, we proposed the use of a defect-mediated photodetector-sensor. The absorption of the photodetectors were enhanced using resonant struc-

## 5.7. Summary and Conclusion

---

tures, giving improved responsivity and SNR, compared to a linear detector. Resonant structures were also shown to be promising biosensors. In this paper, we proposed and demonstrated a novel approach to integrate a sensor with a photodetector by integrating, as a single device, our well-developed resonator-based sensors with defect-mediated photodetectors.

The single-device integration of a photodetector-sensor was investigated by implementing two designs. In each design, the photodetector-sensor could interact with the target analyte through a window in its oxide cladding, where the cladding otherwise provides isolation for the electrical contacts made with the photodetector. In one of these designs, metal routing had to pass over the coupling region, resulting in only a portion of the total length of the photodetector-sensor being exposed to the analyte; whereas in the other design, highly doped silicon was used to route the electrical signal, allowing the full length of photodetector-sensor to be exposed. In the second design, in order to make contact to the inside of the ring, a portion of the highly doped silicon had to pass through the resonator waveguide. This resulted in additional loss in the resonator, and, therefore, a relatively lower  $Q$  for the second design. Hence, we performed sensitivity analysis on the design with the higher  $Q$ . Our photodetector-sensor had a measured responsivity of 0.09 A/W, sensitivity of 30 nm/RIU, quality factor of 4400 (in water), and extinction ratio of 30 dB.

The integration of a sensor with a photodetector removes the need for an external photodetector to interrogate the sensor and provides a significant

step toward the development of CMOS compatible, SOI-based systems on a chip. Implementing a defect-mediated photodetector in a resonator-based sensor (photodetector-sensor) allows for reductions in the device footprint, optical loss, complexity, and cost.

There are two factors to consider when choosing the defect concentration for a detector-sensor: 1) a defect concentration that is too high reduces the Q and iLoD (assuming constant S), thus, degrading the sensor's performance [17, 34]. 2) a defect concentration that is too low degrades the detector's performance by reducing the responsivity and SNR of the detector [105], while there is an optimal point for implant concentration and detector's performance [105]. These opposing trends impact the overall system's performance.

In this chapter, we demonstrated a basic proof of concept for an integrated ion-implanted photodetector-sensor. Clearly, we can improve these photodetector sensors based on concepts discussed in the previous chapters. For example, the lower sensitivity resulting from the TE guided mode in the rib structure can be improved by operating using the TM mode. Simulations show six times improvements in sensitivity when using propagating TM mode in rib waveguides.

# Chapter 6

## Differential Sensing System

Evanescent Field (EF) optical sensors have been widely investigated and used as biological and chemical sensors by researchers. However, the stability, repeatability, and accuracy of these sensors have always been a concern. These sensors, like all other optical devices, are affected by noises from various components/instruments in the experimental setup and the device's imperfections. In addition, the response of these sensors is significantly affected by common and inevitable environmental variations. In the experimental setup, the noise or error due to instrumentation (laser source and detector) can be classified to 1) amplitude intensity noise and 2) wavelength noise. The noise in the amplitude of the intensity are usually due to photodetector noises (shot noise, etc), and output power variations of the light source (tunable laser) [107–109]. The effect of amplitude noise for the resonators with high extinction ratio ( $>15\text{dB}$ ) is insignificant and can be further reduced to a more negligible value using fitting methods (e.g. lorentzian fit) [42, 107]. The wavelength noise in the instrumentation of the setup is mostly due to light source's wavelength repeatability, stability, and accuracy. For the case of our light source, the tuneable laser, the worst case of these noises

is  $\sim \pm 1\text{pm}$  for repeatability and stability [110].

Various groups have investigated the sources of noise in resonator sensors and temperature has been determined to have the most dominant and significant affect [107, 109, 111–113]. The resonant wavelength of the EF resonator sensors is strongly affected by temperature variations ( $\sim 80\text{ pm/K}$  for standard 220nm SOI sensor).

EF optical sensors can have a more stable performance in the presence of a reliable reference sensor that can capture and correct for dominant environmental variations such as temperature changes. To address the challenges of current EF sensors, a system of partially orthogonal sensors with various sensitivities is proposed and investigated. This system mimics a multivariate system. The aim of this design is to correct for correlated errors and drifts due to environmental variations.

## 6.1 Introduction

Evanescent field optical sensors based on Silicon-on-Insulator (SOI) have shown promises for biosensing applications [17, 34], ranging from basic medical research to home healthcare. These sensors provide label-free detection and estimation of concentration, presence of a molecule, or a molecular binding event. Fabricated devices seem to be remarkably affected by process variations such as those caused by environmental and external conditions. Among fabricated sensors, we have observed a lot of variability, from excel-

lent performance to unpredictable or poor response. From a system's point of view, the variability could strongly reduce the usage of these sensors because of poor repeatability. It also decreases the high throughput that is always associated with microelectronics and SOI-based integrated systems, fabricated through commercially available foundry services.

Data processing and chemometrics can improve the system's performance [114, 115], but a well-inclusive reference is required to be able to remove as much correlated and orthogonal noises as possible. (Orthogonal noise means that the undesirable variations are independent of the variation of interest. Correlated noise means that the variations affect the properties that are measured to predict/calculate the change of interest.) One of the major challenges of most sensing systems (e.g. bio-sensors) is to find a proper reference signal that accounts for most of the variations that are not relevant to the variations of the analyte of interest.

Researchers have proposed and tried various methods of having a reference sensor. Methods include having identical sensors but covering the reference sensor with a cladding material such as  $SiO_2$  or PMMA. Therefore, it does not come into contact with the analyte under study and only picks up the temperature variations [54]. However, a reference sensor under a material with different thermal properties might not reflect the temperature variations accurately and timely. In fact, it has been observed that drifts are hypothesized to be due to leakage of fluid into the cladding of the covered reference sensor [54]. This can also mean a change in thermal prop-

erties of the material and the system relations. The other common method of implementing a reference signal is having a reference sensor in another fluidic channel which does not experience the analyte changes [116]. This method is sometimes used as sensing reference and, other times, as biological reference or control experiment. The difference between the sensing signal (from analyte channel) and reference signal (from buffer solution) determines the corrected sensing signal. This method assumes that the buffer solution in the reference channel experiences the same variations as the analyte in the sensing channel. Using this method as sensing or temperature reference might not be the most ideal as the two sensors can be far away. Thus, it is difficult to make sure that the temperature of solutions in both channels are the same. This method might require advanced temperature control. Having a separate channel for biological control experiments is a common practice. This control channel can also benefit from a reference temperature sensor to correct for the possible variations between the temperatures of the solutions in two channels.

In this chapter, we propose and investigate a system model capable of correcting the common external and correlated drifts and noises (i.e. temperature variations). This method can be beneficial and applicable to any sensing application, including biological applications.

## 6.2 System Design and Methods

A system with a single resonator would respond to both cladding changes (including the change of interest) and changes in other components and properties of the system (noise in the system). Changes in optical properties of the waveguide due to environmental variations such as temperature and common mode shifts due to the source or detector, are examples of system noises. The error bars due to noises (unwanted variations and drifts) in our system are correlated and dominated by common mode contributions from each sensor. Sensors with various and significantly different sensitivities to cladding medium and to other contributing variations (e.g. temperature) in one channel would allow the rejection of these common mode variations.

Therefore, to address the challenges of bio-sensor systems, we propose a combination of multiple sensors with significantly different sensitivities in the same channels; i.e. both data channel (i.e. on the same waveguide bus) and fluidic channel. In such a design, all sensors in a single channel capture both the unwanted variations that causes drifts, such as temperature, and variations of interest, such as concentrations. Each sensor's response to these variations differ based on their specific sensitivity to that variation ( $\mathbf{S}$ ). As a result, solving for the variation of interest in the system of equations (i.e. a weighted difference between the resonant peaks of these sensors) would correct a dominant part of the common/correlated noises. Thus, a more accurate and direct indication of the variations of interest in the analyte

will be obtained. This can be achieved with any set of sensors that can be cascaded and have significantly different sensitivities to their surrounding changes.

We present the general case of our system proposal with the  $n$  dimensional matrix representation below:

$$\Delta\lambda = \mathbf{S} \Delta\mathbf{Var} \quad (6.1)$$

$$\begin{bmatrix} \Delta\lambda_{S1} \\ \Delta\lambda_{S2} \\ \vdots \\ \Delta\lambda_{Sn} \end{bmatrix} = \begin{bmatrix} \mathbf{S1} \\ \mathbf{S2} \\ \vdots \\ \mathbf{Sn} \end{bmatrix} \begin{bmatrix} \Delta\mathit{Var}_x \\ \Delta\mathit{Var}_2 \\ \vdots \\ \Delta\mathit{Var}_n \end{bmatrix} \quad (6.2)$$

$$\begin{bmatrix} \Delta\lambda_{S1} \\ \Delta\lambda_{S2} \\ \vdots \\ \Delta\lambda_{Sn} \end{bmatrix} = \begin{bmatrix} (\frac{\delta\lambda}{\delta\mathit{Var}_1})_{S1} & \cdots & (\frac{\delta\lambda}{\delta\mathit{Var}_n})_{S1} \\ (\frac{\delta\lambda}{\delta\mathit{Var}_1})_{S2} & \cdots & (\frac{\delta\lambda}{\delta\mathit{Var}_n})_{S2} \\ \vdots & \cdots & \vdots \\ (\frac{\delta\lambda}{\delta\mathit{Var}_1})_{Sn} & \cdots & (\frac{\delta\lambda}{\delta\mathit{Var}_n})_{Sn} \end{bmatrix} \begin{bmatrix} \Delta\mathit{Var}_x \\ \Delta\mathit{Var}_2 \\ \vdots \\ \Delta\mathit{Var}_n \end{bmatrix} \quad (6.3)$$

$$(\frac{\delta\lambda}{\delta\mathit{Var}_i})_{Si} \gg (\frac{\delta\lambda}{\delta\mathit{Var}_i})_{Sj} \quad \text{for } i \neq j$$

where  $\mathit{Var}_1$  to  $\mathit{Var}_n$  are the  $n$  varying properties of the system.  $\mathit{Var}_1$  includes, and dominated by, the variable of interest ( $\mathit{Var}_x$ ), but it is also affected by all other variable properties. This represents a multivariate system for sensing applications, where a higher degree of orthogonality between signals is desirable. The determinant of the matrix determines the degree of the orthogonality between its row vectors. Therefore, a system that has an

**S** matrix with larger determinant (which means that the sensitivity characteristics of the sensors have higher degrees of partial orthogonality) is more desirable.

For the case of a sensing system, the purpose is to measure the change of interest in the cladding medium as a result of changes in concentrations or biomolecular/chemical reactions. For each of the evanescent field sensors in the system, the peak resonance wavelength shifts according to equation 6.4:

$$\Delta\lambda_{Si} = \left(\frac{\delta\lambda}{\delta T}\right)_{Si} \Delta T + \left(\frac{\delta\lambda}{\delta n_{cl}}\right)_{Si} \Delta n_{bio} + \Delta\lambda_e \quad (6.4)$$

where  $\Delta\lambda_{Si}$  is the measured peak resonant wavelength shift in the  $i$ -th sensor;  $\left(\frac{\delta\lambda}{\delta T}\right)_{Si}$  and  $\left(\frac{\delta\lambda}{\delta n_{cl}}\right)_{Si}$  are the sensitivity of the  $i$ -th sensor to the temperature variations and the refractive index variations of the cladding medium respectively;  $\Delta n_{bio}$  is the refractive index change of interest, which is due to biomolecule reactions or concentration variations; and  $\Delta\lambda_e$  is the error in resonant shift. Assuming that the system of sensors is mostly experiencing common/correlated noises, and the random noise is negligible ( $\Delta\lambda_e \approx 0$ ), having two sensors will solve for the two unknowns  $\Delta T$  and  $\Delta n_{bio}$  in equation 6.4.

The change in refractive index of the cladding ( $\Delta n_{cl}$ ) is a function of temperature, concentrations, and/or biological reactions:

$$\Delta n_{cl} = \left(\frac{\delta n_{cl}}{\delta T_{cl}}\right) \Delta T + \Delta n_{bio} \quad (6.5)$$

## 6.2. System Design and Methods

---

where  $\Delta n_{cl}$  is the change in refractive index of the cladding due to temperature ( $\Delta T$ ) and biochemical changes ( $\Delta n_{bio}$ ) such as concentration variations, and  $\frac{\delta n_{cl}}{\delta T_{cl}}$  is the sensitivity of the refractive index of the cladding to the temperature variation of the cladding. Note that the wavelength shift contributed by the change in refractive index of analyte due to temperature is included in the first term of equation 6.4.

To demonstrate the capabilities of the proposed system of resonator sensors, we have designed and investigated a system of two resonator sensors. For this case, we can rewrite our matrix representation in equations 6.2 and 6.3. The first varying property is the change in the refractive index of the cladding ( $Var_1 = \Delta n_{cl}$ ), which is affected by temperature ( $Var_2 = \Delta T$ ), and the change of interest ( $Var_x = \Delta n_{bio}$ ). Therefore,

$$\begin{bmatrix} \Delta\lambda_{S1} \\ \Delta\lambda_{S2} \end{bmatrix} = \begin{bmatrix} \mathbf{S1} \\ \mathbf{S2} \end{bmatrix} \begin{bmatrix} \Delta n_{bio} \\ \Delta T \end{bmatrix} \quad (6.6)$$

where

$$\mathbf{S} = \begin{bmatrix} \mathbf{S1} \\ \mathbf{S2} \end{bmatrix} = \begin{bmatrix} \left(\frac{\delta\lambda}{\delta n_{cl}}\right)_{S1} & \left(\frac{\delta\lambda}{\delta T}\right)_{S1} \\ \left(\frac{\delta\lambda}{\delta n_{cl}}\right)_{S2} & \left(\frac{\delta\lambda}{\delta T}\right)_{S2} \end{bmatrix} \quad (6.7)$$

Therefore,

$$\begin{bmatrix} \Delta\lambda_{S1} \\ \Delta\lambda_{S2} \end{bmatrix} = \begin{bmatrix} (\frac{\delta\lambda}{\delta n_{cl}})_{S1} & (\frac{\delta\lambda}{\delta T})_{S1} \\ (\frac{\delta\lambda}{\delta n_{cl}})_{S2} & (\frac{\delta\lambda}{\delta T})_{S2} \end{bmatrix} \begin{bmatrix} \Delta n_{bio} \\ \Delta T \end{bmatrix} \quad (6.8)$$

To achieve the purposes of noise corrections with this system design, it is required to obtain two sensors with significantly different sensitivity properties (oppositely behaving); i.e. 1) a sensor with elevated sensitivity to the biomolecules in the cladding medium, and lower sensitivities to other system variations such as temperature variations, 2) a sensor with lower sensitivities to the cladding and higher sensitivity to temperature variations for example. A differential measurement is achieved when the responses of these sensors are significantly different. In other words, we are designing a sensitivity matrix (**S**) with a higher determinant. One way to build such a system is to have different waveguide thicknesses, which will allow different relative shifts, and thus, eliminating spurious effects and improving measurements repeatability. To investigate the proposed system design, we used ring resonators with various waveguide thicknesses [35, 99].

To demonstrate the capability of a two-resonator system, we have designed a cascade of two resonators with thicknesses of 220nm and 90nm (by using methods explained in Sections 2.2 and 3.2). These were fabricated in The Institute of Microelectronics in Singapore (IME). The resonator sensor with thinner waveguide core (90 nm thick silicon) serves as the sensor with higher sensitivity to cladding and lower sensitivity to temperature. In con-

trast, the resonator with the regular thickness of 220nm serves as the sensor with lower sensitivity to cladding and higher sensitivity to temperature (or reference sensor):

$$\left(\frac{\delta\lambda}{\delta n_{cl}}\right)_{S90} > \left(\frac{\delta\lambda}{\delta n_{cl}}\right)_{S220} \quad (6.9)$$

$$\left(\frac{\delta\lambda}{\delta T}\right)_{S90} < \left(\frac{\delta\lambda}{\delta T}\right)_{S220} \quad (6.10)$$

where,  $\left(\frac{\delta\lambda}{\delta n_{cl}}\right)_{S90}$  and  $\left(\frac{\delta\lambda}{\delta n_{cl}}\right)_{S220}$  are the sensitivities of the sensor to the variations of the refractive index of the cladding, and  $\left(\frac{\delta\lambda}{\delta T}\right)_{S90}$  and  $\left(\frac{\delta\lambda}{\delta T}\right)_{S220}$  are the sensitivities of the sensor to the temperature variations, for the sensor with silicon core thickness of 90 nm and 220 nm, respectively. According to simulated sensitivities, presented in figure 3.3, these sensitivity values for our designed system with two cascaded resonators are:  $\left(\frac{\delta\lambda}{\delta n_{cl}}\right)_{S90} \approx 120$  nm/RIU,  $\left(\frac{\delta\lambda}{\delta n_{cl}}\right)_{S220} \approx 56$  nm/RIU,  $\left(\frac{\delta\lambda}{\delta T}\right)_{S90} \approx 0.06$  nm/K, and  $\left(\frac{\delta\lambda}{\delta T}\right)_{S220} \approx 0.075$  nm/K. Based on these values for our designed sensors and equation 6.4, a system of two equations and two unknowns can be established to predict the variations of interest in the presence of temperature drifts.

## 6.3 Characterization and Performance of the Sensors and System

To demonstrate and experimentally validate the capabilities of our system, various concentrations of analytes over a range of temperatures were flown over our system of cascaded resonator sensors (using methods explained in

### 6.3. Characterization and Performance of the Sensors and System

---

Section 2.2). Specifically, four sets of data were collected. For each data set, various RI solutions were introduced to the cladding medium of our cascaded resonator sensors. Three sets were collected at controlled temperatures of 24, 25, and 26 °C. The last set was collected at a random temperature (i.e. without temperature controlling the experimental setup). Maintenance of slow flow is required in these experiments to avoid bubble generation and to allow the system to reach a steady-state temperature. If we assume negligible  $\Delta\lambda_e$  with controlled experiments, we can achieve temperature corrections using the response of two sensors.

Figure 6.1 (a,b) shows the wavelength shift responses of each of the two resonator sensors individually for the four sets of data explained above (three controlled and one random temperature). The results in figure 6.1 assumes a zero concentration at 25 °C as the reference point to demonstrate the relative shifts. When the temperature is controlled, a well-defined linear relation between the concentration and wavelength shift is observed. The linear relation describes the sensitivity of the sensor to the refractive index of cladding. Therefore, the shift of interest is the slope, and the shift due to temperature variations is the vertical distance (i.e. the offset between the lines for various temperatures).

$$\Delta\lambda_{total} = \Delta\lambda_{wanted} + \Delta\lambda_{unwanted} \quad (6.11)$$

Assuming that our sensing system had only one of these resonator sen-

### 6.3. Characterization and Performance of the Sensors and System

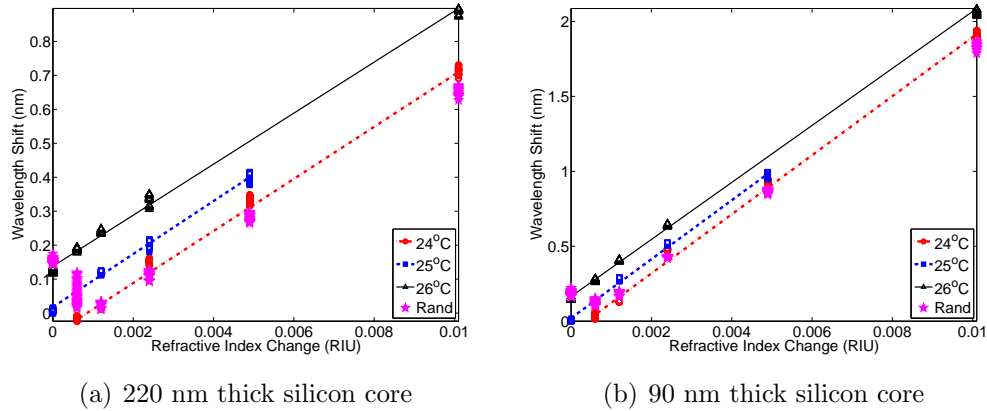


Figure 6.1: Response of each single resonator sensor, a) sensor with 220 nm thick silicon core, b) sensor with 90 nm thick silicon core, to the four data sets. Each sensor’s response to the three data sets with controlled temperature has a clear best fit line. However, it is clear that in the absence of a repeatable and accurate temperature controlling mechanism, the predictions are not reliable and the accuracy of predictions is significantly reduced.

sors, it is clear that without a well repeatable temperature controlled experiment, predicting the refractive index of the cladding accurately is challenging. Thus, the error of prediction/estimation is high.

Based on this set of calibration data, the ‘*unwanted*’ shift for both sensors are approximately similar. Therefore, subtracting the resonance wavelengths of the two sensors produces only the ‘*wanted*’ shift. Although not optimal, this differential measurement system improves the prediction results significantly. These promising results are due to significantly different sensitivities of the two resonator sensors to RI changes, where one is almost twice of the other.

Figure 6.2 shows the results of our differential measurement system, which

### 6.3. Characterization and Performance of the Sensors and System

---

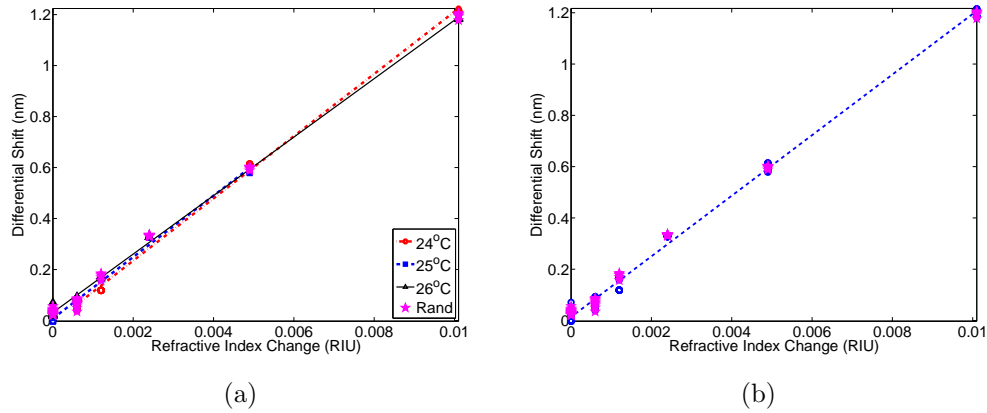


Figure 6.2: Response of the differential system of cascaded resonators to the four data sets. a) observing how each set fits. Dashed lines are the best fit lines for each data set (to compare with figure 6.1). b) observing how all the four sets fit. Dashed line is the best fit line to the three data sets with controlled temperature.

in this case is the difference between the resonance peak of the two resonator sensors. It can be well observed that the response of the system to the change in refractive index of cladding is the same at various temperatures. For initial demonstration, the differential calculation is performed on each temperature and the best-fit line was plotted for comparison to figure 6.1 (a,b). In figure 6.2 (b), the linear line is the best fit to the data from the three temperatures 24 °C, 25 °C, and 26 °C. The result of the random set is plotted as purple stars. Assuming that a linear model was built with the results from the three temperatures and was used to estimate the random set, we calculate the  $R^2$  value of prediction to be 0.996. If we only used the data at one temperature and used the sensors individually to build the model, we would have achieved  $R^2$  values of 0.9-0.95 and 0.4-0.74 for 90 nm

### 6.3. Characterization and Performance of the Sensors and System

and 220 nm thick resonator sensors respectively.

To observe the effect of differential system on a set of data where the temperature of the stage is not controlled, the response of the sensors to changes of concentration over time is plotted in figure 6.3 (a). Figure 6.3 (b) translates the same data in figure 6.3 (a) into our usual sensitivity plot to observe how the degree of the accuracy of concentration prediction/estimation improves with the differential system.

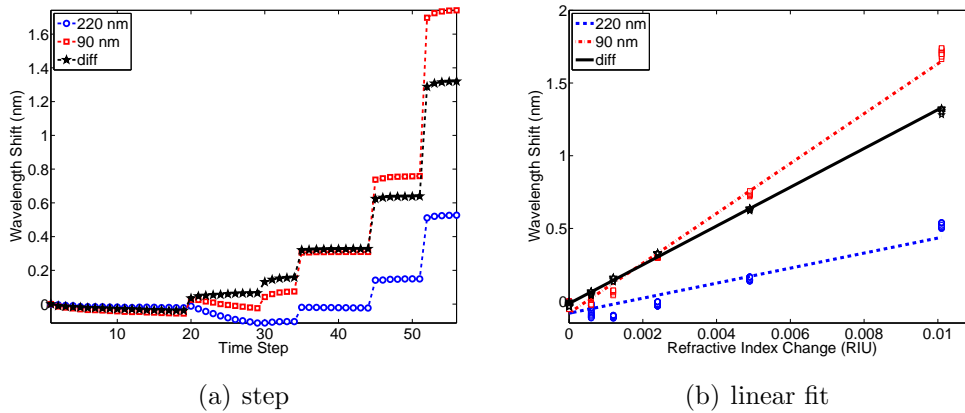


Figure 6.3: Response of the differential system (black) as well as each of the resonator sensors individually to a set of RI measurements where the temperature is not controlled. a) is the response over time as the reagent (RI solution) changes. b) plots the shift as a function of change in refractive index of the cladding, and the linear best fit line through the points to estimate the sensitivity and observe the accuracy of measurements.

## 6.4 Discussions and Conclusions

The differential system would perform best if there are multiple sensors with significantly different sensitivities to the cladding material (change in refractive index of the cladding) and the temperature of the waveguide. We assume that the system reaches a thermally steady state, meaning that the temperature of the silicon waveguides and the cladding are the same. Also, assuming that the dominant factor in the resonant shifts are temperature and concentration, we can solve equation 6.4 for our two sensors to obtain the two unknowns,  $\Delta T$  and  $\Delta n_{bio}$ . Furthermore, the resonant wavelength shift due to temperature variations can be extracted in order to obtain  $\Delta T$ .

One might think that having multiple identical sensors and averaging them would have similar effect. However, this would only reduce the random noise but not the undesired correlated shifts and drifts due to environmental variations that all sensors experience similarly. Therefore, it is important to have significantly different sensors that would respond to these common variations differently.

Regarding the optimization of our proposed system of differential measurement, let us write the two equations for the two sensors: *Sensor1* and *Sensor2*. *Sensor1* is assumed to have a higher sensitivity to the change in refractive index of the cladding.

$$\Delta\lambda_{Sensor1} = S_{T-1}\Delta T + S_{C-1}\Delta C \quad (6.12)$$

$$\Delta\lambda_{Sensor2} = S_{T-2}\Delta T + S_{C-2}\Delta C \quad (6.13)$$

where  $S_{T-1}$  and  $S_{T-2}$  are the sensitivities of *Sensor1* and *Sensor2*, respectively, to temperature variations;  $S_{C-1}$  and  $S_{C-2}$  are the sensitivities of *Sensor1* and *Sensor2*, respectively, to concentrations; and  $\Delta C$  is the concentration changes (change of interest). To remove the effect of temperature variations (the first term in the equations 6.12 and 6.13), we have to calculate a weighted difference of the responses of the two sensors:

$$\Delta\lambda_{System} = (S_{C-1} - \frac{S_{T-1}}{S_{T-2}}S_{C-2})\Delta C \quad (6.14)$$

Therefore, for improved higher sensitivity of our differential system, larger  $S_{C-1}$  and  $S_{T-2}$  as well as smaller  $S_{T-1}$  and  $S_{C-2}$  are preferred. Comparing this with the matrix representations in equations 6.6-6.8, it can be realized that maximizing the determinant of the  $\mathbf{S}$  matrix results in the optimum system performance.

The comparison of various two-sensor systems can be illustrated with the sensors that are developed in this thesis. The sensitivity matrices and their determinants can be derived from table 6.2.

Table 6.1 summarizes the specification of some of the previously discussed sensors. Table 6.2 is a summary of the calculated determinant of the sensitivity matrix ( $\mathbf{S}$ ) for various possible pairs with the sensors in table 6.1. Generally, for this specific case of extracting concentration changes in the presence of temperature variations, pairing the sensors with highest and low-

#### 6.4. Discussions and Conclusions

---

est ratio of temperature sensitivity/bulk sensitivity would result in the best performance (compare tables 6.1 and 6.2).

Table 6.1: Sensitivity vectors of a few sensors

Name	Pol. (Thick, Width) (nm, nm)	$S_{bulk}$	$S_T$	Ratio
		$\frac{\Delta\lambda_{res}}{\Delta n_{cl}} [\frac{nm}{RIU}]$	$\frac{\Delta\lambda_{res}}{\Delta T} [\frac{nm}{K}]$	$\frac{S_T}{S_{bulk}} [\frac{RIU}{K}]$
TE-220	TE (220, 500)	56	0.08	$1.4 \times 10^{-3}$
TE-90	TE (90, 900)	120	0.07	$5.8 \times 10^{-4}$
TM-220	TM (220, 750)	179	0.04	$2.2 \times 10^{-4}$
TM-150	TM (150, 900)	274	0.008	$2.9 \times 10^{-5}$

Table 6.2: Determinant of the sensitivity matrix for various combinations of a system of two resonator sensors

	TE-220	TE-90	TM-220	TM-150
TE-220	0	5.7	12.1	21.5
TE-90	5.7	0	7.7	18.2
TM-220	12.1	7.7	0	9.5
TM-150	21.5	18.2	9.5	0

In general, a better performance is achieved with a system of partially orthogonal sensors. This means that each sensor has significantly higher sensitivity to one parameter and significantly lower sensitivities to the other varying parameters in the system. For example, extending our system design

to  $n$  dimensions, if  $n$  sources of undesirable drifts and variations in the system are identified, designing  $n$  sensors, where each one is significantly more sensitive to one of these variations, is ideally desirable. With this  $n$  dimensional problem presented in equations 6.1-6.3, it can be observed that designing a diagonally-dominant matrix  $\mathbf{S}$ , with maximized determinant value, is required for the best performance of this proposed system of sensors.

# Chapter 7

## Conclusions and Future Work

In this thesis, we have investigated, developed, and demonstrated novel SOI-based optical sensors and sensing systems for the ultimate long-term goal of full sensing system on-chip advancement. The SOI-based sensor, being the core component of the sensing system, allows detection and quantification of target molecules. Therefore, improving the sensitivity, accuracy, repeatability, and reliability of the sensing system, within the constraints of MPW foundries, are critical steps towards our long-term goal. Efficient SOI-based sensors and system of sensors that are fabricated with standard CMOS processes, create a potential for integration of sensors with electronics and develop a sensing system-on-chip.

### 7.1 Summary and Conclusion

In summary, we have studied, theoretically and experimentally, SOI-based resonator sensors and system. We have proposed and demonstrated methods to improve the sensitivity of the sensors as single devices, investigated a novel method to integrate a detector with a sensor, and achieved a novel design of a

system of sensors, mimicking multivariate techniques, to correct for unwanted variations and to accomplish a more repeatable and accurate measurement in the presence of environmental variations.

Contributions of this thesis are:

- Proposed and investigated methods to improve the sensitivity of SOI-based sensors as a single device. The effect of waveguide core thickness on the sensitivity of our resonators was investigated both theoretically and experimentally. It was found that, for a TE guided mode, the sensitivity of a resonator sensor increases as the waveguide thickness decreases (from our conventional 220 nm thick silicon core) to approximately 35 nm thick silicon core. Therefore, the smallest thickness available through MPW foundry services, 90 nm thick silicon core, was used to design ultra-thin resonator sensors.
- Demonstrated analytically, by using fully-vectorial 2D eigenmode solver and analytical equations coded in MATLAB, the relationship between sensitivity of the sensor and the dimensions of the waveguide core.
- Designed and experimentally characterized resonator sensors with the thicknesses that were available through MPW foundries and were close to our analytical findings. Sensors with sensitivities of around 270 nm/RIU were accomplished.
- Investigation and demonstration of a novel method to integrate a detector with resonator sensors. Defect-mediated, ion-implanted, resonant-

enhanced photodetector sensors were designed and characterized.

- Proposed and demonstrated a novel design of a system of sensors. With this design, each sensor in the system, having various sensitivities to different variables, creates an equation with multiple unknowns. The relations and variability between these equations constitutes a system of equations and unknowns. The sensitivity components of all the sensors in the system generates a sensitivity matrix ( $\mathbf{S}$ ). This system is suitable for training a multivariate model to predict the variations of interest more accurately in the presence of ‘unwanted’ variations. The performance of this multivariate system depends on the determinant of  $\mathbf{S}$ . The higher the determinant, the higher is the degree of orthogonality, and therefore the system is more efficient. The  $R^2$  value of prediction was improved from 0.5 to 0.99.

## 7.2 Future Work

In this thesis, we have focused on optimizing sensor designs within the constraints of MPW foundries to prepare for future development of sensing system on-chip. To achieve this long-term goal, suggested improvements and future work include:

- Having achieved promising results with the design of a system of two sensors, the design of the system of cascaded sensors can be expanded to more sensors.

## 7.2. Future Work

---

- The proposed system of sensors, where each sensor is more sensitive to a specific variation, provides a set of suitable equations for development of a prediction model. Therefore, a prediction model can be developed, by using multivariate techniques, based on the system of equations that are formed as a results of our system of cascaded sensors.
- Investigation of different options for integrating photodetector with a system of resonator sensors on the same chip.
- A more thorough study of noises involved in the system, both from instrumentation and environmental variations, will be required to determine the specification of other components of the sensing system on chip (such as on-chip laser and detector). The overall performance of the sensing system is limited by the combination of the performances of all components.
- Integration of the sensing systems with electronics on the same chip, as a step towards lab-on-chip (LoC) or sensing systems on chips (SSOCs)

# Bibliography

- [1] R. M. Lequin, “Enzyme immunoassay (eia)/enzyme-linked immunosorbent assay (elisa),” *Clinical chemistry*, vol. 51, no. 12, pp. 2415–2418, 2005.
- [2] J. L. Arlett, E. B. Myers, and M. L. Roukes, “Comparative advantages of mechanical biosensors,” *Nat Nano*, vol. 6, no. 4, pp. 203–215, 04 2011. [Online]. Available: <http://dx.doi.org/10.1038/nnano.2011.44>
- [3] V. Gubala, L. F. Harris, A. J. Ricco, M. X. Tan, and D. E. Williams, “Point of care diagnostics: status and future,” *Analytical chemistry*, vol. 84, no. 2, pp. 487–515, 2011.
- [4] C. D. Chin, V. Linder, and S. K. Sia, “Commercialization of microfluidic point-of-care diagnostic devices,” *Lab on a Chip*, vol. 12, no. 12, pp. 2118–2134, 2012.
- [5] R. Etzioni, N. Urban, S. Ramsey, M. McIntosh, S. Schwartz, B. Reid, J. Radich, G. Anderson, and L. Hartwell, “The case for early detection,” *Nature Reviews Cancer*, vol. 3, no. 4, pp. 243–252, 2003.
- [6] J. T. Kindt, M. S. Luchansky, A. J. Qavi, S.-H. Lee, and R. C. Bailey, “Subpicogram per milliliter detection of interleukins using silicon photonic microring resonators and an enzymatic signal enhancement strategy,” *Analytical Chemistry*, vol. 85, no. 22, pp. 10 653–10 657, 2013, pMID: 24171505.
- [7] M. S. Luchansky and R. C. Bailey, “Silicon photonic microring resonators for quantitative cytokine detection and T-cell secretion analysis,” *Anal. Chem.*, vol. 82, no. 5, pp. 1975–1981, 2010.
- [8] A. L. Washburn, L. C. Gunn, and R. C. Bailey, “Label-free quantitation of a cancer biomarker in complex media using silicon photonic

- microring resonators,” *Anal. Chem.*, vol. 81, no. 22, pp. 9499–9506, 2009.
- [9] M. Iqbal, M. A. Gleeson, B. Spaugh, F. Tybor, W. G. Gunn, M. Hochberg, T. Baehr-Jones, R. C. Bailey, and L. C. Gunn, “Label-free biosensor arrays based on silicon ring resonators and high-speed optical scanning instrumentation,” *IEEE J. Quantum Electron.*, vol. 16, no. 3, pp. 654–661, 2010.
- [10] A. J. Qavi and R. C. Bailey, “Multiplexed detection and label-free quantitation of MicroRNAs using arrays of silicon photonic microring resonators,” *Angewandte Chemie*, vol. 122, no. 27, pp. 4712–4715, 2010.
- [11] A. L. Washburn, M. S. Luchansky, A. L. Bowman, and R. C. Bailey, “Quantitative, label-free detection of five protein biomarkers using multiplexed arrays of silicon photonic microring resonators,” *Analytical chemistry*, vol. 82, no. 1, pp. 69–72, 2009.
- [12] J. K. Doylend and A. P. Knights, “The evolution of silicon photonics as an enabling technology for optical interconnection,” *Laser & Photon. Rev.*, vol. 6, no. 4, pp. 504–525, 2012.
- [13] W. Shi, H. Yun, C. Lin, J. Flueckiger, N. A. F. Jaeger, and L. Chrostowski, “Coupler-apodized bragg-grating add-drop filter,” *Opt. Lett.*, vol. 38, pp. 3068–3070, 08/2013 2013.
- [14] W. Shi, X. Wang, W. Zhang, H. Yun, N. A. F. Jaeger, and L. Chrostowski, “Integrated microring add-drop filters with contradirectional couplers,” *CLEO (Conference on Lasers and Electro-Optics) 2012*, p. JW4A.91, 05/2012 2012.
- [15] R. Soref, “The Past, Present, and Future of Silicon Photonics,” *Selected Topics in Quantum Electronics, IEEE Journal of*, vol. 12, no. 6, pp. 1678–1687, Nov. 2006.
- [16] N. A. Yebo, D. Taillaert, J. Roels, D. Lahem, M. Debliquy, P. Lommens, Z. Hens, and R. Baets, “Integrated optical gas sensors on silicon-on-insulator platform,” in *Proceedings of the 2009 Annual Symposium of the IEEE Photonics Benelux Chapter*, S. Beri, P. Tassin, G. Craggs, X. Leijtens, and J. Danckaert, Eds. VUB Press, 2009, pp. 153–156.

- [17] L. Chrostowski, S. Grist, J. Flueckiger, W. Shi, X. Wang, E. Ouellet, H. Yun, M. Webb, B. Nie, Z. Liang, K. C. Cheung, S. A. Schmidt, D. M. Ratner, and N. A. F. Jaeger, “Silicon photonic resonator sensors and devices,” *Proc. SPIE*, vol. 8236, no. 1, pp. 823 620–823 620–16, Feb. 2012.
- [18] O. Scheler, J. T. Kindt, A. J. Qavi, L. Kaplinski, B. Glynn, T. Barry, A. Kurg, and R. C. Bailey, “Label-free, multiplexed detection of bacterial tmRNA using silicon photonic microring resonators,” *Biosens. Bioelectron.*, vol. 36, no. 1, pp. 56–61, 2012.
- [19] W. W. Shia and R. C. Bailey, “Single domain antibodies for the detection of ricin using silicon photonic microring resonator arrays,” *Anal. Chem.*, vol. 85, no. 2, pp. 805–810, 2012.
- [20] M. R. Tomita, L. S. Russ, R. Sridhar, and B. J. Naughton, “Smart home with healthcare technologies for community-dwelling older adults,” *Available as on 13th of March*, 2012.
- [21] X. Fan, I. White, S. Shopova, H. Zhu, J. Suter, and Y. Sun, “Sensitive optical biosensors for unlabeled targets: A review,” *Analytica Chimica Acta*, vol. 620, no. 1-2, pp. 8–26, Jul. 2008.
- [22] F. Vollmer and L. Yang, “Review Label-free detection with high-Q microcavities: a review of biosensing mechanisms for integrated devices,” *Nanophotonics*, vol. 1, no. 3-4, Jan. 2012.
- [23] <https://www.biacore.com/lifesciences/company/index.html>, “Ge healthcare,” 2013-01-23. [Online]. Available: <https://www.biacore.com/lifesciences/company/index.html>
- [24] V. M. Passaro, F. Dell’olio, B. Casamassima, and F. D. Leonardis, “Guided-Wave Optical Biosensors,” *Sensors*, vol. 7, pp. 508–539, 2007.
- [25] C. F. Donzella V, “Optical biosensors to analyze novel biomarkers in oncology,” *J Biophotonics*, vol. 4, no. 6, pp. 442–452, 2011.
- [26] F. Vollmer, S. Arnold, D. Braun, I. Teraoka, and A. Libchaber, “Multiplexed DNA quantification by spectroscopic shift of two microsphere cavities.” *Biophysical journal*, vol. 85, no. 3, pp. 1974–1979, Sep. 2003.

- [27] C. L. Arce, K. De Vos, T. Claes, K. Komorowska, D. Van Thourhout, and P. Bienstman, “Silicon-on-insulator microring resonator sensor integrated on an optical fiber facet,” *IEEE Photon. Tech. Lett.*, vol. 23, no. 13, pp. 890–892, 2011.
- [28] S. M. Grist, S. A. Schmidt, J. Flueckiger, V. Donzella, W. Shi, S. Talebi Fard, J. T. Kirk, D. M. Ratner, K. C. Cheung, and L. Chrostowski, “Silicon photonic micro-disk resonators for label-free biosensing,” *Opt. Express*, vol. 21, pp. 7994–8006, 03/2013 2013.
- [29] S. Mandal and D. Erickson, “Nanoscale optofluidic sensor arrays,” *Opt. Express*, vol. 16, no. 3, p. 1623, 2008.
- [30] X. Wang, J. Flueckiger, S. Schmidt, S. Grist, S. Talebi Fard, J. Kirk, M. Doerfler, K. C. Cheung, D. M. Ratner, and L. Chrostowski, “A silicon photonic biosensor using phase-shifted bragg gratings in slot waveguide,” *J. Biophotonics*, 04/2013 2013.
- [31] P. Dumon, W. Bogaerts, V. Wiaux, J. Wouters, S. Beckx, J. Van Campenhout, D. Taillaert, B. Luyssaert, P. Bienstman, D. Van Thourhout, and R. Baets, “Low-loss SOI photonic wires and ring resonators fabricated with deep UV lithography,” *IEEE Photon. Tech. Lett.*, vol. 16, no. 5, pp. 1328–1330, May 2004.
- [32] H. Mukundan, A. S. Anderson, W. K. Grace, K. M. Grace, N. Hartman, J. S. Martinez, and B. I. Swanson, “Waveguide-based biosensors for pathogen detection,” *Sensors*, vol. 9, no. 7, pp. 5783–5809, 2009.
- [33] F. Dell’Olio and V. M. Passaro, “Optical sensing by optimized silicon slot waveguides,” *Opt. Express*, vol. 15, no. 8, pp. 4977–4993, Apr. 2007.
- [34] S. Talebi Fard, S. M. Grist, V. Donzella, S. A. Schmidt, J. Flueckiger, X. Wang, W. Shi, A. Millspaugh, M. Webb, D. M. Ratner, K. C. Cheung, and L. Chrostowski, “Label-free silicon photonic biosensors for use in clinical diagnostics,” *Proc. SPIE, Silicon Photonics VIII*, vol. 8629, pp. 862909–14, 02/2013 2013.
- [35] S. Talebi Fard, V. Donzella, S. A. Schmidt, J. Flueckiger, S. M. Grist, P. TalebiFard, Y. Wu, R. J. Bojko, E. Kwok, N. A. Jaeger, D. M. Rat-

- ner, and L. Chrostowski, “Performance of ultra-thin SOI-based resonators for sensing applications,” *Opt. Express*, vol. 22, no. 12, pp. 14 166–14 179, 2014.
- [36] K. Zinoviev, L. G. Carrascosa, J. Sánchez del Río, B. Sepúlveda, C. Domínguez, and L. M. Lechuga, “Silicon photonic biosensors for lab-on-a-chip applications,” *Advances in Optical Technologies*, vol. 2008, 2008.
- [37] J. Arlett, E. Myers, and M. Roukes, “Comparative advantages of mechanical biosensors,” *Nature nanotechnology*, vol. 6, no. 4, pp. 203–215, 2011.
- [38] C. W. Heath, “Pesticides and cancer risk,” *Cancer*, vol. 80, no. 10, pp. 1887–1888, 1997.
- [39] S. Laschi, D. Ogończyk, I. Palchetti, and M. Mascini, “Evaluation of pesticide-induced acetylcholinesterase inhibition by means of disposable carbon-modified electrochemical biosensors,” *Enzyme and Microbial Technology*, vol. 40, no. 3, pp. 485–489, 2007.
- [40] <http://www.epixfab.eu>, “epixfab: The silicon photonics platform,” 2013-01-22. [Online]. Available: <http://www.epixfab.eu>.
- [41] I. M. White and X. Fan, “On the performance quantification of resonant refractive index sensors,” *Opt. Express*, vol. 16, no. 2, pp. 1020–1028, 2008.
- [42] T. Yoshie, L. Tang, and S.-Y. Su, “Optical microcavity: Sensing down to single molecules and atoms,” *Sensors*, vol. 11, no. 2, pp. 1972–1991, 2011.
- [43] J. Ackert, J. Doylend, D. Logan, P. Jessop, R. Vafaei, L. Chrostowski, and A. Knights, “Defect-mediated resonance shift of silicon-on-insulator racetrack resonators,” *Opt. Express*, vol. 19, no. 13, pp. 11 969–11 976, 2011.
- [44] L. Chrostowski and M. Hochberg, *Silicon Photonics Design*, ser. Cambridge University Press, 2015.

- [45] Y. Wang, X. Wang, J. Flueckiger, H. Yun, W. Shi, R. Bojko, N. A. F. Jaeger, and L. Chrostowski, “Focusing sub-wavelength grating couplers with low back reflections for rapid prototyping of silicon photonic circuits,” *Opt. Express*, vol. 22, no. 17, pp. 20 652–20 662, Aug 2014.
- [46] V. V. Tuchin, I. L. Maksimova, D. A. Zimnyakov, I. L. Kon, A. H. Mavlyutov, and A. A. Mishin, “Light propagation in tissues with controlled optical properties,” *J. Biomed. Opt.*, vol. 2, no. 4, pp. 401–417, 1997.
- [47] R. Sokoloff, K. Norton, C. Gasior, K. Marker, and L. Grauer, “A dual-monoclonal sandwich assay for prostate-specific membrane antigen: levels in tissues, seminal fluid and urine.” *Prostate*, vol. 43, no. 2, pp. 150–7, 2000.
- [48] U. B. Nielsen and B. H. Geierstanger, “Multiplexed sandwich assays in microarray format,” *Journal of immunological methods*, vol. 290, pp. 107–120, 2004.
- [49] X. Wang, W. Shi, S. Grist, H. Yun, and N. A. F. J. Chrostowski, “Narrow-Band Transmission Filter using Phase-Shifted Bragg Gratings in SOI Waveguide,” 10/2011 2011, p. ThZ1.
- [50] V. R. Almeida, Q. Xu, C. A. Barrios, and M. Lipson, “Guiding and confining light in void nanostructure,” *Opt. Lett.*, vol. 29, no. 11, pp. 1209–1211, 2004.
- [51] E. L. Florin, V. T. Moy, and H. E. Gaub, “Adhesion forces between individual ligand-receptor pairs,” *Science (New York, NY)*, vol. 264, p. 415, 1994.
- [52] S. Mandal, J. M. Goddard, and D. Erickson, “A multiplexed optofluidic biomolecular sensor for low mass detection,” *Lab on a Chip*, vol. 9, pp. 2924–2932, 2009.
- [53] K. D. Vos, I. Bartolozzi, E. Schacht, P. Bienstman, and R. Baets, “Silicon-on-insulator microring resonator for silicon-on-insulator microring resonator for sensitive and label-free biosensing,” *Opt. Express*, vol. 15, no. 12, pp. 7610–7615, 2007.

- [54] D.-X. Xu, M. Vachon, A. Densmore, R. Ma, S. Janz, A. Delâge, J. Lapointe, P. Cheben, J. Schmid, E. Post *et al.*, “Real-time cancellation of temperature induced resonance shifts in SOI wire waveguide ring resonator label-free biosensor arrays,” *Opt. Express*, vol. 18, no. 22, pp. 22 867–22 879, 2010.
- [55] T. Claes, J. G. Molera, K. De Vos, E. Schacht, R. Baets, and P. Bienstman, “Label-free biosensing with a slot-waveguide-based ring resonator in silicon on insulator,” *IEEE J. Photonics*, vol. 1, no. 3, pp. 197–204, 2009.
- [56] A. Densmore, D.-X. Xu, P. Waldron, S. Janz, P. Cheben, J. Lapointe, A. Delâge, B. Lamontagne, J. Schmid, and E. Post, “A silicon-on-insulator photonic wire based evanescent field sensor,” *IEEE Photon. Tech. Lett.*, vol. 18, no. 23, pp. 2520–2522, 2006.
- [57] G. Veldhuis, O. Parriaux, H. Hoekstra, and P. Lambeck, “Sensitivity enhancement in evanescent optical waveguide sensors,” *J. Lightwave Tech.*, vol. 18, no. 5, p. 677, 2000.
- [58] M. Gould, A. Pomerene, C. Hill, S. Ocheltree, Y. Zhang, T. Baehr-Jones, and M. Hochberg, “Ultra-thin silicon-on-insulator strip waveguides and mode couplers,” *Appl. Phys. Lett.*, vol. 101, no. 22, pp. 221 106–221 106, 2012.
- [59] H. Li, “Refractive index of silicon and germanium and its wavelength and temperature derivatives,” *J. Phys. and Chem. Ref. data*, vol. 9, no. 3, pp. 561–658, 1980.
- [60] B. J. Frey, D. B. Leviton, and T. J. Madison, “Temperature-dependent refractive index of silicon and germanium,” in *Astronomical Telescopes and Instrumentation*. International Society for Optics and Photonics, 2006, pp. 62 732J–62 732J.
- [61] A. N. Bashkatov and E. A. Genina, “Water refractive index in dependence on temperature and wavelength: a simple approximation,” in *Saratov Fall Meeting 2002: Optical Technologies in Biophysics and Medicine IV*. International Society for Optics and Photonics, 2003, pp. 393–395.

- [62] G. Abbate, U. Bernini, E. Ragozzino, and F. Somma, “The temperature dependence of the refractive index of water,” *J. Phys. D: Appl. Phys.*, vol. 11, no. 8, p. 1167, 1978.
- [63] W. Bogaerts, V. Wiaux, D. Taillaert, S. Beckx, B. Luyssaert, P. Bienstman, and R. Baets, “Fabrication of photonic crystals in silicon-on-insulator using 248-nm deep uv lithography,” *IEEE journal of selected topics in quantum electronics*, vol. 8, no. 4, pp. 928–934, 2002.
- [64] M. Hochberg, “Integrated ultrafast nonlinear optical devices in silicon,” Ph.D. dissertation, California Institute of Technology, 2006.
- [65] T. Baehr-Jones, M. Hochberg, C. Walker, and A. Scherer, “High Q ring resonators in thin silicon-on-insulator,” *Appl. Phys. Lett.*, vol. 85, no. 16, pp. 3346–3347, 2004.
- [66] F. Grillot, L. Vivien, S. Laval, and E. Cassan, “Propagation loss in single-mode ultrasmall square silicon-on-insulator optical waveguides,” *J. Lightwave Tech.*, vol. 24, no. 2, p. 891, 2006.
- [67] J. McCaulley, V. Donnelly, M. Vernon, and I. Taha, “Temperature dependence of the near-infrared refractive index of silicon, gallium arsenide, and indium phosphide,” *Phys. Rev. B*, vol. 49, no. 11, p. 7408, 1994.
- [68] Y. Wang, J. Flueckiger, C. Lin, and L. Chrostowski, “Universal grating coupler design,” *Proc. SPIE*, vol. 8915, pp. 89 150Y–89 150Y–7, 2013.
- [69] X. Wang, S. Grist, J. Flueckiger, N. A. Jaeger, and L. Chrostowski, “Silicon photonic slot waveguide bragg gratings and resonators,” *Opt. Express*, vol. 21, no. 16, pp. 19 029–19 039, 2013.
- [70] F. Payne and J. Lacey, “A theoretical analysis of scattering loss from planar optical waveguides,” *Opt. and Quantum Electron.*, vol. 26, no. 10, pp. 977–986, 1994.
- [71] P. Dong, W. Qian, S. Liao, H. Liang, C.-C. Kung, N.-N. Feng, R. Shafiqi, J. Fong, D. Feng, A. V. Krishnamoorthy *et al.*, “Low loss shallow-ridge silicon waveguides,” *Opt. Express*, vol. 18, no. 14, pp. 14 474–14 479, 2010.

- [72] F. Grillot, L. Vivien, S. Laval, D. Pascal, and E. Cassan, “Size influence on the propagation loss induced by sidewall roughness in ultrasmall soi waveguides,” *Photonics Technology Letters, IEEE*, vol. 16, no. 7, pp. 1661–1663, 2004.
- [73] J. Vörös, “The density and refractive index of adsorbing protein layers,” *Biophysical journal*, vol. 87, no. 1, pp. 553–561, 2004.
- [74] A. Yariv and P. Yeh, *Photonics: Optical Electronics in Modern Communications (The Oxford Series in Electrical and Computer Engineering)*. Oxford University Press, Inc., 2006.
- [75] “IME,” 2015-01. [Online]. Available: <http://www.a-star.edu.sg/ime/>
- [76] S. Schmidt, J. Flueckiger, W. Wu, S. M. Grist, S. Talebi Fard, V. Donzella, P. Khumwan, E. R. Thompson, Q. Wang, P. Kulik, X. Wang, A. Sherwali, J. Kirk, K. C. Cheung, L. Chrostowski, and D. Ratner, “Improving the performance of silicon photonic rings, disks, and bragg gratings for use in label-free biosensing,” *Proc. SPIE, Biosensing and Nanomedicine VII*, vol. 9166, p. 91660M, 08/2014 2014.
- [77] L. Chrostowski, X. Wang, J. Flueckiger, Y. Wu, Y. Wang, and S. Talebi Fard, “Impact of fabrication non-uniformity on chip-scale silicon photonic integrated circuits,” in *Optical Fiber Communication Conference*. Optical Society of America, 2014, pp. Th2A–37.
- [78] I. Teraoka and S. Arnold, “Theory of resonance shifts in TE and TM whispering gallery modes by nonradial perturbations for sensing applications,” *JOSA B*, vol. 23, no. 7, pp. 1381–1389, 2006.
- [79] G. Moța, I. Moraru, J. Sjöquist, and V. Gheție, “Protein a as a molecular probe for the detection of antigen induced conformational change in Fc region of rabbit antibody,” *Molecular immunology*, vol. 18, no. 5, pp. 373–378, 1981.
- [80] W. L. DeLano, M. H. Ultsch, J. A. Wells *et al.*, “Convergent solutions to binding at a protein-protein interface,” *Science*, vol. 287, no. 5456, pp. 1279–1283, 2000.

- [81] P. C. Weber, D. Ohlendorf, J. Wendoloski, and F. Salemme, “Structural origins of high-affinity biotin binding to streptavidin,” *Science*, vol. 243, no. 4887, pp. 85–88, 1989.
- [82] M. Graille, E. A. Stura, A. L. Corper, B. J. Sutton, M. J. Taussig, J.-B. Charbonnier, and G. J. Silverman, “Crystal structure of a staphylococcus aureus protein A domain complexed with the fab fragment of a human IgM antibody: structural basis for recognition of b-cell receptors and superantigen activity,” *Proceedings of the National Academy of Sciences*, vol. 97, no. 10, pp. 5399–5404, 2000.
- [83] H. P. Erickson, “Size and shape of protein molecules at the nanometer level determined by sedimentation, gel filtration, and electron microscopy,” *Biological procedures online*, vol. 11, no. 1, pp. 32–51, 2009.
- [84] M. C. Coen, R. Lehmann, P. Gröning, M. Biemann, C. Galli, and L. Schlapbach, “Adsorption and bioactivity of protein A on silicon surfaces studied by AFM and XPS,” *Journal of colloid and interface science*, vol. 233, no. 2, pp. 180–189, 2001.
- [85] S. Talebi Fard, K. Murray, M. Caverley, V. Donzella, J. Flueckiger, S. M. Grist, E. Huante-Ceron, S. A. Schmidt, E. Kwok, N. A. Jaeger *et al.*, “Silicon-on-insulator sensors using integrated resonance-enhanced defect-mediated photodetectors,” *Opt. express*, vol. 22, no. 23, pp. 28 517–28 529, 2014.
- [86] A. Gassenq, N. Hattasan, L. Cerutti, J. B. Rodriguez, E. Tournié, and G. Roelkens, “Study of evanescently-coupled and grating-assisted GaInAsSb photodiodes integrated on a silicon photonic chip,” *Opt. Express*, vol. 20, no. 11, pp. 11 665–11 672, 2012.
- [87] H. Park, A. W. Fang, R. Jones, O. Cohen, O. Raday, M. N. Sysak, M. J. Paniccia, and J. E. Bowers, “A hybrid AlGaInAs-silicon evanescent waveguide photodetector,” *Opt. Express*, vol. 15, no. 10, p. 60446052, 2007.
- [88] J. Brouckaert, G. Roelkens, D. Van Thourhout, and R. Baets, “Compact InAlAs-InGaAs metal-semiconductor-metal photodetectors integrated on silicon-on-insulator waveguides,” *IEEE Photon. Tech. Lett.*, vol. 19, no. 19, pp. 1484–1486, Oct. 2007.

- [89] J. Michel, J. Liu, and L. C. Kimerling, “High-performance Ge-on-Si photodetectors,” *Nature Photonics*, vol. 4, no. 8, pp. 527–534, 2010.
- [90] L. Vivien, J. Osmond, J.-M. Fdli, D. Marris-Morini, P. Crozat, J.-F. Damlencourt, E. Cassan, Y. Lecunff, and S. Laval, “42 GHz PIN germanium photodetector integrated in a silicon-on-insulator waveguide,” *Opt. Express*, vol. 17, no. 8, pp. 6252–6257, 2009.
- [91] L. Virot, L. Vivien, A. Polzer, D. Marris-Morini, J. Osmond, J. M. Hartmann, P. Crozat, E. Cassan, C. Baudot, C. Kopp, F. Boeuf, H. Zimmermann, and J. M. Fdli, “40 Gbit/s germanium waveguide photodetector on silicon,” L. Vivien, S. K. Honkanen, L. Pavesi, and S. Pelli, Eds., Jun. 2012, pp. 84 310A–84 310A–7.
- [92] C. T. DeRose, D. C. Trotter, W. A. Zortman, A. L. Starbuck, M. Fisher, M. R. Watts, and P. S. Davids, “Ultra compact 45 GHz CMOS compatible germanium waveguide photodiode with low dark current,” *Opt. Express*, vol. 19, no. 25, pp. 24 897–24 904, 2011.
- [93] L. Vivien, A. Polzer, D. Marris-Morini, J. Osmond, J. M. Hartmann, P. Crozat, E. Cassan, C. Kopp, H. Zimmermann, and J. M. Fdli, “Zero-bias 40Gbit/s germanium waveguide photodetector on silicon,” *Opt. Express*, vol. 20, no. 2, pp. 1096–1101, 2012.
- [94] J. Ackert, A. Knights, M. Fiorentino, R. Beausoleil, and P. Jessop, “Defect enhanced silicon-on-insulator microdisk photodetector,” in *Optical Interconnects Conference, 2012 IEEE*. IEEE, 2012, pp. 76–77.
- [95] J. J. Ackert, M. Fiorentino, D. F. Logan, R. G. Beausoleil, P. E. Jessop, and A. P. Knights, “Silicon-on-insulator microring resonator defect-based photodetector with 3.5-GHz bandwidth,” *J. Nanophotonics*, vol. 5, no. 1, pp. 059 507–059 507, 2011.
- [96] D. F. Logan, P. Velha, M. Sorel, R. M. De La Rue, P. E. Jessop, and A. P. Knights, “Monitoring and tuning micro-ring properties using defect-enhanced silicon photodiodes at 1550 nm,” *IEEE Photon. Tech. Lett.*, vol. 24, no. 4, pp. 261–263, 2012.
- [97] D. F. Logan, P. Velha, M. Sorel, R. De La Rue, A. P. Knights, and P. E. Jessop, “Defect-enhanced silicon-on-insulator waveguide resonant

- photodetector with high sensitivity at 1.55  $\mu\text{m}$ ,” *IEEE Photon. Tech. Lett.*, vol. 22, no. 20, pp. 1530–1532, 2010.
- [98] D. F. Logan, P. E. Jessop, and A. P. Knights, “Modeling defect enhanced detection at 1550 nm in integrated silicon waveguide photodetectors,” *J. Lightwave Tech.*, vol. 27, no. 7, pp. 930–937, 2009.
- [99] S. Talebi Fard, V. Donzella, S. Schmidt, D. Ratner, R. Bojko, and L. Chrostowski, “Sensitivity analysis of thin waveguide SOI ring resonators for sensing applications,” in *Photonics Conference (IPC), 2013 IEEE*. IEEE, 2013, pp. 616–617.
- [100] R. R. Grote, K. Padmaraju, B. Souhan, J. B. Driscoll, K. Bergman, and R. Osgood, “10 Gb/s error-free operation of all-silicon ion-implanted-waveguide photodiodes at 1.55  $\mu\text{m}$ ,” *IEEE Photon. Tech. Lett.*, vol. 25, no. 1, pp. 67–70, 2013.
- [101] J. Doylend, P. Jessop, and A. Knights, “Silicon photonic resonator-enhanced defect-mediated photodiode for sub-bandgap detection,” *Opt. Express*, vol. 18, no. 14, pp. 14 671–14 678, 2010.
- [102] M. S. Luchansky, A. L. Washburn, T. A. Martin, M. Iqbal, L. C. Gunn, and R. C. Bailey, “Characterization of the evanescent field profile and bound mass sensitivity of a label-free silicon photonic microring resonator biosensing platform,” *Biosens. Bioelectron.*, vol. 26, no. 4, pp. 1283–1291, 2010.
- [103] A. Densmore, M. Vachon, D.-X. Xu, S. Janz, R. Ma, Y.-H. Li, G. Lopinski, A. Del age, J. Lapointe, C. Luebbert, Q. Y. Liu, P. Cheben, and J. H. Schmid, “Silicon photonic wire biosensor array for multiplexed, real-time and label-free molecular detection,” *Opt. Lett.*, vol. 34, no. 23, pp. 3598–3600, 2009.
- [104] P. J. Foster, J. K. Doylend, P. Mascher, A. P. Knights, and P. G. Coleman, “Optical attenuation in defect-engineered silicon rib waveguides,” *J. Appl. Phys.*, vol. 99, no. 7, pp. –, 2006.
- [105] D. Logan, K. Murray, J. Ackert, P. Velha, M. Sorel, R. M. De La Rue, P. Jessop, and A. Knights, “Analysis of resonance enhancement in defect-mediated silicon micro-ring photodiodes operating at 1550 nm,” *J. Optics*, vol. 13, no. 12, p. 125503, 2011.

- [106] M. Geis, S. Spector, M. Grein, J. Yoon, D. Lennon, and T. Lyszczarz, “Silicon waveguide infrared photodiodes with  $>35$  GHz bandwidth and phototransistors with  $50 \text{ AW}^{-1}$  response,” *Opt. Express*, vol. 17, no. 7, pp. 5193–5204, 2009.
- [107] K. De Vos, “Label-free silicon photonics biosensor platform with microring resonators.” Ph.D. dissertation, Ghent University, 2010.
- [108] M. Á. Guillén-Torres, E. Cretu, N. A. Jaeger, and L. Chrostowski, “Ring resonator optical gyroscopes parameter optimization and robustness analysis,” *Journal of Lightwave Technology*, vol. 30, no. 12, pp. 1802–1817, 2012.
- [109] F. Ghasemi, M. Chamanzar, A. A. Eftekhar, and A. Adibi, “An efficient technique for the reduction of wavelength noise in resonance-based integrated photonic sensors,” *Analyst*, vol. 139, pp. 5901–5910, 2014. [Online]. Available: <http://dx.doi.org/10.1039/C4AN01292E>
- [110] *Agilent 81682A Tunable Laser Modules User’s Guide, Sixth Edition.*
- [111] J. Schmid, M. Ibrahim, P. Cheben, J. Lapointe, S. Janz, P. Bock, A. Densmore, B. Lamontagne, R. Ma, W. Ye *et al.*, “Temperature-independent silicon subwavelength grating waveguides,” *Optics letters*, vol. 36, no. 11, pp. 2110–2112, 2011.
- [112] J. Teng, P. Dumon, W. Bogaerts, H. Zhang, X. Jian, X. Han, M. Zhao, G. Morthier, and R. Baets, “Athermal silicon-on-insulator ring resonators by overlaying a polymer cladding on narrowed waveguides,” *Optics express*, vol. 17, no. 17, pp. 14627–14633, 2009.
- [113] V. Raghunathan, W. N. Ye, J. Hu, T. Izuhara, J. Michel, and L. Kimerling, “Athermal operation of silicon waveguides: spectral, second order and footprint dependencies,” *Optics express*, vol. 18, no. 17, pp. 17631–17639, 2010.
- [114] S. Talebi Fard, L. Chrostowski, E. Kwok, and M.-C. Amann, “Chemo-metric approach for improving VCSEL-based glucose predictions,” *IEEE Trans. Biomed. Eng.*, vol. 57, no. 3, pp. 578–585, 2010.
- [115] S. Talebi Fard, W. Hofmann, P. Talebi Fard, E. Kwok, M.-C. Amann, and L. Chrostowski, “Optical glucose monitoring using vertical cavity

surface emitting lasers (vcsels),” in *Proc. SPIE*, vol. 7397, 2009, p. 739704.

- [116] K. B. Gylfason, C. F. Carlborg, A. Kazmierczak, F. Dortu, L. Vivien, C. A. Barrios, W. van der Wijngaart, G. Stemme *et al.*, “On-chip temperature compensation in an integrated slot-waveguide ring resonator refractive index sensor array,” *Opt. Express*, vol. 18, no. 4, pp. 3226–3237, 2010.

# Appendix A

## List of Publications

1. **Sahba Talebi Fard**, et al., “Optimized Sensitivity of Silicon-on-Insulator Strip Waveguide Resonator Sensor”, In review (2014).
2. **Sahba Talebi Fard**, V. Donzella, S. Schmidt, J. Flueckiger, S. Grist, P. TalebiFard, Y. Wu, R. Bojko, E. Kwok, N. Jaeger, D. Ratner, and L. Chrostowski, ”Performance of ultra-thin SOI-based resonators for sensing applications.” *Optics Express* 22, no. 12 (2014): 14166-14179.
3. **Sahba Talebi Fard**, K. Murray, M. Caverley, V. Donzella, J. Flueckiger, S. Grist, E. Huante-Ceron, S. Schmidt, E. Kwok, N. Jaeger, A. Knights, and L. Chrostowski, ”Silicon-on-insulator sensors using integrated resonance-enhanced defect-mediated photodetectors.” *Optics Express* 22, no. 23 (2014): 28517-28529.
4. **Sahba Talebi Fard**, S. Grist, V. Donzella, S. Schmidt, J. Flueckiger, X. Wang, W. Shi, A. Millspaugh, M. Webb, D. Ratner, K. Cheung, L. Chrostowski, “Label-free silicon photonic biosensors for use in clinical diagnostics”, Proc. SPIE, Silicon Photonics VIII, 8629:86290914 (**Invited**), *SPIE OPTO*, International Society for Optics and Photonics, 2/02/2013.
5. S. Schmidt, J. Flueckiger, W. Wu, S. M. Grist, **Sahba Talebi Fard**, V. Donzella, P. Khumwan, E. R. Thompson, Q. Wang, P. Kulik, X. Wang, A. Sherwali, J. Kirk, K. C. Cheung, L. Chrostowski, and D. Ratner, “Improving the performance of silicon photonic rings, disks, and bragg gratings for use in label-free biosensing”, Proc. SPIE, Biosensing and Nanomedicine VII 9166, 91660M (2014).
6. **Sahba Talebi Fard**, E. Kwok, and L. Chrostowski, “Optical Glucose Monitoring Sensors”, Canadian Medical and Biological Engineering Conference (2014).

Appendix A. List of Publications

---

7. V. Donzella, A. Sherwali, J. Flueckiger, S. Grist, **Sahba Talebi Fard**, and L. Chrostowski, “Design and fabrication of SOI micro-ring resonators based on sub-wavelength grating waveguides”, *Optics Express* (2014).
8. C. Fu, **Sahba Talebi Fard**, K. Lee, S. Hong, L. Lee “Nanoplasmonic Optoporation for Large-scale Precision Gene Regulation in Stem Cells”, in review (2014).
9. L. Chrostowski, X. Wang, J. Flueckiger, Y. Wu, Y. Wang, **Sahba Talebi Fard**, “Impact of fabrication non-uniformity on chip-scale silicon photonic integrated circuits”, Optical Fiber Communication Conference, Th2A. 37. 2014/3/9.
10. V. Donzella, A. Sherwali, J. Flueckiger, **Sahba Talebi Fard**, S. Grist, and L. Chrostowski, “Sub-wavelength grating components for integrated optics applications on SOI chips”, *Optics Express*, 22, no. 17 (2014/8/25): 21037-21050.
11. S. Moghaddamjoo, A. Tashakor, **Sahba Talebi Fard**, Y. Tashakkor, E. Kwok, Y. Li, N. Tavassoli, G. Tibbits, E. Grant, and A. Rawicz, “Characterization of Cardiac Troponin I Raman Signature in Bovine Serum Albumin and Human Blood Serum for the Potential Diagnosis of Myocardial Infarction”, in review
12. X. Wang, J. Flueckiger, S. Schmidt, S. Grist, **Sahba Talebi Fard**, J. Kirk, M. Doerfler, K. Cheung, D. Ratner, and L. Chrostowski, “A silicon photonic biosensor using phase-shifted bragg gratings in slot waveguide”, *Journal of Biophotonics*, 04/2013 2013.
13. S. Grist, S. Schmidt, J. Flueckiger, V. Donzella, W. Shi, **Sahba Talebi Fard**, J. Kirk, D. Ratner, K. Cheung, and L. Chrostowski, “Silicon photonic micro-disk resonators for label-free biosensing”, *Optics Express*, 21:79948006, 03/2013 2013.
14. V. Donzella, **Sahba Talebifard**, L. Chrostowski, “Study of waveguide crosstalk in silicon photonics integrated circuits”, Photonics North (2013)
15. **Sahba Talebifard**, V. Donzella, S. A. Schmidt, D. M. Ratner, R. J. Bojko, L. Chrostowski, “Sensitivity analysis of thin waveguide SOI ring

- resonators for sensing applications.” International Photonics Conference (IPC), 2013 IEEE, pages 616-617.
16. V. Donzella, **Sahba Talebifard**, L. Chrostowski, “Modeling of asymmetric slot racetracks for improved bio-sensors performance”, Numerical Simulation of Optoelectronic Devices (NUSOD), 2013
  17. W. Shi, H. Yun, C. Lin, M. Greenberg, X. Wang, Y. Wang, **Sahba Talebi Fard**, J. Flueckiger, N. Jaeger, L. Chrostowski, “Ultra-compact, flat-top demultiplexer using anti-reflection contra-directional couplers for CWDM networks on silicon”, *Optics express* 21 (6), 6733-6738, 2013/3/25.
  18. V. Donzella, **Sahba Talebifard**, L. Chrostowski, “Fabrication and experimental characterization of cascaded SOI micro-rings for high-throughput label-free molecular sensing”, *Industrial & Engineering Chemistry Research*, 2013
  19. **Sahba Talebi Fard**, L. Chrostowski, E. Kwok, M.C. Amann, “Chemo-metric Approach for Improving VCSEL-based Glucose Predictions”, *IEEE Transactions on Biomedical Engineering*, vol. 57, issue 3, pp. 578-585, 02/2010.
  20. **Sahba Talebi Fard**, W. Hofmann, P. Talebi Fard, E. Kwok, M.C. Amann, L. Chrostowski, “Optical Glucose Monitoring using Vertical Cavity Surface Emitting Lasers (VCSELs)”, *SPIE Optics and Photonics Symposium - Bio-Sensing-II - Novel and Bio-inspired Sensors*, vol. 7397, pp. 739704-1 to 739704-11 (**Invited**), 2/08/2009.
  21. **Sahba Talebi Fard**, “Glucose Monitoring”, *Master’s Thesis*, The University of British Columbia, Aug. 2008.
  22. **Sahba Talebi Fard**, W. Hofmann, P. Talebi Fard, G. Bohm, M. Ortseifer, E. Kwok, M.C. Amann, L. Chrostowski, “Optical Absorption Glucose Measurements Using 2.3  $\mu\text{m}$  Vertical Cavity Semiconductor Lasers”, *IEEE Photonics Technology Letters*, vol. 20, issue 11, pp. 930–932, 06/2008.
  23. **Sahba Talebi Fard**, L. Chrostowski, E. Kwok, “Measuring Blood Glucose Using Vertical Cavity Semiconductor Lasers (VCSELs)”, *Canadian Medical and Biological Engineering Society Conference*, 06/2007.

# Appendix B

## Derivation of Sensitivity Formula

Here we review the derivation of the sensitivity formula for resonator sensors based on [43].

Considering dispersion in a resonator, the mode condition is given by equation B.1:

$$m\pi = \frac{2n_{eff}L}{\lambda_{res}} \quad (\text{B.1})$$

where, L is the length of the resonator,  $\lambda_{res}$  is the resonant wavelength, and  $n_{eff}$  is the effective index of the waveguide.

The group index ( $n_g$ ) is defined as:

$$n_g = n_{eff} - \lambda_{res} \frac{\delta n_{eff}}{\delta \lambda} \quad (\text{B.2})$$

Now, equating the mode at initial wavelength and the shifted wavelength (using equation B.1), we have:

$$\frac{n_g + \lambda_{res} \frac{\delta n_{eff}}{\delta \lambda}}{\lambda_{res}} = \frac{n_g + (\lambda_{res} + \Delta \lambda_{res}) \frac{\delta n_{eff}}{\delta \lambda} + \Delta n_{cl} \frac{\delta n_{eff}}{\delta n_{cl}}}{\lambda_{res} + \Delta \lambda_{res}} \quad (\text{B.3})$$

Solving this equation, we can find wavelength shift as a function of the change in refractive index of the cladding, which defines sensitivity of the resonator.

$$\frac{\Delta \lambda_{res}}{\Delta n_{cl}} = \frac{\lambda_{res}}{n_g} \frac{\delta n_{eff}}{\delta n_{cl}} \quad (\text{B.4})$$